A robust statistical method for determining material properties and indentation size effect using instrumented indentation testing

Yang Xia

Par **Yang XIA**

A robust statistical method for determining material properties and indentation size effect using instrumented indentation testing

Thèse présentée
pour l'obtention du grade
de Docteur de l'UTC

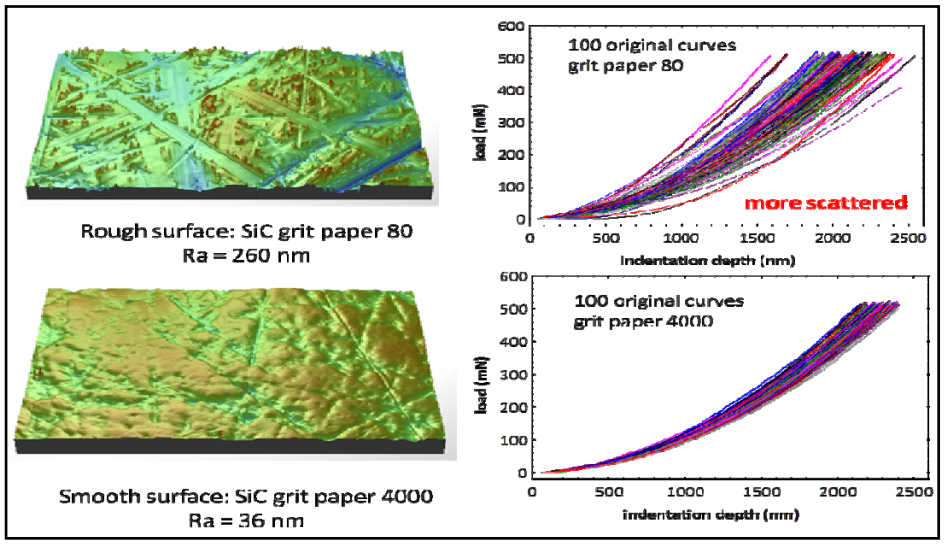

Soutenue le 18 septembre 2014
Spécialité : Mécanique Avancée : Unité de recherche en Mécanique - Laboratoire Roberval (UMR-7337)
D1982

Université de Technologie de Compiègne

Ecole Doctorale

Spécialité : Mécanique Avancée

A robust statistical method for determining material properties and indentation size effect using instrumented indentation testing

Yang XIA

Soutenue le 18 Septembre 2014

Jury

Rapporteur	S. Benayoun	Ecole Centrale de Lyon
	D. Chicot	Université Lille 1
Invité	A. Iost	Ecole Nationale Supérieure d'Arts et Métiers
	P.-E. Mazeran	Université de Technologie de Compiègne
	V. Le Houerou	Institut Charles Sadron
Directeur de thèse	M. Bigerelle	Université de Valenciennes
Co-directrice de thèse	S. Bouvier	Université de Technologie de Compiègne

Thèse préparée au sein du Laboratoire Roberval, UMR 7334.

Abstract

Instrumented indentation is a practical and powerful tool for probing the mechanical properties of materials at small scales. However, several errors (surface roughness, indentation size effect, determination of first contact point, *etc*…) affect the instrumented indentation testing (*e.g.* the low reproducibility of the indentation curves) and lead to inaccuracies in the determination of mechanical properties of materials analyzed. An original approach is developed in this thesis for the accurate characterization of the mechanical properties of materials. This approach is established by a statistical analysis of the indentation curves with taking account of error in determining the first contact point and effects of the surface roughness. This approach is basing on a minimization of the distance (defined as the initial contact depth error) between the experimental indentation curves and the ones simulated with Bernhard's model in order to generate a "unique" representative curve which enables to represent all the experimental curves. The proposed method permits to calculate the macro-hardness and the Young's modulus of materials from this representative curve with the consideration of the errors due to the surface roughness and the indentation size effect for shallow penetration. The robustness of the method is proved by its application to different groups of specimens, *i.e.* different materials with various mechanical properties, different surface preparation methods (polishing, sandblasting) and different indenter tips to generate different states of local stresses. A quantitative link between the surface roughness and the standard deviation of initial contact depth error is established by a multi-scale surface roughness analyzing. The proposed method enables to characterize the mechanical properties of materials without resorting to the surface preparation which may potentially alter its properties (*e.g.* generation of residual stresses, surface contamination ...).

Keywords:

Instrumented indentation, Macro-hardness, Indentation size effect, Surface roughness, Initial contact depth error.

Résumé

L'Indentation instrumentée est un outil pratique et puissant pour sonder les propriétés mécaniques des matériaux à petite échelle. Cependant, plusieurs erreurs (rugosité de surface, effet de taille d'indentation, la détermination de premier point de contact, *etc.*) affectent l'essai d'indentation instrumentée (*e.g.* non reproductibilité de la courbe d'indentation) et conduisent à des imprécisions dans la détermination des propriétés mécaniques des matériaux analysés. Une approche originale est développée dans cette thèse pour la caractérisation précise des propriétés mécaniques des matériaux. Cette approche fondée sur une analyse statistique des courbes d'indentation avec la prise en compte d'erreur dans la détermination du premier point de contact et des effets de la rugosité de surface. L'approche est basée sur une minimisation de la distance (défini comme l'erreur de la profondeur de contact initiale) entre l'ensemble des courbes expérimentales et celles simulées par le modèle de Bernhard de manière à générer une courbe maitresse « unique » représentative du faisceau de courbes expérimentales. La méthode proposée permet de calculer à partir de cette courbe maitresse la macro-dureté et le module d'Young du matériau en tenant compte des erreurs dues à la rugosité de surface et à l'effet de taille en indentation pour les faibles profondeurs de pénétration. La robustesse de la méthode est prouvée par son application à différents groupes d'échantillons, *i.e.* panels de matériaux à propriétés mécaniques diverses, différents traitements de surface (polissage, sablage) et différentes pointes d'indentation permettant de générer différents états de contraintes locaux. Une liaison quantitative entre la rugosité de surface et l'écart type de l'erreur de la profondeur de contact initiale est établie grâce à une analyse multi- échelle de la rugosité de la surface. La méthode proposée permet de caractériser les propriétés mécaniques des matériaux sans avoir recours à la préparation de surface pouvant potentiellement altérer ses propriétés (*e.g.* génération de contraintes résiduelles, contamination de surface…).

Mots clés:

Indentation instrumentée, Macro-dureté, Effet de taille de l'indentation, Rugosité de surface, Erreur de la profondeur de contact Initiale.

Publications:

- J. Marteau, Y. Xia, P.-E. Mazeran, S. Bouvier, M. Bigerelle (2012), “Zero-point correction method for nanoindentation tests to accurately quantify hardness and indentation size effect”, Strain Vol. 48(6), pp. 491-497.

- J. Marteau, M. Bigerelle, Y. Xia, P.-E. Mazeran, S. Bouvier (2013), “Quantification of first contact detection errors on hardness and indentation size effect measurements”, Tribology International 59: 154-162.

- Y. Xia, M. Bigerelle, J. Marteau, P.E. Mazeran, S. Bouvier, A. Iost (2014), “Effect of surface roughness in the determination of the mechanical properties of material using nanoindentation test”, Scanning 36:134-149.

- Y. Xia, M. Bigerelle, S. Bouvier, A. Iost, P.E. Mazeran (2014), “Quantitative approach to determine the mechanical properties by nanoindentation test: application on sandblasted materials”, Tribology International, *DOI: 10.1016/j.triboint.2014.07.022*.

- J. Marteau, M. Wieczorowski, Y. Xia, M. Bigerelle (2014), "Multiscale assessment of the accuracy of surface replication", Surface Topography: Metrology and Properties, *Accepted*.

Table of contents

Table of figures

Table of tables

Chapter I General Introduction

Instrumented indentation testing, also referred to as depth-sensing indentation testing, is a widely used method to investigate the near-surface mechanical properties, at depths of a few micrometers. The instrument continuously measures the load and indentation depth during an entire loading and unloading circle, and then the hardness and the elastic modulus are estimated by the analyzing of the load-depth response (P-h curve). However, the level of accuracy of the hardness and elastic modulus values from indentation test is always a question. One manifestation of this low accuracy is the no reproducibility of P-h curves for homogeneous and isotopic materials. Various errors are associated with this problem and the main reasons can be divided schematically into three categories:

- Environmental and device issues, *e.g.* temperature changes, indenter properties (geometry shape and mechanical behaviors of the indenter tip),
- Material related issues, *e.g.* time dependent response, surface hardening (due to the polishing or another method of processing) and surface roughness,
- Depth measurement issues, *e.g.* contact profile (pile-up or sink-in) and the determination of the first contact point (the initial depth of penetration).

In addition to the above, indentation size effect (ISE), *i.e.* a significant increase in hardness with the decrease of depth at small depths, is another serious factor that affects the validation of the results of instrumented indentation test. For crystalline materials, the most popular mechanism for explaining ISE phenomena is basing on the geometrically necessary dislocations (GNDs) and strain gradient theory, which is shown as Nix-Gao model. However, some of the experimental hardness data can deviate significantly from the prediction of the above model when the depths are less than several hundred nanometers. There are two main types of factor for the discrepancy between the predicted hardness and observed hardness at very shallow indentation depths: one is the inherent factors about the response of materials during instrumented indentation test (*e.g.* Peierls stress, storage volume for GNDs), the other is the extrinsic factors such as blunt tip on a sharp indenter, chemical contamination and surface roughness. It is worth noting that these above-mentioned extrinsic factors of ISE phenomena are also the origins of the hardness errors, which means that while the errors on the characterization of mechanical properties are not independent, and some of them influence each other in practice (*e.g.* ISE and surface roughness). Among these factors, some of them can be avoided by a proper specimen preparation or indenter calibration, except for the surface roughness. In fact, the influence

of surface roughness on hardness or ISE can also be reduced with a sufficient surface preparation (*e.g.* polishing), but the latter would introduce some surface hardening, which would also affect the hardness measurement at the early stage of indenter penetration. Consequently, a certain amount of surface roughness is an unavoidable factor in instrumented indentation testing.

Surface roughness can have a significant influence on the hardness and ISE estimation because the instrumented indentation testing estimates the mechanical properties of the tested material based on the assumption that the specimen surface is flat. Then it uses the measured indentation depth from the "flat surface" to calculate the projected contact area and subsequently to calculate the hardness. But no surface is perfectly flat and the measured indentation depth from the "flat surface" will be overestimated or underestimated. Thus the corresponding contact area and mechanical properties will be affected subsequently by the depth error. Therefore, the main aim of this thesis is to quantify the effect of the surface roughness on the instrumented indentation data and try to develop a more general method to accurately characterize the material mechanical behavior with the consideration of surface roughness effect on the instrumented indentation testing.

In the present work, a set of specimens with different surface roughness are studied. The material parameters are determined through an inverse method that relies on an original quantitative statistical model. This model highlights the influence of the roughness on nanoindentation curve and leads to a more accurate determination of the mechanical properties based on two innovative concepts. The first one consists in marking the curves by a specific definition of the initial contact depth error, defined as a gap between the actual experimental loading curve and the simulated one using Bernhardt's law. The second innovative concept of our method lies in the use of the curves for calculation of the set of mechanical parameters. Our method is based on the treatment of all the curves as a whole *i.e.*, the mechanical properties are determined by minimizing a function that process all the curves. This concept differs from usual data treatment methods as they calculate the mechanical parameters from each curve and then the average value of the mechanical parameters from different curves is calculated as the final results.

In order to prove the robustness of the proposed method and to ensure the universality of the investigations in this thesis, the more detail studies in this thesis with the proposed method is separated into three aspects as follow:

- Different materials which are having different hardening (Stainless steels, Aluminum based, Titanium based and replication material), for each material, a set of specimens having different roughness are studied,
- Different indenter shapes which will produce different plastic zone and the stress state in the subsurface (Berkovich and Cube-Corner indenter),
- Different surface preparation methods which will generate different residual stresses and different types of roughness on the specimens (mechanical polishing or sandblasting), the different surface roughness are achieved by changing the grit paper size or changing the air pressure, respectively.

Furthermore, in order to identify the material properties of the specimens with a presence of surface roughness, a suitable estimation of the surface roughness is required because the surface roughness is very sensitive to the evaluation length. Therefore, a multi-scale surface roughness analysis is performed to find the best evaluation length for surface estimation when studying the instrumented indentation data. Thanks to this multi-scale surface roughness analysis method, combining with the investigation of initial contact depth errors by the proposed model, the effect of surface roughness on scatter of the instrumented indentation curves is studied quantitatively. Finally, a surface replication technology is used to generate the specimens (model specimens and replicated specimens) which are made with different material but having similar surface roughness. Then the effect of the surface roughness on the distribution of the initial contact depth error is further proved by applying the proposed method on these specimens.

After this general introduction, the manuscript is divided into four chapters. Chapter II begins with a presentation of the materials and the experimental techniques (*e.g.* surface generation and measurement methods) used to this study. Then it reviews the basic theory of the instrumented indentation testing and the related load-depth curve analysis method used for the identification of material properties. At last, the original proposed load-depth curve analysis method and the multi-scale surface roughness analysis method are described.

Chapter III is devoted to the evaluation of the robustness of the proposed model. The first part is focus on the comparison of the mechanical properties given by the proposed

method with several other data treatment methods. The second part aims to introduce the multi-scale analysis method for surface roughness and to assess the effect of surface roughness on the distribution of the initial contact depth error. The last part is dedicated to estimate the Young's Modulus with the proposed method with the consideration of the surface roughness effect. In order to verify the reliability of the proposed model for different materials and surface treatment methods, the above three studies are realized through analyzing the instrumented indentation curves performed on three different specimens. They are: polished austenitic stainless steel 316L, sandblasted aluminum-based alloy 2017A, and polished aluminum-based alloy 2017A, separately. At the same time, the origin of the initial contact depth error and the effect of surface roughness on the identification of the mechanical properties are investigated for each specimen.

Chapter IV is focus on assessing the efficiency of the proposed method on different indenters (*i.e.* Berkovich and Cube-Corner). The specimen used in this chapter is the polished titanium-based alloy TA6V4. Moreover, the mechanical properties, including the hardness and Young's modulus, obtained for different indenters with the proposed model are compared. At last, the errors affecting the identification of the mechanical properties due to the surface roughness for different indenters are quantified.

In Chapter V, the surface of several polished titanium-based alloy TA6V4 specimens are chosen as the model surface and they are reproduced by the surface replication technology. The similarity of the surface roughness between the model surface and the replicated one are studied. With the comparison of the indentation data performed on the replication and model materials, the effect of the surface roughness on the distribution of the initial contact depth error for these two materials is shown. The ability of the proposed method in the characterization of the mechanical behaviors unrelated with the surface roughness, *i.e.* application of the proposed method on two different materials (metal and replication material) having the same surface roughness, is investigated.

Finally, this thesis ends with a general conclusion and suggestion of possible prospects.

Chapter II Experimental techniques and numerical methodology for the indentation test analysis

II.1 Overview

This chapter consists of two parts. The first part describes the experimental techniques used in the thesis. Three types of materials, surface generation and measurement methods are presented. The principal of the instrumented indentation testing and a special multi-scale surface roughness analysis method are also introduced. The second part introduces the original proposed numerical methodology for the instrumented indentation test analysis, which is the core method of this thesis. The key differences between the novel numerical model and the traditional method about the instrumented indentation curve treatment are highlighted.

II.2 Experimental techniques

II.2.1 Materials

To investigate the universality of the method, three materials which possess different resistance to a plastic deformation were studied in this thesis: titanium-based alloy TA6V4 (R_e = 800 MPa, R_m = 900 MPa), austenitic stainless steel 316L (R_e = 170 MPa, R_m = 500 MPa) and aluminum-based alloy 2017 (R_e = 220 MPa, R_m = 400 MPa). The chemical compositions (in wt %) of the materials are given in Table 1. For each material, the specimens were cut from a round bar and into a circular cylinder with a diameter of 30 mm and a thickness of 20 mm. Finally, 11 specimens were prepared for TA6V4 and 316L, and 15 specimens for 2017A.

TA6V4	Al	V	Fe	O	C	N	Y	H	Ti		
	6.13	4.00	0.11	0.11	0.004	0.006	<0.001	0.0007	base		
316L	C	Si	Mn	Ni	Cr	Mo	N	S	P	Cu	Fe
	0.008	0.27	1.62	14.58	17.58	2.8	0.06	0.001	0.014	0.07	Base
2017A	Zn	Mg	Cu	Cr	Mn	Fe	Si	Zr +Ti			Al
	≤ 0.25	0.4-1.0	3.5-4.5	≤ 0.1	0.4-1.0	≤ 0.7	0.2-0.8	≤ 0.25			Base

Table 1: The chemical compositions (in wt %) of the materials.

II.2.2 Different processes for surface generation

Two surface treatment processes were employed in this study: mechanical polishing and sandblasting. Both of them shape the surface with the help of abrasive particles. Mechanical polishing is the process of grinding the surface on the abrasive disks under an

external load, while sandblasting is the operation of forcibly propelling a stream of abrasive material against a surface under high pressure.

- **Mechanical polishing**

A specific automatic polishing machine (STRUERS, France) having two off-center rotating movement was used in the experiments. First, all the specimens were polished to a mirror-like surface *i.e.* to silicon carbide grit paper 4000 to obtain similar initial states. Then, several different surface roughness were achieved using different grit papers under a fix load and time (150 N, 3 min) with water lubrication at 300 revolutions per minute. For each material, eleven specimens were polished. The different surface states correspond to the ending of the abrasion after using grit papers: 80, 120, 180, 220, 320, 500, 800, 1000, 1200, 2400 or 4000.

- **Sandblasting**

The process of sandblasting is just used to treat the other 4 surfaces of the specimens 2017A. To ensure all the specimens have the same mechanical and topographical initial state, a pre-polishing with the 120, 320 and 1000 silicon carbide grit papers and a fine polishing with a 3 µm grain size diamond DP-Spray lubricant were performed successively. Each specimen was then sandblasted using 500 µm Al_2O_3 particles in a machine CSF 70 V. By changing the parameters of sandblasting, *i.e.* air-jet pressure, the distance and the included angle between the surface and the blasting tip, different surfaces of the specimens are shaped. The parameters of the sandblasting process for different specimens named S1, S2, S3 and S4 are listed in Table 2.

Specimen	Pressure (bar)	Distance (cm)	Angle
S1	1	15	90
S2	1	30	90
S3	0.5	30	90
S4	0.5	30	60

Table 2: Sandblasting parameters for four 2017A specimens.

II.2.3 Surface measurement metrology

The two dimensional 2D and three dimensional 3D surface topographies of the abraded and replicated specimens were measured using contact (tactile profilometer) and non-contact (optical interferometer) equipments, respectively. The 2D measurement

provides surface profiles for roughness analysis, while the 3D measurement provides surface topographies or indentation prints more directly.

- **Two dimensional surface measurement: 2D**

The 2D surface measurement was performed with a tactile profilometer TENCOR P10 (KLA-TENCOR, USA). It is based on the principle of running a probe across a surface in order to detect variations in height as a function of distance. The vertical sensitivity of the profilometer is 10 nm and the horizontal sensitivity is 50 nm. A stylus with a tip radius of 2 µm was used to probe the surface under a 5 $\times 10^{-5}$ N load. The high-resolution 2D surface profiles were recorded with a measurement length of 5 mm at a speed of 200 µm/s. Each profile is described by 25,000 points (0.2 µm between each point). For each specimen, 30 profiles were recorded.

- **Three dimensional surface measurement: 3D**

The 3D surface measurement was carried out using an optical interferometer Zygo NewView 7300 (Zygo, USA) with Vertical Scanning Interferometry (VSI) mode. The principle of the machine is that a white light source beam is focused by a lens and then is separated into two parts by a beam splitter. The first portion is reflected by the sample while the latter is reflected by the reference mirror. Finally, these two parts are recombined by the beam splitter, which leads to the observation of fringes (see Figure 1). In VSI mode the objective moves vertically to scan the surface at various heights. The fringes are changed with the movement of the objective. Thus, the surface heights can be calculated with the recorded fringe modulation data, and then the surface topography is described.

A 640 x 480 pixels field zoom lens and a 20X magnification Mirau objective were used. The optical resolution in lateral spatial (x-y axis) and vertical spatial (z axis) is 0.71 µm and 0.55 µm, respectively. The maximum vertical scan length is 100 µm to assure all peaks and valleys of the surface can be measured. The scan time of one measurement is 7 seconds. In order to increase the field of view, stitching process was used. This process makes several measurements of the specimen surface as it is moved by a motorized stage and then combines the multiple data sets into one [1]. The stitching was realized using sixteen 348 µm x 262 µm measurement areas with an overlapping percentage equal to 20%. And 20 stitching processes were performed for each specimen.

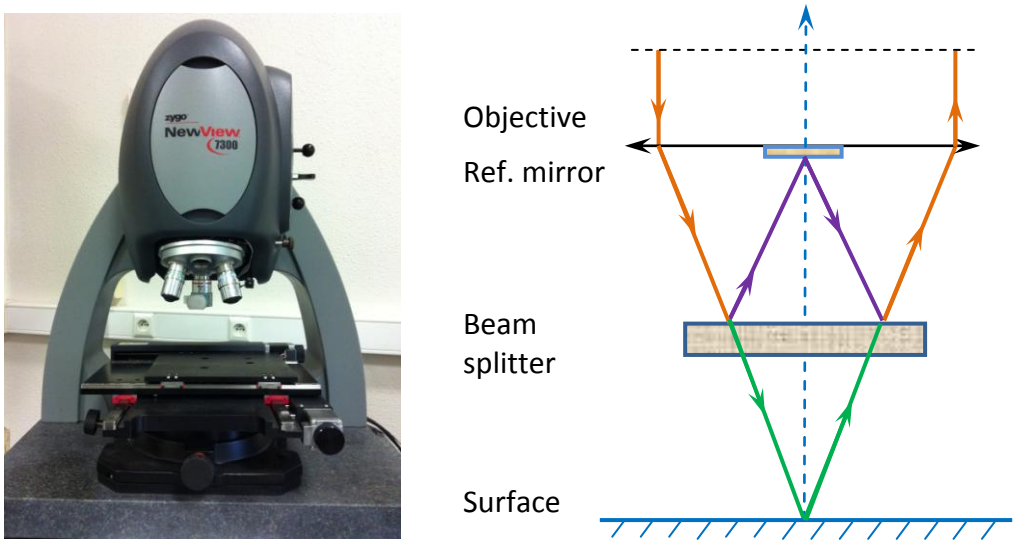

Figure 1: Optical interferometer Zygo NewView 7300 and Optical path of Mirau objective.

II.2.4 Multi-scale surface roughness analysis

Surface roughness parameters are important quantitative index for surface study. But they strongly depend on the scale at which they are calculated, *i.e.* evaluation length [2]. It is difficult for surface parameters to reflect the whole surface when the evaluation length is too short, while it is not suitable for surface parameters to capture finer surface details when the evaluation length is too long. The majority of the surface characterization methods measure the surface topography and provide the surface parameters in a given evaluation length that does not allow to both having high definition and high scanning area [3]. It is therefore necessary to achieve a multi-scale surface roughness analysis to find the best evaluation length in a particular study. Multi-scale surface analysis is a procedure to recalculate the surface roughness parameters with different evaluation lengths [4]. It requires the splitting of each experimental profile into equal parts, considered each as an evaluation length. Then, a pretreatment to remove the local variations of the surface is performed by calculating regression parameters on a given window. Each sub-profile is then rectified by a smoothing polynomial of order 3 and the least square adjustment method. Basically, this treatment is similar to a high-pass filtering revealing the micro roughness. By applying this multi-scale surface analysis method on the surface measurement data of all the specimens, the rectified profiles with different evaluation lengths were formed as shown in Figure 2. For each specimen, the surface parameter can be calculated basing on the different rectified profiles.

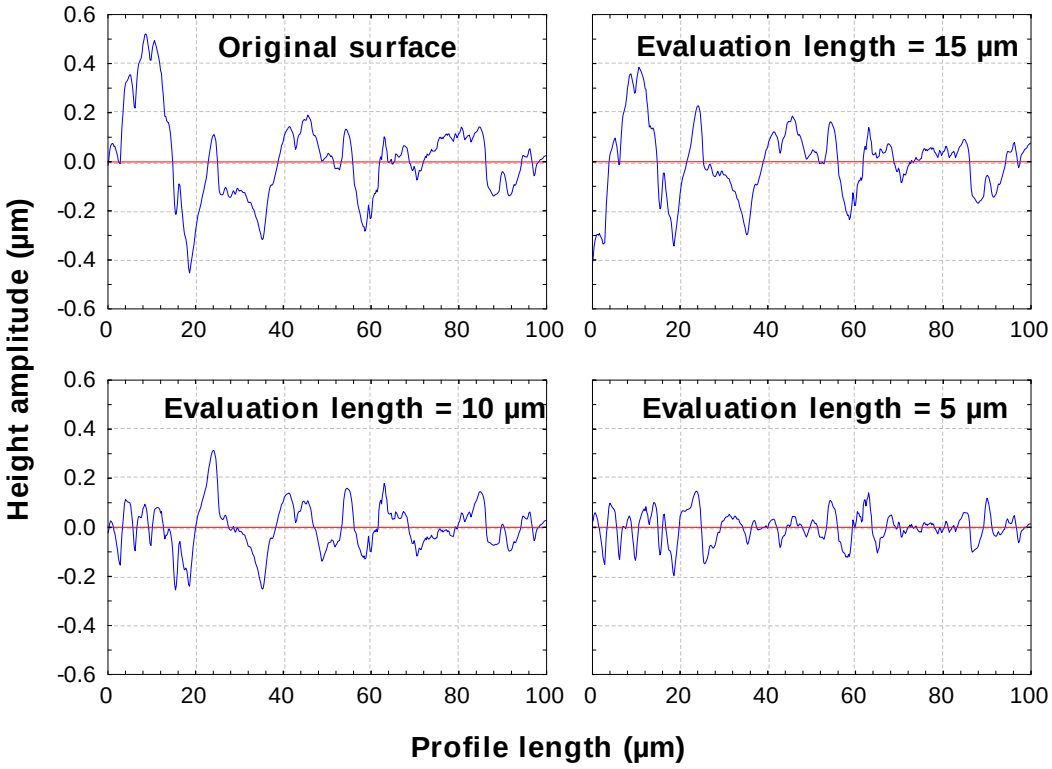

Figure 2: Original surface profile and rectified profiles calculated with evaluation length 15, 10 and 5 µm, for specimen TA6V4 polished with grit paper 500.

II.2.5 Instrumented indentation testing

The instrumented indentation testing is widely used for mechanical characterization of the small volume of elastoplastic materials [5]. In this test, the vertical force is applied to press an indenter into the surface of specimen. The force and the displacement of the indenter are measured continuously during the loading and unloading steps, from which the hardness and elastic modulus are estimated. The forces involved are usually in the millinewton (10^{-3} N) range and are measured with a resolution of a few nanonewtons (10^{-9} N). The depths of penetration are in the order of micrometers with a resolution of less than a nanometer (10^{-9} m) [5].

II.2.5.1 Instrumented indentation system

As shown in Figure 3 [6], the typical instrumented indentation testing system consists of three main parts: a diamond indenter usually mounted to a rigid indenter column, an electromagnetic coil for load application, and a capacitive sensor for measuring the displacements of the indenter. The test sample is fixed on a specimen supporter, and an X-Y-Z table for moving the specimen under the indenter.

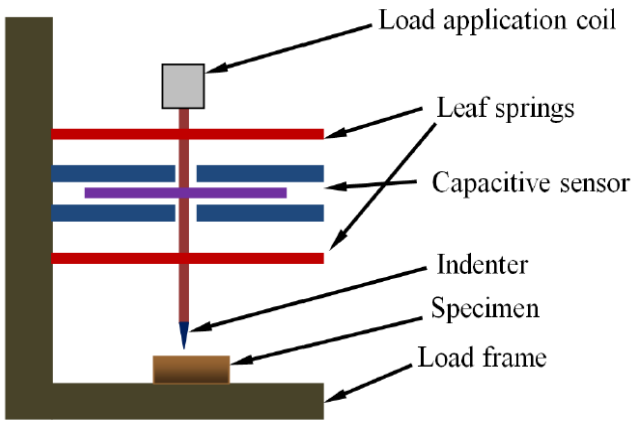

Figure 3: A schematic illustration of the instrumented indentation test [6].

A nanoindentation test process is as follows [7]: the load P is applied to indenter by an electromagnetic coil, which allows knowing the value of the load by measuring the current flowing in the coil. As the force is transmitted through the indenter column, the indenter firstly approaches the test surface until contact is sensed as a distinctly increase in contact stiffness. Then, the indenter is starting to be pressed vertically into the surface of the specimen until the maximum force P_{max} or the maximum displacement h_{max} (specified by the user) is achieved. The displacement h is usually measured by a capacitive sensor. The load on the indenter is held constant for a given time at the peak load and then the indenter is withdrawn completely from the specimen at a rate that is comparable to the pressing rate. During the test, the load and the depth of the penetration are recorded continuously for a complete loading and unloading cycle. Finally, a load-depth curve is generated [8].

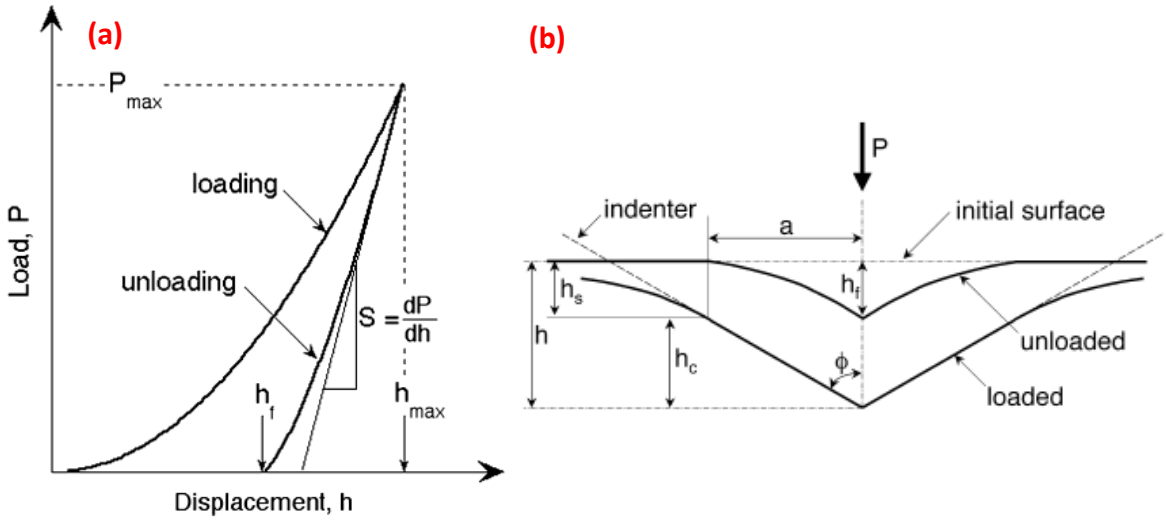

Figure 4: Schematic representations of (a) typical indentation load-depth curve and (b) indentation profiles with various quantities [8].

Figure 4(a) shows the load-depth behavior during both the loading and unloading of the indenter. Correspondingly, a schematic representation of the indentation profiles with various quantities is shown in Figure 4(b). As the indenter is driven into the material, both elastic and plastic deformation processes occur, producing a hardness impression that conforms to the shape of the indenter to some contact depth (h_c). When the indenter is unloaded, the elastic strains are recovered. The residual depth of the hardness impression after final unloading is named as the final depth (h_f). Then these important quantities: the peak load ($P_{\max}$), the maximum depth ($h_{\max}$), the final or residual depth after unloading (h_f), the contact depth (h_c), and the slope of the upper portion of the unloading curve ($S = dP/dh$) are used to calculate the mechanical properties. The two mechanical properties which are most frequently extracted from this load-depth curve are Hardness (H) and Young's modulus (E). The physical principles and models used to determine H and E from indentation load-depth data will be presented further in Section II.2.5.2.

II.2.5.2 Calculation of mechanical properties

- **Hardness**

The fundamental formula of the hardness is defined as the ratio between the applied force P on the indenter and the projected contact area A at that load. It is expressed by the following equation:

$$H = \frac{P}{A}. \tag{2.1}$$

It is worth to note that the hardness determined by nanoindentation test is computed under load. It is more precise than the hardness obtained from the conventional method, which is determined by measurement of the size of the residual hardness impression. Especially when the contact is predominantly elastic, the residual contact area after unloading is small. In this case, the conventional definition of hardness will yield a greater value than that obtained by the procedure outlined here.

- **Elastic modulus**

Since the fact that the elastic displacements occur in both the indenter and the specimen during nanoindentation testing, the elastic modulus of the tested material E

could be determined indirectly by the calculation of the reduced elastic modulus E_r with the following Hertz function [9]:

$$\frac{1}{E_r} = \frac{1-v^2}{E} + \frac{1-v_i^2}{E_i}, \tag{2.2}$$

where v is the Poisson's ratio for the tested material, and E_i and v_i are respectively the elastic modulus and the Poisson's ratio of the indenter.

The reduced elastic modulus E_r is calculated as,

$$E_r = \frac{\sqrt{\pi}}{2}\frac{S}{\sqrt{A}}, \tag{2.3}$$

where A is the contact area and S is the contact stiffness between the indenter and the specimen.

The Equation (2.3) is obtained from Sneddon function [10] which is found in elastic contact theory. It is originally derived to calculate the force and the displacement for a conical indenter. Then, Bulychev *et al* [11] showed that this equation is equally suitable for spherical and cylindrical indenters. Subsequently, Pharr [12] proved that the formula (2.3) is operable for any axis symmetrical indenter.

According to the equations (2.1), (2.2) and (2.3), it is clear that in order to calculate the elastic modulus and hardness, it is necessary to know the load P, the projected contact area A, the contact stiffness S and the elastic properties of the indenter. The load is directly recorded, and the elastic properties of the indenter are known (For diamond indenter, the elastic constants E_i = 1141 Gpa and V_i = 0.07 are often used [13]). In contrast, the projected contact area A and the contact stiffness S could not be obtained directly. We explain how to calculate them in Section II.2.5.3.

II.2.5.3 Determination of the contact stiffness

The contact stiffness S can be determined in two ways. It is determined either by a quasi-static method based on a fitting equation of the unloading-depth curve, or by a dynamical method based on a direct measure of dynamic contact stiffness during the loading portion of an indentation test [14]. Each of these methods for the contact stiffness determination is explained in detail in this section.

- **Quasi-static method**

The quasi-static method is to calculate the contact stiffness from the unloading curve. This calculation is possible because the contact between the indenter and the sample is considered as purely elastic during initial part of unload.

Doener and Nix [15] have shown firstly that, for a Berkovich indenter, the elastic behavior of the indentation contact during initial stage of unloading curve is similar to that of a flat cylindrical punch. The initial part of the unloading curve then could be considered as the elastic law of the flat cylindrical punch established by Sneddon, *i.e.* the relation between the load and the depth is linear. Therefore, by extrapolating the initial linear portion of the unloading curve to zero load, it is possible to obtain the contact stiffness using the extrapolated depth with the maximum load value.

However, Oliver and Pharr [16] has found that the unloading curve for pyramidal indenter is usually not linear as suggested by Doerner and Nix, but is described by a power law:

$$P = B(h - h_f)^m, \tag{2.4}$$

where B and m are empirically determined fitting parameters. Equation (2.4) is differentiated with respect to depth, and then the contact stiffness is obtained at the maximum displacement:

$$S = \frac{dP}{dh}\Big|_{h=h_{\max}} = Bm(h - h_f)^{m-1}. \tag{2.5}$$

Once the contact stiffness is determined, the reduced elastic modulus E_r can be calculated by Equation (2.3). However, this method just permits to determine the stiffness from the slope of the unloading curve at the maximum load. Thus a continuous stiffness measurement technique is established to provide a continuous measurement during a nanoindentation process.

- **Continuous stiffness measurement (CSM) method [17]**

The CSM method is to measure the stiffness continuously during the loading portion of the indentation test. It is accomplished by imposing a small dynamic oscillation on the nominally load signal and measuring the resulted dynamic displacement response of the

indenter system by means of a frequency-specific amplifier. Then the contact stiffness can be determined continuously as a function of depth.

With the CSM method, besides the load applied by the electromagnetic coil, a small amplitude oscillation at a given frequency ω is superimposed on the nominal load. The oscillating force is:

$$F(t) = F_0 e^{i\omega t} \ , \tag{2.6}$$

where $F(t)$ is the harmonic oscillation force superimposed on load P , F_0 is the amplitude of $F(t)$, ω is the frequency and t is time. Then the response of the indenter as a consequence of the oscillating force is:

$$z(t) = z_0 e^{i(\omega t - \varphi)} \ , \tag{2.7}$$

where $z(t)$ is the harmonic oscillation of the indenter, φ is an phase angle by which the response function $z(t)$ lags the force function $F(t)$.

The relationship between the force and the response of the indenter movement can be described by a second-order differential equation:

$$m\ddot{z}(t) + D\dot{z}(t) + Kz(t) = F(t) \, , \tag{2.8}$$

where m , D and K are the mass, damping and stiffness of the system, respectively. By injecting Equation (2.6) and (2.7) into Equation (2.8), the transfer function of the dynamic system is obtained:

$$-m\omega^2 + iD\omega + K = \frac{F_0}{z_0} e^{i\varphi} \ , \tag{2.9}$$

$$\tan(\varphi) = \frac{D\omega}{K - m\omega^2} \ . \tag{2.10}$$

These equations from (2.6) to (2.10) are just suitable for a simple-harmonic oscillator model, which means the indenter is free-handing. When the indenter is in contact with the specimen, we must account for the components of the indentation instrument (including the frame and the indenter) and the component of the contact together, as shown in Figure 5.

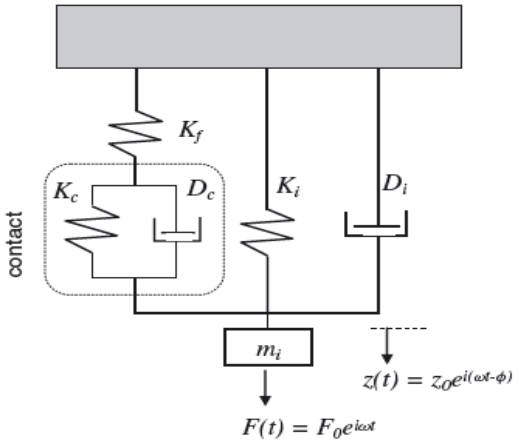

K_f : Elastic stiffness of indenter frame.

K_i : Spring constant.

D_i : Damping of indenter.

K_c : Contact stiffness (S).

D_c : Damping of contact.

Figure 5: Model accommodating both indentation instrument and contact [17].

In this case, the components of the indentation instrument and the contact may be combined and represented by effective components such that we can continue to use the simple-harmonic oscillator. Then the real stiffness and the damping of the contact could be analyzed by reducing the indentation instrument response. The stiffness and damping of indentation instrument components, including the frame and the indenter, are provided by the equipment manufacturer. Through dynamical analysis of the system, it is possible to calculate the contact stiffness and the damping of contact. From these two variables, the reduced elastic modulus can be determined.

This technique is much more efficient than the quasi-static method, because the stiffness is measured continuously during the test. It offers a direct measurement of contact stiffness at any point during the loading part of the indentation test, not just at the point of unloading.

II.2.5.4 Determination of the projected contact area

For the instrumented indentation test, the contact area is difficult to measure directly with optical equipment because the indentation imprint is very small. Thus Oliver, Hutchings and Pethica suggested determining the contact area with a simple method based on the knowledge of the indenter shape function, that is, the cross-sectional area of the indenter as a function of the distance from its tip [18]. In fact, this distance is just the contact depth which can be measured during indentation testing. Therefore, the determination of the contact depth is important for the calculation of the contact area.

- **Oliver and Pharr method [16]**

Oliver and Pharr provide a new means for determining the contact depth directly from the experimental measured load-depth data. They asserts that the measured depth at any point during loading comprise two parts: the contact depth h_c along the contact between the indenter and the specimen and the depth h_s due to the deflection of the surface at the perimeter of the contact as shown in Figure 3(b). The contact depth is expressed as:

$$h_c = h - h_s . \tag{2.11}$$

The penetration h is measured during the test. It is therefore necessary to determine h_s from the load-depth data. Oliver and Pharr assume that the deflection around the indenter at the perimeter contact is purely elastic. Thus the Sneddon equation for the shape of the surface outside the area of contact can be used to calculate the deflection. In the case of a conical indenter, the expression is the following equation:

$$h_s = \frac{(\pi - 2)}{\pi}(h - h_f) . \tag{2.12}$$

Here, the expression use quantity $h - h_f$ rather than h by itself since the Sneddon's solution applies only to the elastic component of the displacement. Furthermore, the Sneddon's load-depth expression for a conical indenter allows obtaining the following expression:

$$h - h_f = 2\frac{P}{S} , \tag{2.13}$$

where S is the stiffness. Combining the Equation (2.12) and (2.13), the following function is obtained:

$$h_s = \frac{2(\pi - 2)}{\pi}\frac{P}{S} = \varepsilon \frac{P}{S} , \tag{2.14}$$

where ε is a constant that depends on the indenter geometry. According to the elastic contact analysis, the geometric constant for the conical and flat punch indenter is equal to 0.72 and 1, respectively. A value of 0.75 is used almost exclusively as the geometry constant for spherical and pyramidal indenters.

Replacing h_s obtained with equation (2.14) in equation (2.11), the expression of the contact height from Oliver and Pharr method is obtained:

$$h_c = h - \varepsilon \frac{P}{S} \ . \tag{2.15}$$

Thus the projected contact area can be estimated with the area function:

$$A = f(h_c) \ . \tag{2.16}$$

Table 3 provides a summary of the area functions for various geometric indenters.

Tip Type	Shape	Area function	Comments
Berkovich	Pyramid	$A = 24.56 h_c^2$	—
Cube-Corner	Pyramid	$A = 2.6 h_c^2$	—
Sphere	Spherical	$A = 2\pi R h_c$	R is tip radius, contact radius a << 2R
Cone	Conical	$A = \pi \tan^2 \psi h_c^2$	ψ is half-included angle
Flat punch	Cylinder	$A = \pi a^2$	a is punch radius A is independent of h_c

Table 3: Area functions for various indenter geometries [7].

With the instrumented indentation technique, the contact stiffness of a material can be obtained either by quasi-empirical method that calculating the property at maximum load or by dynamical CSM method that measuring the property continuously during the loading procedure. Oliver and Pharr approach is the most often used model to calculate the contact depth. As these two quantities are calculated, it is possible to obtain the hardness and the elastic modulus of the material.

II.2.5.5 Experimental parameters

Instrumented indentation testing was made using a MTS Nanoindenter (Agilent Technologies, USA) equipped with a Berkovich diamond indenter or a Cube-Corner diamond indenter, as shown in Figure 6. Both of two indenters are a three-sided pyramid with geometrical self-similarity [19]. The geometrical faces of the Cube-Corner indenter are mutually perpendicular, which is like the corner of a cube. Moreover, the Cube-Corner

indenter is sharper than the Berkovich indenter. The angle between the axis of symmetry and a face for the Cube-Corner indenter is 34.3° whereas for the Berkovich indenter it is 65.3° [20]. The instrument is on an anti-vibration base and is located in an ambient temperature cabinet, which provides a thermally stable environment. Experiments were performed using the Continuous Measurement Method (CSM) at a constant strain rate (0.05 s^{-1}) until the maximum indentation depth of 3000 nm was achieved. One hundred (10 x 10) indentations were made for each specimen. To avoid the interaction of the indentations, the distance between two adjoining indentations was taken equal to 100 µm.

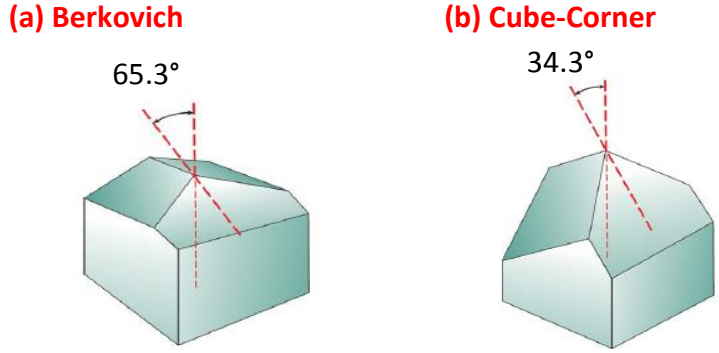

Figure 6: Indenter types (a) Berkovich and (b) Cube-Corner [20].

II.3 Numerical methodology for the indentation test analysis

The load-depth curves obtained from the continuously recording by instrumented indentation test provide a "mechanical fingerprint" of the material's response to contact deformation [21]. It is therefore necessary to further process these curves to fully understand the mechanical properties of a material. In this section, the attention is focused on analyzing the loading part of the load-depth curves in order to consider the indentation size effect at the initial portion of loading. First, various traditional approaches to describe the loading-depth curves are presented. Then, an original methodology for the indentation curves analysis is proposed.

II.3.1 Analytical solution development of loading-depth curves

II.3.1.1 Kick's law

For geometrically similar indenters, a quadratic relationship between the load P and the indentation depth h is appropriate to describe the loading-depth curve. It is known as Kick's law [22]:

$$P = Ch^2, \quad (2.17)$$

where C is the loading curvature that depends on both the indenter shape and the material. The significance of this law is that the material hardness remains constant regardless of the applied force to the indenter. However, this simple quadratic relation is quickly become insufficient to describe the experimental curves, especially for the beginning part of the curves. In fact, the initial stage of the load-depth curve usually is no longer a perfect parabolic but rather a linear shape, which is due to the existence of the indentation size effect. But the model doesn't take account in the ISE phenomena. Several authors have reported that this law could not describe the beginning of the loading curve for several materials (*e.g.* aluminum, fused silica or ceramics…) [23] and proposed that the load-depth curve is more accurately described when the exponent in Kick's law is less than 2 [24,25].

II.3.1.2 Meyer's law

The first approach to describe the load-depth curve considering the indentation size effect phenomena is the Meyer's law [26]. The Meyer's law is expressed as:

$$P = Kd^n, \quad (2.18)$$

where P is the load, K is a material constant, d is the diameter of the remaining circle of contact by a spherical indenter and n is the Meyer's index. Thus the hardness could be calculated using the Equation (2.19):

$$H = \alpha P / d^2 = \alpha K d^{n-2} \quad (2.19)$$

where α is a constant. The relation indicates that the hardness should increase with the increasing of the diameter d when $n > 2$ and decrease with the increasing of the diameter d when n < 2 (*i.e.* ISE phenomena). And the hardness is independent to the depth when the n-value equal to 2. In this case, the ISE is not considered and the Meyer's law becomes to the Kick's law.

Initially, the Meyer's law was proposed for a spherical indenter with a known radius R as shown in Figure 7(a). The geometric relationship between the depth of indentation h and the diameter d is [27]:

$$d = 2\sqrt{h(2R-h)}. \quad (2.20)$$

To correspond to the loading-depth curve, it is reasonable to change the Meyer's law content using the depth h instead of the diameter d :

$$P = Kh^n. \quad (2.21)$$

With a pyramidal or conical indenter, the ratio of the length of the diagonal or radius of circle of contact to the depth of the indentation remains constant for increasing indenter load, *i.e.* the indenter is geometrical similar [19], as shown in Figure 7 (b). Several authors has [28,29] confirmed therefore that the modified Meyer's law Equation (2.21) could also be used for non-spherical indenters such as Berkovich, Cube-Corner or Conical indenters. This law is often used materials behavior, but due to the fact that n is generally non-integer, it was hard to find a convincing interpretation on how to connect this law to instrumented indentation testing [30]. Therefore, it is more suitable for the analysis from an empirical point of view [31].

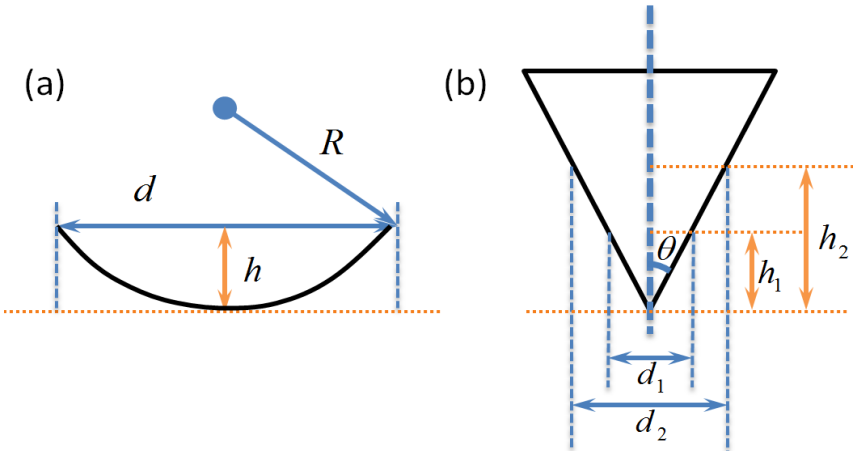

Figure 7: Indentation size for (a) spherical indenter and (b) sharp indenter.

II.3.1.3 Polynomial models

In order to overcome the difficulty arising from the fact that the exponent is usually not an integer in Meyer's law, several polynomial models were approached by correcting the Kick's law to describe the load-depth curves with the consideration of the ISE phenomena, *e.g.* Bernhardt model, Minimum resistance model and Proportional specimen resistance model (PSR model).

The Bernhardt model [32] was the first polynomial model for describing the load-depth curve. It was proposed to correct Kick's formula by adding a linear term, which aims to characterize the dependence of the load to the indentation depth at the initial stage of the loading curve:

$$P = \alpha_1 h^2 + \alpha_2 h\,, \tag{2.22}$$

where α_1 and α_2 are parameters related to the geometry of the indenter tip and the material properties. Bernhard explains the physical meaning of the linear and quadratic

terms of the equation (2.22) as the surface energy term and the volume energy term, respectively, based on the consideration of energy-balance.

Hays and Kendall also proposed another polynomial model basing the energy-balance point of view in 1973 [33]. They suggest that there is a minimum resistance force W on the surface, which is leads to the deviation of the Kick's law from the experimental curves at small depths and hence the observation of the ISE phenomena. The relation is:

$$P = W + K_{HK} h^2 \tag{2.23}$$

Recently, the proportional specimen resistance (PSR) polynomial model was established by Li and Bradt [34]. It is having a similar formula with the Bernhardt model, but different physical interpretations were proposed for the two constants α_1 and α_2. In the PSR model, the first term $\alpha_1 h^2$ is a load-independent coefficient and the second linear term $\alpha_2 h$ expresses the dependence of the surface elastic resistance on the indentation depth. The effect of the linear term on hardness is larger as the load or the depth is decreased. But the effect is negligible at higher load. This tendency of the change of hardness coincides with the indentation size effect.

As summarized by the work of Sangwal [35], various researchers have established this relationship by analyzing the force-displacement curves or the evolution of hardness with depth, obtained with sharp indenters. In this manuscript, the Bernhardt model is applied to develop a novel model because it is the first one to describe the loading-depth curve with the consideration of ISE phenomena using a polynomial series.

II.3.2 Original methodology for loading-depth curves analysis

II.3.2.1 Pre-treatment of the nanoindentation curves

The novel model is based on the treatment of the loading part of the nanoindentation curves. Three pre-treatments of the nanoindentation curves are carried out:

First, the loading part of the nanoindentation curves is extracted from the experimental measurements by limiting the load less than $0.8P_{\max}$ where $P_{\max}$ is the maximum experimental load. The threshold is set to $0.8P_{\max}$ because the curves present an intersection around this value. This truncation helps having a same final load for all the curves to avoid any bias when treating the data.

The second treatment consists in transforming the experimental indentation depth to an independent and identically distributed (i.i.d.) variable to avoid any artifacts during future statistical regression. Thus, the load is averaged each 20 nm to make each random i.i.d. depth having the same probability distribution.

The last treatment is to extract the contact depth h_c from the nanoindentation data using the Oliver and Pharr method as shown in Equation (2.15). Thus, the Bernhardt model can also be rewritten with the contact depth h_c instead of using the experimental depth h :

$$P = \alpha\left(H_0 h_c^2 + \beta h_c\right), \tag{2.24}$$

where α is constant that depends on the geometry of the indenter (α is equal to 24.56 for Berkovich indenter and 2.6 for Cube-Corner indenter), H_0 is the macro-hardness of the specimen, and β is the parameter related to the ISE (*i.e.* the linear part of the loading-depth curve).

II.3.2.2 Introduction of initial contact depth error

Theoretically, all the experimental loading curves can be described by the Equation (2.24), but it is not correctly fulfilled for real materials because the errors from the systematic detection of the first contact point or the presence of surface roughness. In our method, we assume that there is a deviation Δh_c between the experimental curve and the shape given by the Bernhardt model according to the indentation depth axis, as shown in Figure 7.

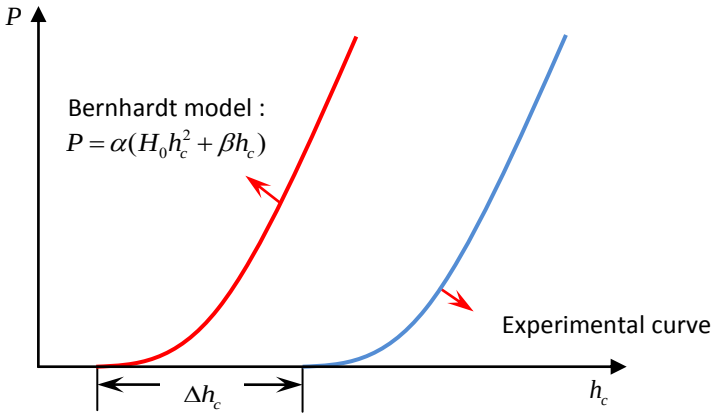

Figure 7: Diagram of the experimental loading-depth curve and the one simulated by Bernhardt model.

This deviation can be induced by a wrong detection of the first contact or the presence of roughness. By adding the deviation Δh_c to the contact depth h_c in Equation (2.24), the real loading-depth curves function therefore can be written as follow:

$$P = \alpha\left[H_0 \left(h_c + \Delta h_c\right)^2 + \beta\left(h_c + \Delta h_c\right)\right], \tag{2.25}$$

where Δh_c is the initial contact depth error.

Once Equation (2.24) is developed and reorganized, the following equation is obtained:

$$P = \alpha\left[H_0 h_c^2 + \left(2H_0 \Delta h_c + \beta\right) h_c + H_0 \Delta h_c^2 + \beta \Delta h_c \right]. \tag{2.26}$$

Equation (2.26) is the basis of the proposed method. It is considered as the best function to describe the experimental curve because of the introducing of the initial contact depth error as shown in Figure 8.

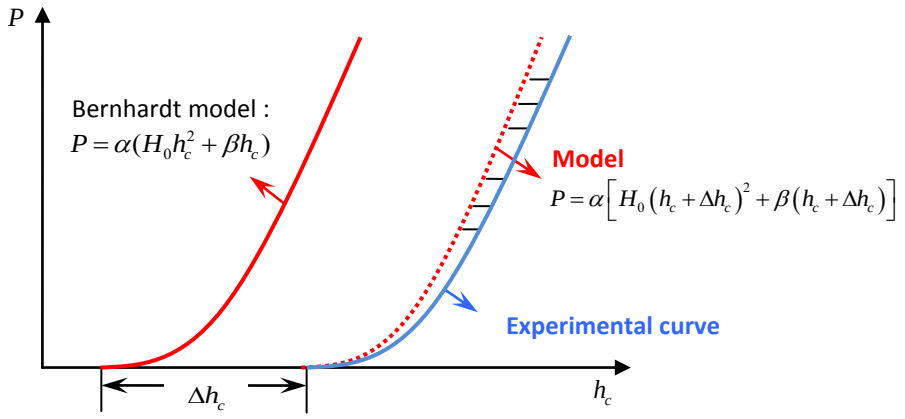

Figure 8: Diagram of the experimental loading-depth curve and the modeled loading-depth curve.

II.3.2.3 Minimization function

Besides the initial contact depth error, another innovative concept that the simultaneously analyzing several loading curves with a minimization function is also proposed in our model.

For the optimization, we consider a set of N experimental loading-depth curves. Then, one of these curves is selected arbitrarily among all the experimental curves as a reference one. We describe this reference curve with the Equation (2.26). Then, the macro-hardness H_0 , the ISE factor β and the initial contact depth error Δh_{ci} are determined by minimize the deviations (deviation of shape and deviation of position) between the reference curve predicted by Equation (2.26) and the other actual experimental curves. This calculation is made through the use of a least square regression analysis. It is a process to insure that the

difference between experimental and modeled loading-depth curves is minimized, as indicated in Equation (2.27).

$$\min_{H_0,\Delta h_1 \ldots \Delta h_N,\beta} \sum_{i=1}^{N}\sum_{j=1}^{M}\left\{P_{i,j} - \alpha\left[H_0 h_{c,j}^2 + \left(2H_0\Delta h_{c,i} + \beta\right)h_{c,j} + H_0\Delta h_{c,i}^2 + \beta\Delta h_{c,i}\right]\right\}^2, \quad (2.27)$$

where i is the i^{th} loading curves and j refers to the j^{th} couple point (P,h) of one loading curve.

Here, the macro-hardness H_0 and the ISE factor β are homogeneous for the whole specimen. It means that the H_0 and β remain constant whatever the selected curve. By contrast, the deviation Δh_{ci} is different for each curve i. Thus, this simultaneously treating for all the curves only gives one set of mechanical parameters.

II.3.2.4 Bootstrap

To be able to guarantee the accuracy of the results given by our method, we determine the value of H_0 and β with their respective confidence intervals using a random sampling technique: Bootstrap [36,37]. This technique is to create new samples from original data using a random sampling with replacement. Here, a double Bootstrap, repeated 1000 times, is performed on the original experimental loading curves of each specimen. First, from N experimental curves, the equivalent numbers of curves are drawn by random sampling with replacement (first Bootstrap). Then for each curve containing M independent and identically distributed (P,h) points, the equivalent numbers of points are drawn by random sampling with replacement (second Bootstrap). This allows us to obtain N curves to statistically represent the variable of nanoindentation tests in different surface zone or a possible heterogeneity of the material. It is these N curves that are applied to perform the optimizations in Equation (2.27).

Chapter III Robustness of the numerical model

III.1 Overview

In this chapter, the robustness of the numerical model is evaluated from three aspects. Firstly, the numerical method is compared with some “intermediary” methods in Section III.2. The estimated hardness of the material with different methods is compared to confirm that the consideration of the initial contact depth error and ISE, and the simultaneous treatment are necessary in the indentation curves analyzing model. Secondly, in Section III.3, a multi-scale surface analysis method and a linear regression analysis method are used to quantify the relation between the standard deviation of the initial contact depth error and the surface roughness parameter calculated with different evaluation lengths, The aim of this part is to verify the ability of numerical model to calculate the mechanical properties with the consideration of the surface roughness effect. Finally, in addition to the hardness of the specimens, the elastic properties Young’s modulus is also estimated by the numerical method in Section III.4.

In order to verify the reliability of the numerical model for different materials and surface treatment methods, the above three studies are realized through analyzing the instrumented indentation curves performed on three different specimens: polished austenitic stainless steel 316L, sandblasted aluminum-based alloy 2017A, and polished aluminum-based alloy 2017A, separately. The relationships between the initial contact depth error and root mean square surface roughness parameter R_q for each specimen are studied in order to understand the surface effects in indentation testing.

III.2 Comparison of the numerical model with the intermediary methods

In this part, the robustness of the proposed methodology is evaluated by comparing our approach to the methods called "intermediary" in the sense that these models do not take into account certain assumptions (such as the presence of an ISE), to evaluate their impact on the determination of hardness. By analyzing the origin of the initial contact depth error, a quantitative relationship between the surface roughness parameter and the initial contact depth error is proposed.

The numerical model is applied to the instrumented indentation curves performed on 11 stainless steel specimens (316L) having rough to mirror-like surface. The surfaces of the

specimens are achieved according to the polishing method described in Section II.2.2. And 100 nanoindentations tests are performed for each specimen. Figure 9 shows the 100 experimental loading-depth curves for 316L stainless steel specimens polished with grit paper 4000 and 80, respectively. The curves of the specimen polished with grit paper 80 are more scatter than those of the specimen polished grit paper 4000.

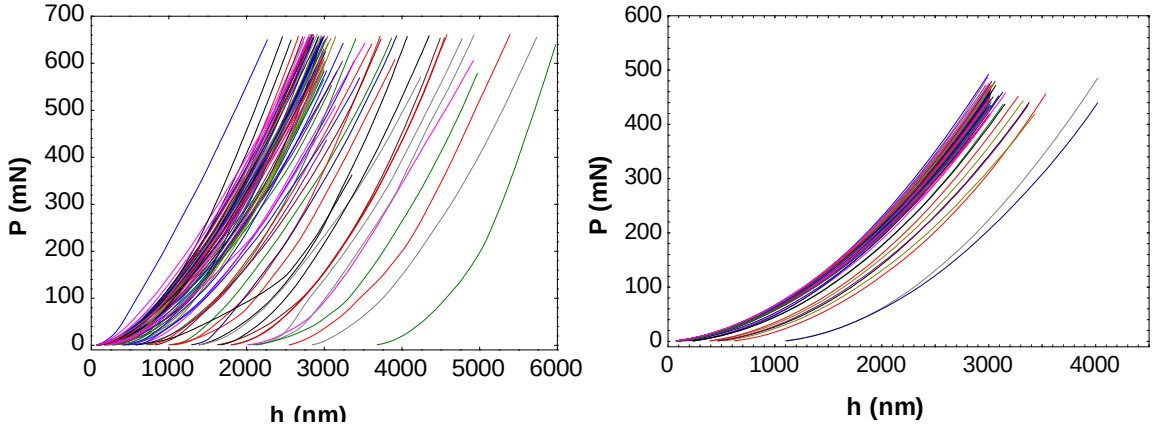

Figure 9: Experimental loading-depth curves for 316L stainless steel specimens polished with grit paper 80 (left) and 4000 (right), respectively.

III.2.1 Presentation of the intermediary methods

In order to check the validity of the proposed approach, five types of intermediary methods for the analyzing of indentation curves are built. These methods are qualified as "intermediary" because they come from several variations of the previous treatment methods.

For easier comparisons, the proposed method as described by Equation (2.27) in Chapter II is denoted as "**Method A**".

$$\min_{H_0,\Delta h_1 \ldots \Delta h_N,\beta} \sum_{i=1}^{N}\sum_{j=1}^{M}\left\{P_{i,j} - \alpha\left[H_0 h_{c,j}^2 + \left(2H_0\Delta h_{c,i} + \beta\right)h_{c,j} + H_0\Delta h_{c,i}^2 + \beta\Delta h_{c,i}\right]\right\}^2, \qquad (2.27)$$

where N is the number of curves and M is the number of points for each curve with a double-Bootstrap.

There are three main features for this model: the simultaneous treatment of all the experimental curves, taking into account the factor of ISE phenomena and the location of the curves is set by a relative referential and not an absolute one. In fact, the curves are represented by their deviations from a reference curve (*i.e.* the difference between the

actual experimental curves and the simulated one with Bernhard model, as defined in Section II.3.2.2), and then they are identified with a particular value Δh_c.

In order to test the influence of the referential choice on the results, a second method is created: **Method B**. The latter uses the same assumptions as Method A, except that the referential choice is absolute, *i.e.* the location of the curves is defined as the point where the load is equal to zero. Thus, all the experimental loading curves are first translated to zero along the x-axis before the minimization. Then, all the loading curves are treated simultaneously as Equation (3.1):

$$\min_{H_0,\beta} \sum_{i=1}^{N} \sum_{j=1}^{M} \left[P_{i,j} - \alpha \left(H_0 h_{c,j}^2 + \beta h_{c,j} \right) \right]^2 . \tag{3.1}$$

The **Method C** is based on the use of a relative referential Δh_c and takes into account the ISE factor β as Method A, but treats the curves individually. It is therefore similar to the methods usually used where a set of material parameters is calculated from a single experimental curve. When multiple curves are present, these methods treat them separately, and then compute the material properties (*e.g.* hardness) by averaging the values given by the different curves. In the case of the processing of 100 curves, the material parameters are firstly identified separately for each curve i using the Equation (3.2):

$$\min_{H_0,\Delta h_i,\beta_i} \sum_{j=1}^{M} \left\{ P_{i,j} - \alpha \left[H_{0,i} h_{c,j}^2 + \left(2 H_{0,i} \Delta h_{c,i} + \beta_i \right) h_{c,j} + H_{0,i} \Delta h_{c,i}^2 + \beta_i \Delta h_{c,i} \right] \right\}^2 . \tag{3.2}$$

where j refers to a point in curve number i and $\Delta h_{c,i}$ is the deviation of curve i from the reference curve simulated with Bernhardt law. $H_{0,i}$ and β_i are the macro-hardness and the ISE factor for curve i.

Once this minimization completed for all the one hundred experimental curves, the average macro-hardness and the ISE factor is calculated as follows:

$$\overline{H_0} = \frac{1}{N} \sum_{i=1}^{N} (H_{0,i}) , \tag{3.3}$$

$$\overline{\beta} = \frac{1}{N} \sum_{i=1}^{N} (\beta_i) . \tag{3.4}$$

The **Method D** involves a simultaneous treatment for all the curves but ignores the ISE factor and does not consider any initial contact depth error ($\Delta h_c = 0$). It means that the curves are described by the Kick's law. The minimization equation can be summed up:

$$\min_{H_0,\beta} \sum_{i=1}^{N}\sum_{j=1}^{M}\left[P_{i,j} - \alpha(H_0 h_{c,j}^2)\right]^2 . \quad (3.5)$$

The **Method E** also ignores the ISE but takes into account the initial contact depth error and uses a simultaneous treatment. The minimization equation can be written as follow:

$$\min_{H_0,\Delta h_1 \ldots \Delta h_N} \sum_{i=1}^{N}\sum_{j=1}^{M}\left\{P_{i,j} - \alpha\left[H_0 h_{c,j}^2 + 2H_0 \Delta h_{c,i} h_{c,j} + H_0 \Delta h_{c,i}^2\right]\right\}^2 . \quad (3.6)$$

Finally, the **Method F** considers the ISE and treats the curves simultaneously but does not consider any initial contact depth error ($\Delta h_c = 0$). The equation of this method is therefore as follows:

$$\min_{H_0,\beta} \sum_{i=1}^{N}\sum_{j=1}^{M}\left[P_{i,j} - \alpha\left(H_0 h_{c,j}^2 + \beta h_{c,j}\right)\right]^2 . \quad (3.7)$$

For more clarity, Table 4 summarizes the different method and hypotheses studied here.

Method	Type of treatment	ISE factor β	Deviation Δh_c
A	Simultaneous	$\beta \neq 0$	Use of Δh_c
B	Simultaneous	$\beta \neq 0$	Use of $P = 0$
C	Individual	$\beta \neq 0$	Use of Δh_c
D	Simultaneous	$\beta = 0$	No deviation
E	Simultaneous	$\beta = 0$	Use of Δh_c
F	Simultaneous	$\beta \neq 0$	No deviation

Table 4: Summary the methods with different hypotheses.

III.2.2 Influence of the referential choice: comparison of Method A and B

Normally, the instrumented indentation curves always show low reproducibility, even for a homogeneous specimen. An important source of the error in indentation tests is the first contact point identification. In spite of the accuracy of the measurement devices is improvement, the position of the first contact point remains uncertain. The bad identification for the first contact point (*i.e.* the position of h = 0) can seriously deteriorate the identification of the mechanical properties such as the hardness because the first contact point is the reference point for recoding the indentation depth. The usual methods generally define the position of the reference point through a specific value or point (*e.g.* h = 0 when P = 0). It is an absolute referential as Method B which is different with the proposed methodology (Method A) using a relative referential.

Figure 10 represents the minimization of the dispersion of the loading-depth curves for the specimen 4000, using Method A and Method B. Compared with Figure 9 displaying the experimental loading-depth curves, there is an important decrease of the deviations between the loading-depth curves using both methods. With Method A, the curves are difficult to distinguish. On the contrary, Method B gives a more "important" scatter. This first comparison underlines the interest in considering the loading-depth curves with a relative referential instead of an absolute chosen value.

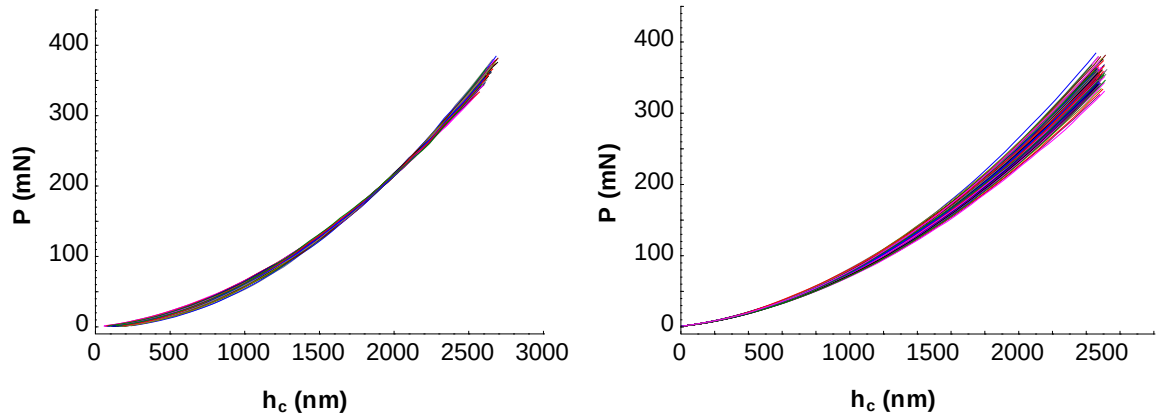

Figure 10: Processing of the experimental loading-depth curves using Method A (left) and Method B (right)for 316L stainless steel specimen polished with grit paper 4000.

Thanks to the use of double Bootstrap for both treatment methods, the average values and the standard deviations are calculated for the macro-hardness and the ISE factor. Table 5 summarizes the results obtained for Specimen 4000. The macro-hardness average values are very close. Method B gives a macro-hardness similar to our method. On the other hand, Method B has a standard deviation which is 2.5 times higher than the one given by our method (Method A). Thus, it shows that considering a relative reference (i.e. respect to the Bernhard law) in curves analyzing processing will give a better accuracy for the determination of material parameters than methods based on the consideration of an absolute value.

Method	H_0 (GPa)		β (mN/nm)	
	Average	Standard deviation	Average	Standard deviation
A	1.86	0.004	1114	30.02
B	1.84	0.01	1271	29.2

Table 5: Average and standard deviations of macro-hardness (H_0) and ISE factor (β) obtained by Methods A and B for 316L stainless steel specimen polished with grit paper 4000.

This difference in standard deviation is less marked in the case of the determination of the ISE factor. The average values found for the ISE factor are very close. The standard deviations are also nearly identical.

To check the validity of the results for the ISE factor value, several indentation prints made on Specimen 4000 are observed with interferometric microscopy. All the prints show pile-up. An example is given in Figure 11. Pile-up observation indicates that positive values should be identified for the ISE factor [38]. As a consequence, both methods correctly describe the material behavior.

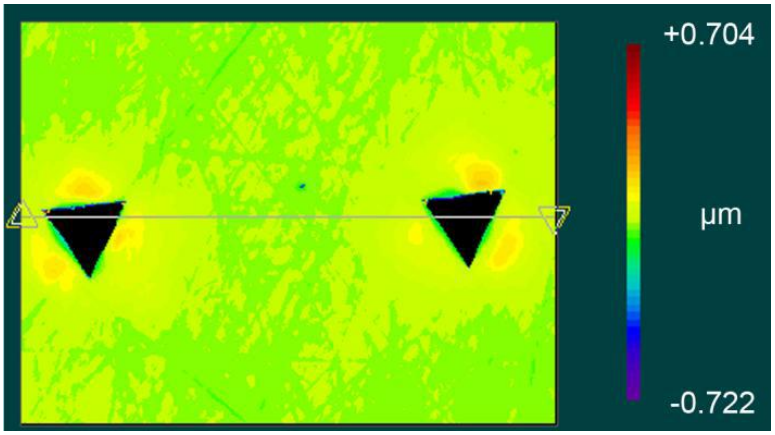

Figure 11: Observation of pile-up occurrence in 316L stainless steel specimen polished with grit paper 4000 using interferometric microscopy

III.2.3 Influence of simultaneous treatment: comparison of Method A and C

As previously stated, our method involves a simultaneous treatment of all the experimental curves for determining the macro-hardness H_0 and the ISE factor β. This point is different with more conventional methods where a set of material parameters is identified for each curve and then the material properties is obtained by averaging all the data. This section is dedicated to identify the robustness of the simultaneous treatment method by comparing the results given by our method (Method A) with those obtained by Method C (representing the model with an individual treatment).

Both processing methods are based on the optimization of a given function using a gradient descent algorithm. A mathematical optimization consists in minimizing the considered function by systematically choosing values in a defined domain. Due to the high nonlinearity of Equation 2.27 in Section II.3.2.3, an iterative scheme of optimization has to be used [39,40]. The Levenberg–Marquardt Algorithm is a very popular curve-fitting

algorithm used in many software applications for solving generic curve-fitting problems. However, this algorithm does not guarantee the obtaining of the global minimum. Therefore, as the variations of the function remain unknown, several starting points must be tested to avoid identifying a local minimum instead of a global minimum. When using different starting points, our method gives similar results (well posed problem). On the opposite, the method treating the curves separately leads to different results (ill-posed problem). The loading-depth curves after data processing with Method C, from 3 different starting points, is shown in Figure 12.

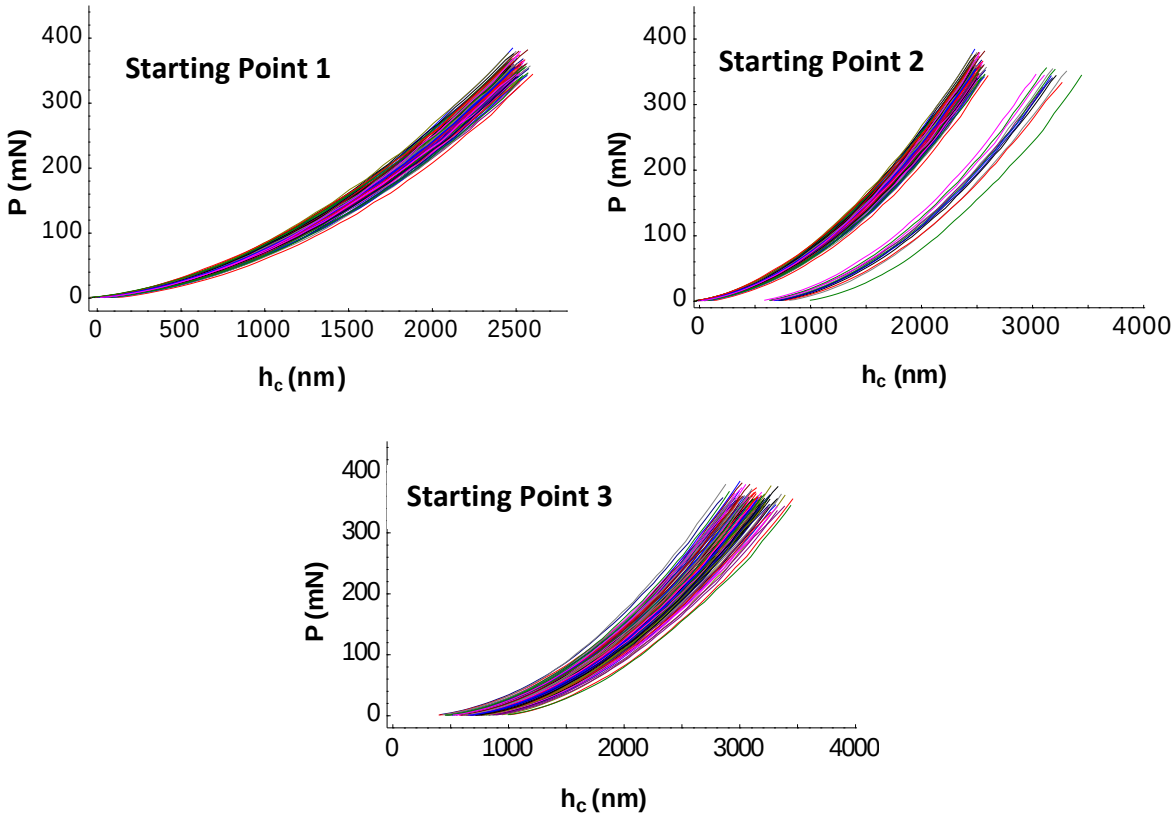

Figure 12: Processing of the experimental loading-depth curves using Method C with three different starting points 1, 2 and 3.

Among the results obtained with the three starting points, the starting point 1 gives the best minimization of the dispersion curves. However, the curves are much more dispersed than Method A (see Figure 10). The minimization obtained by the starting point 2 gives rise to two subpopulations. These preliminary observations reveal that the method treating the curves separately is dependent on the initial values and thus unstable compared to the proposed approach.

Table 6 further details the results given by the three starting points and indicates again the average and standard deviation values found with our model for the macro-hardness and ISE factor. Whatever the method or the tested starting point, the average values obtained for the macro-hardness are nearly identical. For the method treating all the curves separately, the macro-hardness average is equal to 1.852 GPa while the standard deviations spread out between 0.007 and 0.008 GPa. These values remain, certainly, low but only because hardness is determined using one hundred experimental curves. Moreover, the standard deviations calculated with Method A are approximately twice lower than those calculated using Method C. If the experimental data follow a Gaussian hypothesis, it means that four times less experimental loading curves are needed with our method (Method A) to achieve the same standard deviation as that obtained with Method C.

Method	H_0 (GPa)		β (mN/nm)	
	Average	Standard deviation	Average	Standard deviation
A	1.863	0.004	1114	30
C (Starting point 1)	1.852	0.007	1153	25
C (Starting point 2)	1.852	0.008	914	63
C (Starting point 3)	1.852	0.008	-1157	26

Table 6: Average and standard deviation of macro-hardness (H_0) and ISE factor (β) calculated using the simultaneous treatment method (Method A) and the individual treatment method (Method C) with three different starting points.

The average values of ISE factor found for the three starting points are very different. The starting point 1 gives an average value equal to 1153 mN/nm which is similar to the one given by our method. The standard deviation obtained with this starting point is also similar to Method A. In contrast, the starting point 2 gives an average value which is 1.3 smaller and standard deviation 2.5 greater than that given by the starting point 1.

Figure 13 shows the distribution of ISE factors obtained for each experimental curve analyzed with Method C and the second starting point. Two subpopulations of ISE factor can be distinguished. The first one shows a negative ISE factor while the second one has a positive ISE factor. These results correspond to the two distinguished subpopulations that are presented in Figure 12. However, the interferometric microscope observations have shown that only piling-up was presented around the indentation impression, which means the ISE factor should be a positive value [38]. Similarly, the ISE factor identified with the third starting point is also incorrect since a negative average value is identified with a standard

deviation of the same order of magnitude as the one given by our model. It highlights the lack of robustness of the Method C treating the curves separately.

The standard deviations calculated using starting points 1 and 3 are slightly lower than the one given by our model. This tendency can be explained by a better fit of the curves with Method C. In method C, each curve is fitted using a different value for the macro-hardness and the ISE factor. Conversely, in our model, for processing all the curves simultaneously, the mechanical properties are supposed to be same.

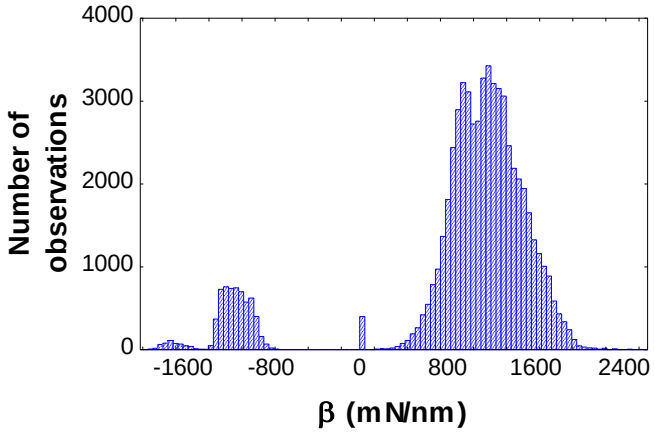

Figure 13: Distribution of ISE factors obtained with Method C and the starting point 2.

It is important to note that, whatever the method are chosen for processing the loading-depth curves, the best results for the ISE factor and the macro-hardness are found when the dispersion of the loading-depth curve is best minimized. To explain this appearance, the values of the deviations between the actual experimental curves and the shape predicted by Bernhardt model are studied in function of the ISE factor value. 1000 couples of values are obtained using a Bootstrap enabling a random sampling with replacement. Figure 14 shows the values between the deviations and the ISE factor obtained with (a) Method C from the first starting point and with (b) Method A.

On Figure 14(a), the deviations between the curves decrease as the ISE factor increases from 0 to 2500 mN/nm for deviations ranging from -1200 to 200 nm. This relationship clearly indicates that in Equation 3.2, the ISE factor value depends on the value of the deviations between the curves and also related to the chosen model. These results explain why different results are obtained when using different starting points.

On the other hand, the deviation values and the ISE factor seem to be independent for the Method A in Figure 14(b). Indeed, the ISE factor only varies from 1010 to 1220 mN/nm for the deviations ranging from -1100 to 20 nm. It proves that the ISE factor value

does not depend on the deviation value. This last observation confirms that treating all the loading curves as a whole endows the method with robustness.

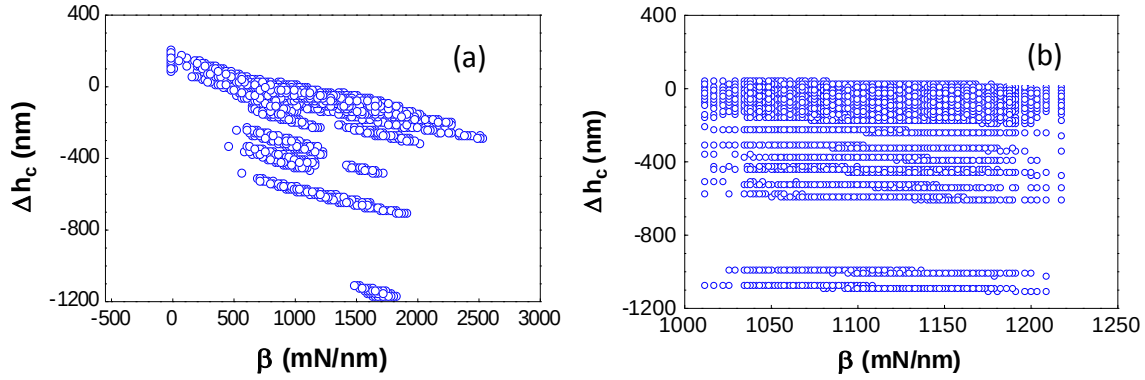

Figure 14: Values of the deviations Δh_c as function of the ISE factor β obtained with (a) Method C and the starting point 1 and (b)Method A.

III.2.4 Influence of the ISE contribution: comparison of Methods A, D, E and F

The improvements brought by our method have mainly been assessed based on a statistical study. The robustness of the method is examined by its application to the analysis of eleven polished specimens with different grades. The proposed method is now compared to methods D, E and F which also treat the curves simultaneously but considering different hypothesis for the ISE and the initial contact depth error. The macro-hardness for each abraded specimen calculated with the method A, D, E or F is depicted in Figure 15 *versus* the specimen grit paper number.

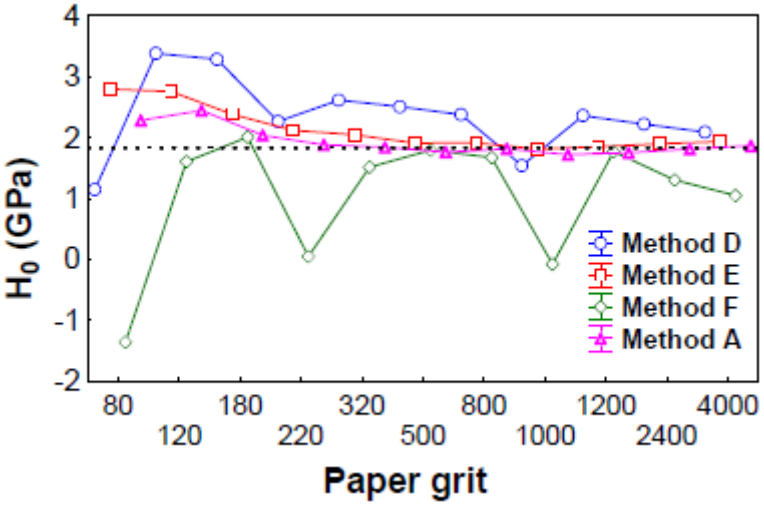

Figure 15: Macro-hardness estimation for each abraded specimen calculated with the method A, D, E or F.

Method F gives absurd values: a negative macro-hardness is found for specimen 80 and equal to zero for specimen 220 and 1000. The other macro-hardness values are also underestimated as a value equal to 1.00 GPa identified for specimen 4000 while the experimental measurements gives 1.83 GPa. On the other hand, Method D globally overestimates the macro-hardness, except for specimen 80 whose value is abnormally low as it is equal to 1.20 GPa.

Method E and A show a variation of the macro-hardness, which meets expectations. Indeed, polishing with low grit papers (*i.e.* high abrasive size) hardens the surface of the material while these effects are less important with high paper grit (*i.e.* low abrasive size). The macro-hardness values are globally higher when calculated using Method E instead of Method A. For specimen 80, Method E gives a macro-hardness equal to 2.80 GPa while 2.20 GPa is obtained with Method A. The macro-hardness values found for specimen 4000 are closer as Method E gives 1.94 GPa and Method A gives 1.89 GPa. The tendency to overestimate the macro-hardness highlights the importance of considering ISE factor when analyzing the loading curves. But against expectations, Method A gives a slightly lower macro-hardness for specimen 80 than for specimen 120. In order to explain this phenomenon, observations are made using Scanning Electron Microscopy. Figure 16 shows the indentation imprints made on specimen 80. It can be noticed that the nanoindentation imprint is less important than the one given by specimen 4000 (Figure 11). Due to the important high cross groove depth, the specimen behaves as a porous material which leads to measure a smaller macro-hardness.

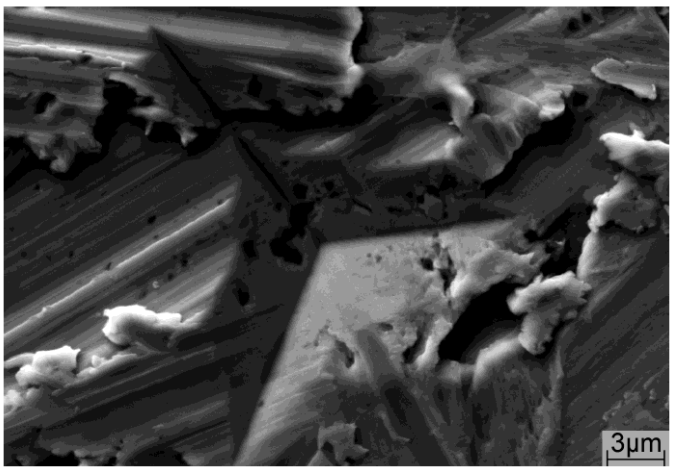

Figure 16: Observation of the nanoindentation prints for 316L stainless steel specimen polished with grit paper 80 using Scanning Electron Microscopy.

Figure 17 shows the ISE factor evolution for the different abraded specimens obtained with Method A or Method F. It can be noticed that Method A gives an ISE factor that decreases from about 4000 mN/nm to 1500 mN/nm with an increase of the paper grit number. Method F gives fluctuating values with particularly high ISE factor for Specimen 80, 200 and 1000.

We have observed previously that a decrease in the paper grit number gives a higher macro-hardness. This phenomenon is caused by the hardening of material. Oliver *et al.* [41] and Alcalá et al. [42] have shown that the pile-up is more important for materials that have a low ability to hardening. Thus, the pile-up should be more important in specimens polished with low paper grit numbers. Iost *et al.* [38] suggests that a higher pile-up gives a greater ISE factor value. This observation corroborates the results given by our method as a greater ISE factor is found for the polished samples with the lower grades (Figure 17).

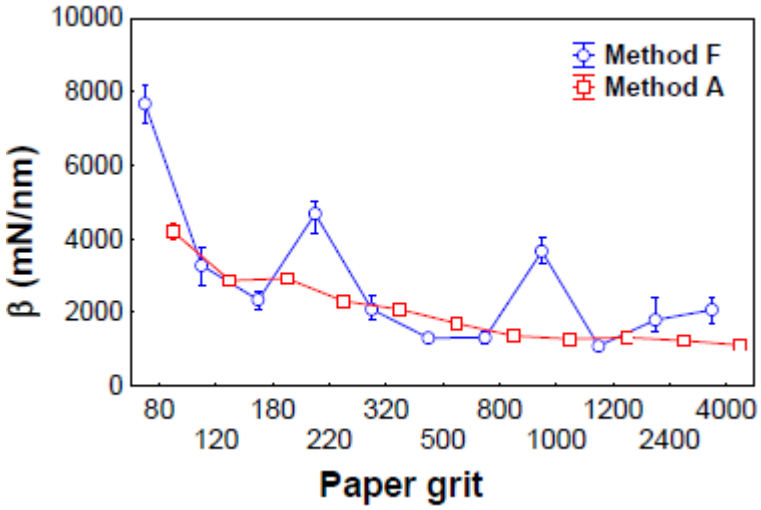

Figure 17: ISE factor values calculated for each abraded specimen using Method A and F.

The previous studies have proved that the robustness of our method is greater than other intermediary methods due to the simultaneous treatment for all the curves, the consideration of ISE factor, and the introduction of the initial contact depth error, *i.e.* the deviations between the shape of the curves and that predicted by the Bernhardt law. But the origin of the initial contact depth error is not clarified. Ostensibly, the initial contact depth error is a representative of the dispersion of the loading-depth curves. However, it is important to note that various origins may result in the dispersion of the loading-depth curves. For crystalline materials, it can be caused by problems of preparation (hardening the surface, the presence of oxides) of a defect of the indenter tip, the presence of roughness or

even a poor estimate of the contact area (presence a pile-up). In our case, a correlation between the surface roughness and the dispersion of loading-depth curves is observed in Figure 9, *i.e.* the dispersion of the curves for smooth surface is significantly smaller than the one for rough surface. Thus, after the investigation of the robustness of our method, we will study the relation between the initial contact depth error and the surface roughness.

III.2.5 Relation between initial contact depth error and surface roughness

Using the eleven abraded specimen, the effect of roughness on the initial contact depth error Δh_c is studied. For each specimen, using the one hundred loading curves and a double Bootstrap, the standard deviation of Δh_c is computed. The calculated standard deviations of Δh_c are then studied as a function of the root mean square (RMS) roughness parameter Rq for each abraded specimen. Here the RMS roughness parameter Rq is given by the standard deviation of the z-values for the surface profile, where z-value indicates the vertical height of the surface as shown in Figure 18.

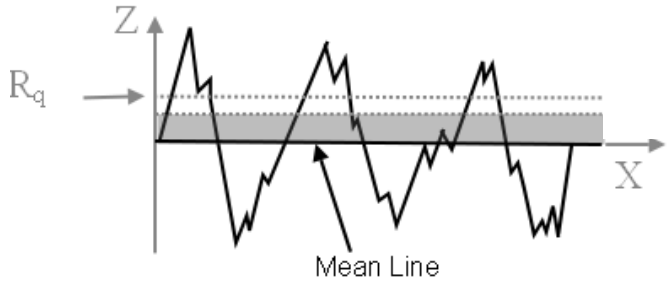

$$R_q = \sqrt{\frac{1}{n}\sum_{i=1}^{n}(Z_i - \overline{Z})^2}$$

Figure 18: Schema of root mean square roughness parameter Rq.

Finally, a linear relationship between the standard deviation of the initial contact depth error and the roughness parameter Rq is found, as shown in Figure 19. The standard deviation of initial contact depth error Δh_c increase from about 25 nm to 210 nm when the RMS surface roughness parameter Rq increases from about 10 nm to 310 nm. A same order of magnitude is observed whatever the studied abraded specimen. It shows that there is a significant connection between the initial contact depth error and the surface roughness. This final study corroborates the interest of the proposed method.

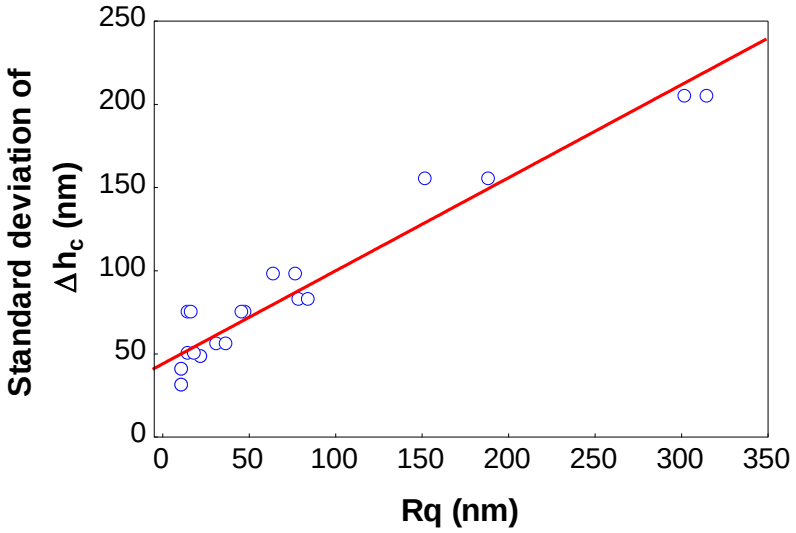

Figure 19: Standard deviation of the initial contact depth error *versus* root mean square surface roughness parameter Rq.

III.2.6 Conclusions

Comparing the assumptions of our method with the usual considerations (use of a single curve for the calculations of material parameters), we highlighted the importance of the dispersion of indentation curves and its influence on the identification of mechanical parameters such as hardness. The results show that the improvement of the accuracy in the identification of mechanical parameters can be made only through the consideration of the macro-hardness and the ISE factor together and through the evaluation of the impact of the initial contact depth error on the indentation data. The linear relationship between the initial contact depth error and surface roughness suggests the origin of the initial contact depth error. It proves that the effect of surface roughness on the indentation data can be corrected by the consideration of the initial contact depth error in the treatment processes of loading-depth curves for the stainless steel specimens 316L.

III.3 Multi-scale analysis of surface roughness for instrumented indentation analysis

The effect of the surface roughness on instrumented indentation data has been shown in the Section III.2. A significant correlation between the surface roughness and the initial contact depth error is found for the specimen 316L. However, the surface roughness parameter is very sensitive to the evaluation length which is defined as the length of surface profile used for the measurement of surface roughness. As mentioned in Section II.2.4, the roughness parameters estimated from different evaluation lengths will present different degrees of the surface roughness and waviness, and thus will produce different surface effect on the instrumented indentation analysis. Therefore, a multi-scale surface roughness analysis method is necessary to be achieved in our studies in order to find the most suitable evaluation length for roughness parameter estimation in instrumented indentation analysis.

In this part, the proposed method is firstly applied to the experimental nanoindentation curves of the four sandblasted 2017A specimens with different surface roughness. The specimens are named as S1, S2, S3 and S4, which has been defined in Section II.2.2. It is worth to note that both the material and the surface generation method of the specimens are different with the previous one in Section III.2. Then the multi-scale analysis method for surface roughness estimation is used to find the best correlated relation between the surface roughness and the indentation data. Moreover, the effect of initial contact depth error on the mechanical properties is studied by comparing the results obtained from the proposed model in two conditions: (a) $\Delta h_c = 0$ (not minimize the deviations of curves, initial contact depth error is zero) or (b) $\Delta h_c \neq 0$ (minimize the deviations of curves with the initial contact depth error) with Equation (2.27).

$$\min_{H_0,\Delta h_1 \ldots \Delta h_N,\beta} \sum_{i=1}^{N}\sum_{j=1}^{M}\left\{P_{i,j} - \alpha\left[H_0 h_{c,j}^2 + \left(2H_0\Delta h_{c,i} + \beta\right)h_{c,j} + H_0\Delta h_{c,i}^2 + \beta\Delta h_{c,i}\right]\right\}^2, \quad (2.27)$$

Figure 20 plots the experimental loading-depth curves (left) and the minimization of the dispersion of the loading-depth curves with the initial contact depth error (right) for specimen S4. Obviously, the shifted curves are closer than the original experimental curves. It suggests that the proposed method is also available on the specimens with another work-

hardening behavior (different material) or with another residuals stress (surface generation processing).

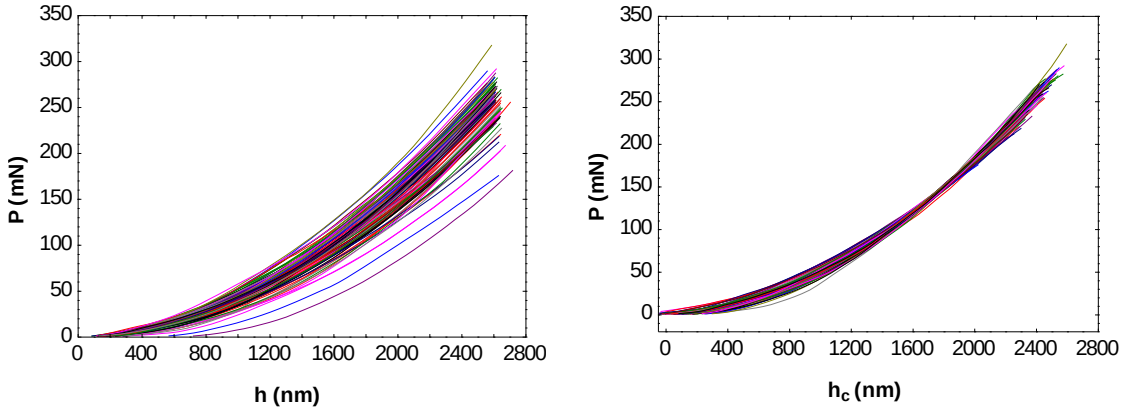

Figure 20: Experimental loading-depth curves (left) and the processing of the experimental loading-depth curves with proposed method considering the initial contact depth error (right) for the specimen S4.

The distribution of the initial contact depth error for each sandblasted 2017A specimen calculated based on the statistical method using a double Bootstrap is shown in Figure 21. It could be observed that the standard deviation of the initial contact depth error, which could be described as the width of red fitting line, decreases from specimen S1 to S4. For this reason, the investigation of relationship between the roughness and the standard deviation of initial contact depth error is valuable for quantifying the effect of surface roughness on nanoindentation data.

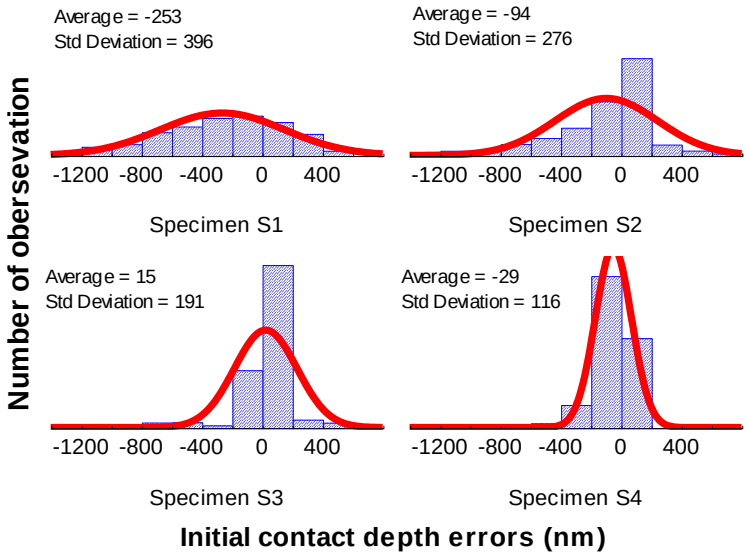

Figure 21: Distribution of the initial contact depth error for each sandblasted 2017A specimen.

III.3.1 Multi-scale surface roughness analysis

The evaluation length of surface profile has a critical effect on the roughness study. Indeed, it was observed that different evaluation lengths will give different roughness parameters [43,44]. The initial roughness profiles were experimentally measured with a given evaluation length (1000 µm). However, the suitability of this given evaluation length for studying the relationship between the surface roughness and instrumented indentation data is open to question. Hence, the aim of the multi-scale surface profile treatment is to find a suitable evaluation length of the surface roughness in instrumented indentation study. In this treatment, the topographic profile was divided into equal parts whose length is the evaluation length. Then a multi-scale surface roughness analysis for each original profile was carried out as described in section II.2.4. For a same original topographic profile, the profiles rectified with different evaluation lengths are strongly different. An example of the profiles recalculated with two different evaluation lengths (15µm and 521 µm) for each sandblasted 2017A specimen has been shown in Figure 22.

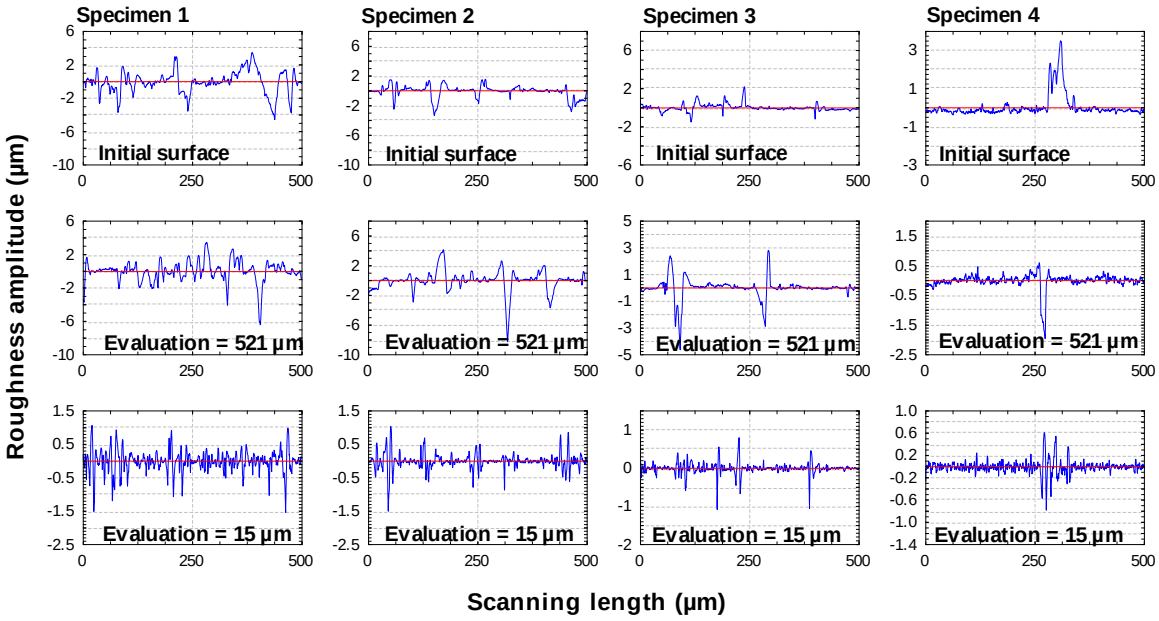

Figure 22:Multi-scale profile reconstructions corresponding to different evaluation length for each sandblasted 2017A specimen

The y axis presents the roughness amplitude which is the vertical distance of the surface profile (bleu one) from the surface mean line (red one). The x axis is the scanning length of the surface profile. The figure show that the roughness amplitude varies from -1.5 µm to 1 µm for the evaluation length equal to 15 µm, while it varies from -6 µm to 4 µm for

the evaluation length equal to 521 µm. It means that comparing with the surface profile calculated with a shorter evaluation length (15 µm), the profile calculated with the longer evaluation length (521 µm) appears more waviness.

To quantify the effect of evaluation length on the surface roughness, the surface height parameter root mean square R_q is calculated with different evaluation length, as shown in Figure 24. For each specimen, the quadratic roughness parameter increases with an increasing evaluation length until an asymptotic value is arises, that the corresponding evaluation length is around 170 µm. A probable reason is that: in the multi-scale surface roughness analysis method, the surface profile heights of a homogeneous and isotropic material are usually considered as a random variables, and the vertical surface height are analyzed statistically with the height probability distribution function which conforms to a Gaussian distribution as shown in Figure 23. The root mean square roughness parameter Rq is a quantitative measurement of the height probability and it is just the standard deviation of the Gaussian distribution (see Figure 18). Normally, the standard deviation of the Gaussian distribution increases with the increasing of evaluation length. But it will achieve a stable situation after the evaluation length is higher than a special value, which may be depended on the material and surface generation process (e.g. 170 µm for sandblasted 2017A). In this case, even the evaluation length is increased, it just produces an increasing observation number of the distribution, and the standard deviation of the Gaussian distribution (*i.e.* roughness parameter Rq) is not changed. However with this special evaluation length, the surface texture may consist of too much waviness than roughness (Figure 22). When considering the surface texture as a source of error in the evaluation of instrumented indentation experiments, only the roughness has to be taken into account.

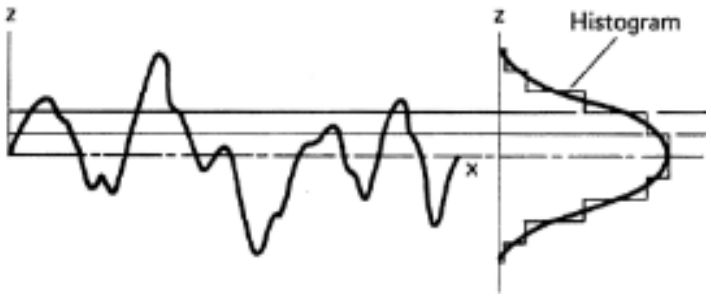

Figure 23: Schema of surface profile corresponds to a Gaussian distribution.

Moreover, comparing the four specimens, it can be observed that the surface roughness produced by different sandblasted parameters decreases from S1 to S4 whatever the evaluation lengths. It means that a higher jet pressure, shorter distance and bigger angle in sandblasting test produce rougher surface (higher R_q).

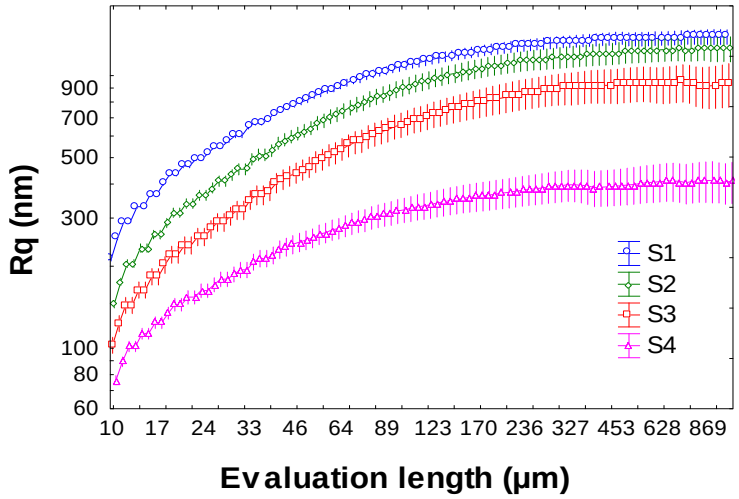

Figure 24: Evolution of the root mean square roughness (Rq) *versus* the evaluation length for each sandblasted 2017A specimen.

As described in the previous paragraph, the evaluation length is an important factor on studying the surface roughness. Hence, the primary issue is to find the most appropriate evaluation length for roughness analysis in the instrumented indentation study. Using different evaluation lengths for each specimen, several calculations of surface roughness parameter Rq have been done (Figure 24). Some values of Rq for each specimen calculated with the evaluation lengths equal to 15, 170 and 521 µm are listed in Table 7.

RMS roughness Rq (nm)	S1	S2	S3	S4
Evaluation length = 15 µm	339	218	169	97
Evaluation length = 170 µm	1110	864	600	252
Evaluation length = 521 µm	1169	984	600	225

Table 7: Root mean square surface parameter Rq calculated with evaluation length equal to 15, 170 and 521 µm, separately.

The instrumented indentation curves have been analyzed with proposed method and the distribution of the initial contact depth error for each specimen has been shown in Figure 21. The standard deviations of the initial contact depth error from S1 to S4 are 396, 276, 191 and 116 nm, separately. Then the linear regressions between the calculated surface

roughness R_q and the standard deviation of the initial contact depth error for each evaluation length have been studied in order to investigate a possible correlation between these two quantities. The corresponding linear correlation coefficients (R^2) are calculated. For example, the relationships between these two quantities when the evaluation length is 15, 170 and 521 µm are shown in Figure 25.

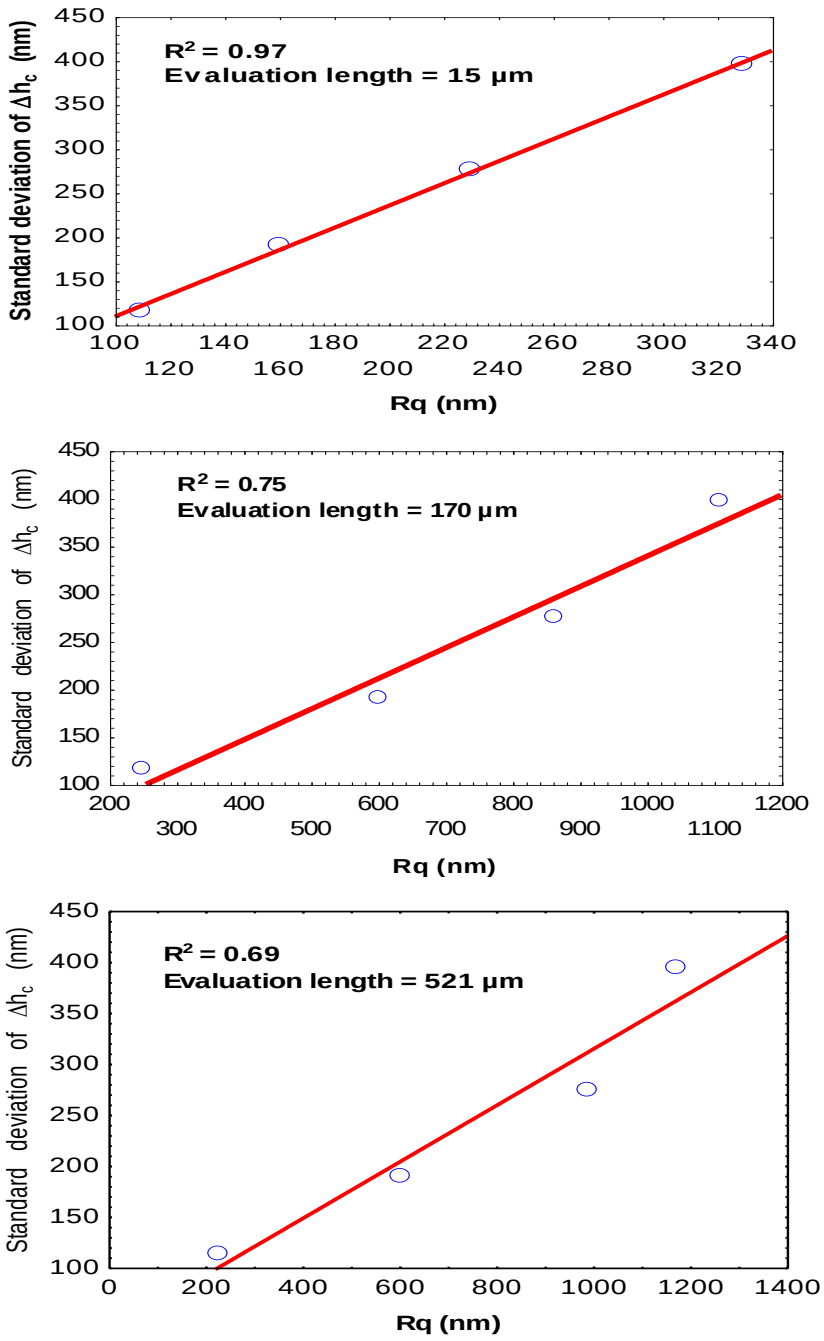

Figure 25: Linear relationship between the standard deviation of initial contact depth error and the surface roughness parameter Rq calculated with evaluation length equal to 15, 170 and 521 µm, separately.

In fact, this study was applied to various evaluation lengths in order to determine the suitable scale at which the best relationship is obtained. The linear coefficient of determination (R^2) as a function of the different evaluation lengths chosen to calculate the relevance Rq is plotted in Figure 26. The best parameter is identified for evaluation length approximately equal to 15 µm, with a linear correlation coefficient equal to 0.97.

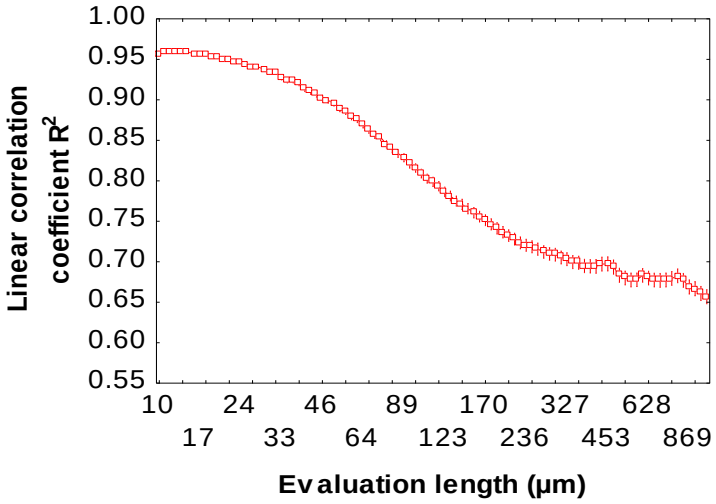

Figure 26: Evolution of the linear correlation coefficient (R^2) *versus* different evaluation lengths.

It means the best evaluation length of roughness identification in this instrumented indentation test is 15 µm, which is also in the size of the indentation print. The dispersion of the indentation curves is clearly correlated to the magnitude of the roughness, at the indentation imprint scale (15 µm). The proposed model allows predicting the mechanical properties based on instrumented indentation testing on sandblasted surface with the consideration of the effect of surface roughness.

III.3.2 Macro-hardness and ISE factor

In order to observe the effect of initial contact errors on the identification of the mechanical properties, the experimental data are treated in two different conditions: ignoring or considering the initial contact depth errors (Method F and Method A respectively). These two conditions correspond to $\Delta h_c = 0$ (not shifting curves) or $\Delta h_c \neq 0$ (shifting curves) in Equation (2.27).

Figure 27 shows the value of the macro-hardness H_0 for each sandblasted 2017A specimen calculated with (a) ignoring or (b) considering the initial contact depth error. The distribution of the macro-hardness for each specimen is displayed by a box-whisker diagram.

It requires order the data numerically from smallest to largest and find the lower quartile, median and upper quartile. The diagram is made up of a "box" and "whiskers". The small point inside the box shows the median. The top and bottom lines of the box are the upper and lower quartiles of the range of macro-hardness for each specimen. The "whiskers" are straight line extending from the ends of the box to the maximum and minimum values. The boxes are more compressed for the macro-hardness estimated considering the initial contact depth errors. It indicates 50 percent of the macro-hardness fall in a small range.

First of all, the macro-hardness for the four specimens calculated for condition (a) is in the range of 1.01-1.54 GPa with a standard deviation around 0.1 GPa. For the second condition (b), the macro-hardness is in the range of 1.63-1.93 GPa with a smaller standard deviation around 0.02 GPa. It is also smaller than the value given by the MTS system of instrumented indentation (around 2 ± 0.3 GPa), which is calculated with an average of the results from each curve.

Second, the mean value of macro-hardness for condition (b) decreases with decreasing surface roughness (*i.e.* from S1 to S4, Figure 24). A possible explanation for this trend is the existence of a strain hardening layer induced by the sandblasting process. In the sandblasting process, a shorter distance between the jet and the surface for S1 or a stronger jet pressure for S2 means a higher surface work-hardening impact.

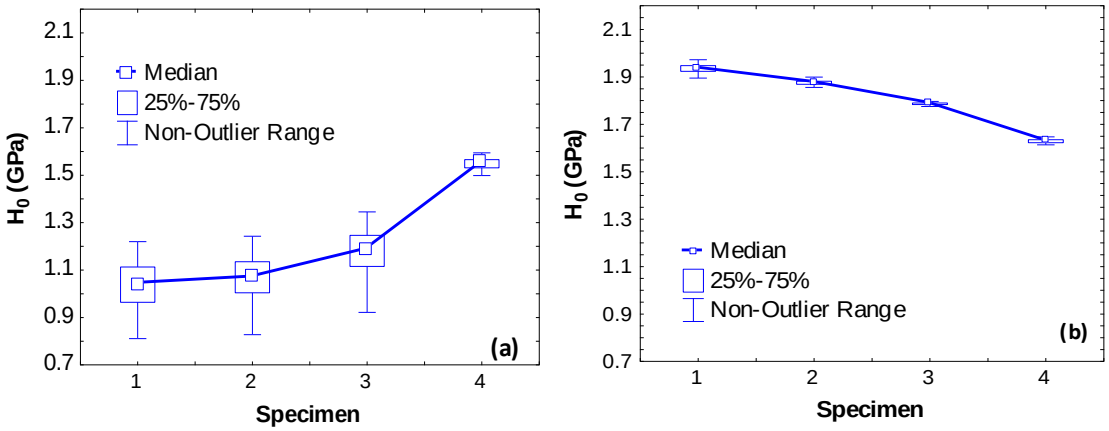

Figure 27: Macro-hardness for each sandblasted 2017A specimen calculated using the proposed method (a) ignoring or (b) considering the initial contact depth error.

The difference of the sandblasting parameters for S3 and S4 is the angle between the jet and the surface. For the smaller angle of S4, the sand particles shoot from a non-vertical direction. This procedure can be divided into two steps: abrading of the initial surface and rebounding from the sandblasted surface [45]. The latter process must dissipate a part of

energy done by the sand particles impact. Thus, the work to abrading the initial surface for S4 that the sand particles shooting to the surface with a angle must be weaker than the situation for S1 that sand particles shooting in a vertical direction. Therefore, the strain hardening layer in S4 is thinner than S3, which denotes a lower macro-hardness in instrumented indentation testing.

Furthermore, it is notable that the mean value of macro-hardness given by condition (b) is around 1.5 times the value given by condition (a) for the specimens S1, S2 and S3. However no difference is observed for specimen S4. The difference of the macro-hardness between the two conditions decreases with the decreasing of the surface roughness (surface roughness decreases from S1 to S4), which directly relies on the standard deviation of the initial contact depth error (Figure 21).

Figure 28 shows the ISE factor of each sandblasted 2017A specimen calculated with (a) ignoring or (b) considering the initial contact error. In condition (a), the ISE factor presents for all the specimens. But when considering the initial contact depth error as condition (b), the ISE factor becomes close to zero for specimens S1, S2 and S3 and the ISE factor remains the same for the specimen S4 (around 400 mN/nm). It suggests that if the initial contact depth error is not considered in the analysis process, an artificial ISE will occur for rougher surface (S1, S2 and S3). This “artificial” ISE on rougher surface can be reduced by considering the initial contact depth error. Due to the correlation between the surface roughness and the initial contact depth error, we could say that the ISE for the rougher surface is mainly resulted from the serious roughness. Compared with the surface roughness, the other reasons such as the effect of pile-up on ISE become negligible. For the fine surface S4 with the lowest roughness, the ISE is not reduced by the consideration of initial contact depth error. A possible reason is that, for the fine surface, the effect of the pile-up on ISE is greater than the effect from the surface roughness. The pile-up around the indentation imprint is probably the best explanation for the ISE occurrence for specimen S4 (inset figures in Figure 28) [46,47]. Therefore, the ISE of S4 which is resulted from the effect of pile-up will not be diminished by considering the initial contact depth error because the initial contact depth error is just related with the surface roughness.

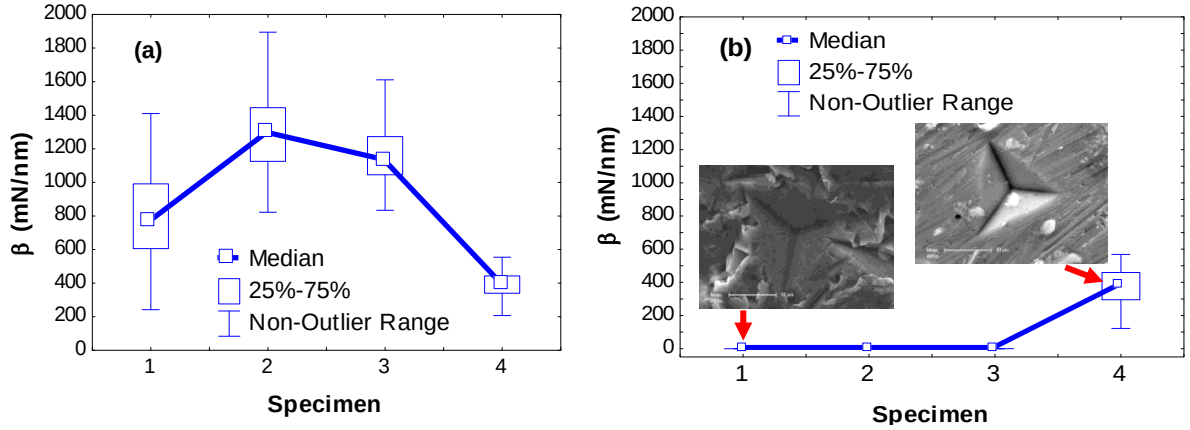

Figure 28: Indentation size effect factor β for each sandblasted 2017A specimen (a) ignoring (Method F) or (b) considering (Method A) the initial contact depth error. The inset figures show an indentation print of specimen S1 (left) and of specimen S4 (right) observed with Scanning Electron Microscopy.

III.3.3 Loading-depth curve simulation

To further explain the difference of the estimated mechanical properties with the two conditions, a set of loading-depth curves are simulated for each specimen basing on the actual experimental loading-depth curves using the following method: the simulated curves are generated according to Equation (2.24):

$$P = \alpha(H_0 h_c^2 + \beta h_c) \tag{2.24}$$

where the macro-hardness H_0 and the ISE factor β are equal to the mean value identified by the proposed model with the consideration of initial contact depth error (condition b). The placement of simulated curves is only defined by an imposed standard deviation of the initial contact depth error (σ_Δ). Each simulated curve is shifted along x-axis according to a Gaussian distribution with different imposed standard deviations. The number of simulated curves is equal to the number of experimental curves for each specimen. Therefore, one hundred curves are generated for each specimen with different standard deviations σ_Δ (from 0 to 500 nm) of the distance between the simulated curves and the zero point. The average of the distances between the simulated curves and the zero point is supposed to equal zero, *i.e.* the systemic zero of all the numerical curves is supposed at the zero of x-axis. This distance just corresponds to the initial contact depth error of the experimental curves. It is worth to highlight that the average of the initial contact depth errors for experimental loading-depth curves are statistically zero due to the Gaussian distribution. Even they are a little different with real zero (as shown in Figure 21), these averages could be turn back to

zero with infinite curves. Comparing with the experimental results controlled by all the parameters, the simulated results are just controlled by the imposed standard deviation. The simulated loading-depth curves are treated with the proposed method with and the simulated macro-hardness are calculated.

Figure 29 shows the variation of the simulated macro-hardness for the four specimens, as a function of the imposed standard deviation of the distance between the simulated curves and the zero. It is found that the situation of imposed standard deviation σ_{Δ} = 0 corresponds to the fact that all the loading-depth curves are close enough (see insets figures for S4 in Figure 29). This is similar with the positions of experimental loading-depth curves in Figure 20(b) that the dispersion of curves has been minimized by the consideration of initial contact depth error (*i.e.* condition (b)). In other words, the imposed standard deviation σ_{Δ} = 0 is equivalent to the situation that the initial contact depth error has been considered in experimental loading-depth curves analyzing. On the contrary, when the imposed standard deviation σ_{Δ} is around to 400 nm, it is equivalent to the state that the experimental loading-depth curves are analyzed without any consideration of the initial contact depth error.

Moreover, for each specimen, the average of simulated macro-hardness decreases with the increasing of the imposed standard deviation and it arrives to the highest value when σ_{Δ} = 0. It means that the minimization of the dispersion of loading-depth curves with the proposed method considering the initial contact depth error will increase the calculated macro-hardness, which is consistent with the analyzing results observed for experimental loading-depth curves. (*i.e.* the macro-hardness calculated with condition (b) that considering the initial contact depth error is higher than the one obtained with condition (a), see Figure 27).

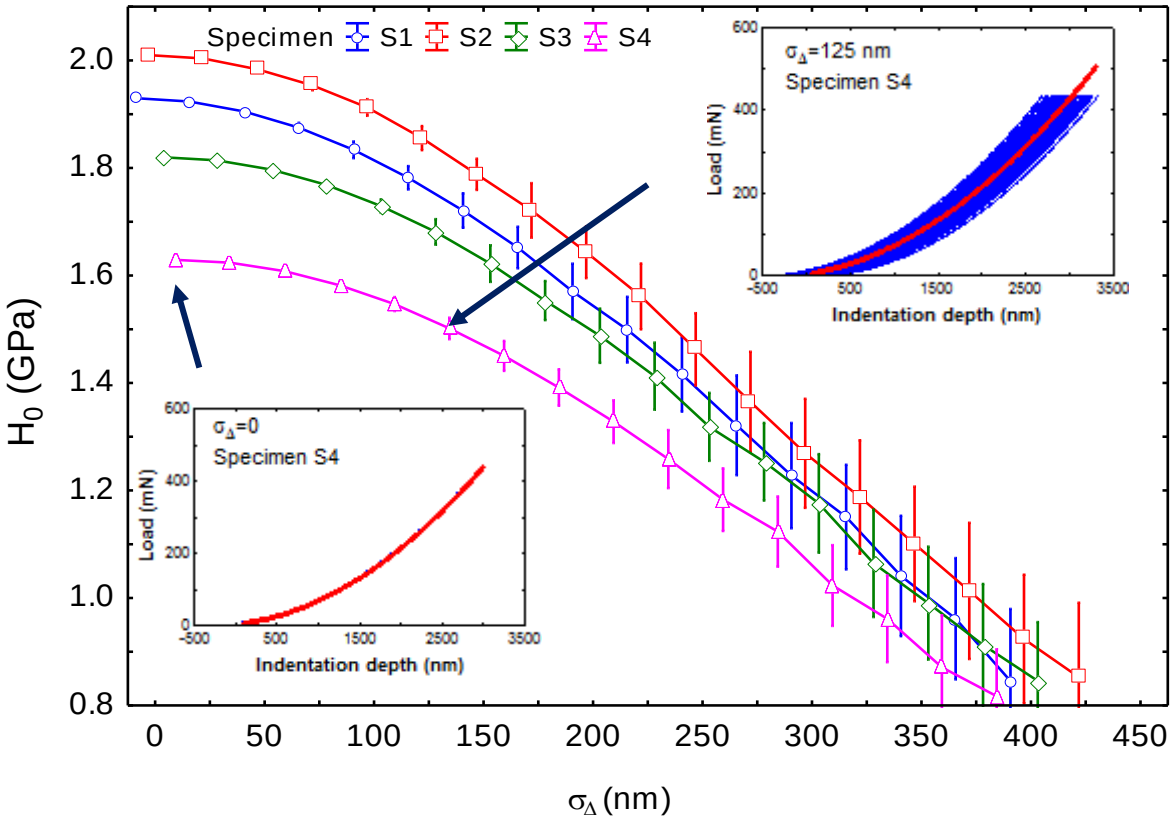

Figure 29: Variation of the macro-hardness of the simulated curves for the four specimens, as a function of the standard deviation of the distance between the zero and the actual position of the simulated curves. In the inset figures, the thin curves are the simulated loading curves obtained before the optimization while the bold ones obtained after optimization with the proposed model.

III.3.4 Conclusions

In this part, the proposed numerical method is applied to four sandblasted 2017A specimens having different surface roughness. A significant correlation between the distribution of initial contact depth error and the surface roughness is found. In order to quantify this correlation, a multi-scale analyzing method is firstly used to estimate the effect of evaluation length on the surface roughness parameters. And then a linear regression method is used to study the relationship between the distribution of initial contact depth error and the root-mean-square surface roughness parameter at different evaluation lengths. Finally, a linear relationship between the surface roughness parameter Rq and the initial contact depth error, similar to that obtained for the specimens 316L, is found when the evaluation length is equal to 15 µm. It proves that even the material and the surface

generation process are changed, the proposed numerical model is still suitable for analyzing the instrumented indentation data with the consideration of the effect of surface roughness.

Moreover, the mechanical properties for sandblasted 2017A specimens are studied with the proposed method but for two different conditions: considering or ignoring the initial contact depth error. It is found that the macro-hardness estimated with considering the initial contact depth error is higher than one obtained when the initial contact depth error is ignored. Thus, the loading-depth curves are simulated basing on the experimental loading-depth curves with different imposed standard deviations of the positions. By applying the numerical method on the simulated loading-depth curves, a similar situation is found for the simulated curves.

III.4 Assessment of elastic modulus with initial contact depth error

In this part, the proposed method is applied to eleven 2017A specimens who are polished with different grit papers (the paper numbers are 80, 120, 180, 220, 320, 500, 800, 1000, 1200, 2400, and 4000). A considerable minimization on the dispersion of the loading-depth curves is obtained after the analyzing process, which is similar with the previous studies as shown in Figure 20. The macro-hardness and indentation size effect factors are estimated in two conditions: considering or neglecting the initial contact depth errors. Moreover, another important mechanical property Young's Modulus is also calculated.

III.4.1 Macro-hardness and ISE factor

The macro-hardness and the ISE factor are estimated using the proposed method in two different conditions: considering or ignoring the initial contact depth errors. These two conditions respectively correspond to the $\Delta h_c = 0$ (not shifting curves) or $\Delta h_c \neq 0$ (shifting curves) in Equation (2.27). Figure 30 shows the macro-hardness estimated in these two conditions. A box-whisker diagram is used to present the figures which are similar with the Figure 27.

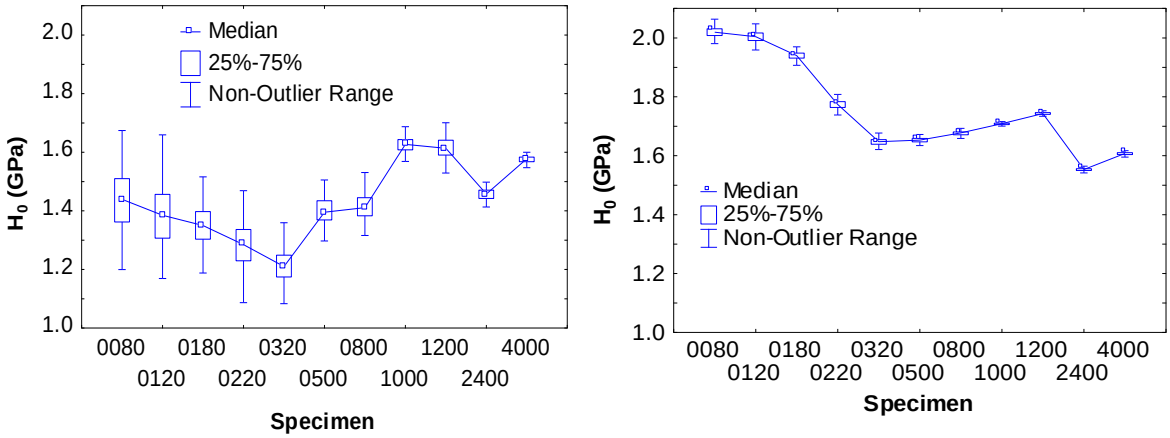

Figure 30: Macro-hardness for each polished 2017A specimen calculated using the proposed method ignoring (left) or considering (right) the initial contact depth error.

The variations of the macro-hardness estimated for the condition ignoring the initial contact depth errors are much lower than those estimated with the consideration of initial contact depth error. Moreover, the mean value of the macro-hardness estimated considering the initial contact depth errors varies with the different grit papers within the range of 1.55 – 2.05 GPa. From specimens polished with grit paper 80 to 320, the mean

value of H_0 decreases with the increase of the grit paper (*i.e.* the decrease of the size of the abrasive grain). This effect might be partly assigned to the influence of the contact surface in the indentation test. For the rougher surface (*i.e.*, polished by the lowest grit paper), the contact surface is small, hence the hardness is high. Within the second and the third group (*i.e.*, specimens polished with grit papers from 500 to 1200 and from 2400 to 4000, respectively), the mean value of H_0 increases with the increasing of the paper grit. This effect may be related to the work-hardening phenomenon arising from the polishing process.

Figure 31 shows the ISE factors estimated in these two conditions. The variation of the ISE factor calculated in the case of ignoring the initial contact depth errors globally decreases with the grit paper from 80 to 4000. It means the ISE factor is correlated with the surface roughness of the specimens for the material 2017A. After considering the initial contact depth errors, the mean value of ISE factor becomes close to zero for specimens polished with grit paper from 80 to 1200. However, there is no change for specimens polished by grit paper 2400 and 4000, almost similar ISE factors were obtained. This situation is similar with the sandblasted 2017A specimens. For materials with higher surface roughness, the surface roughness seems to be the main origin of ISE factor when the surface is rough. The consideration of the initial contact depth errors will diminish this “artificial” ISE factor.

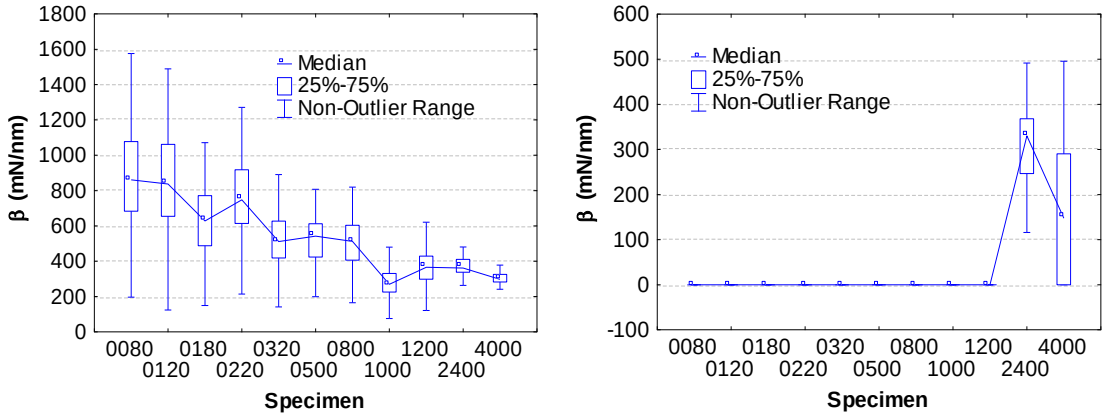

Figure 31: ISE factor for each polished 2017A specimen calculated using the proposed method ignoring (left) or considering (right) the initial contact depth error.

III.4.2 Contact stiffness and Young's Modulus

As described in Section II.2.5.2, the Young's Modulus can be determined indirectly by the calculation of the reduced elastic modulus with the contact stiffness and the projected contact area as in Equation (2.3).

$$E_r = \frac{\sqrt{\pi}}{2}\frac{S}{\sqrt{A}}, \tag{2.3}$$

According to Oliver and Pharr method, the projected contact area A can be calculated with the indentation contact depth h_c as shown in Equation (2.16).

$$A = f(h_c) = \alpha h_c^2, \tag{2.16}$$

Thus, a relationship between the contact stiffness and the contact depth with a pyramid indenter can be obtained from Equation (2.3) and Equation (2.16):

$$S = \frac{2\sqrt{\alpha}h_c}{\sqrt{\pi}}E_r, \tag{3.8}$$

Equation (3.8) indicates that the contact stiffness is linearly proportional to the indentation depth. The contact stiffness S evolution with the indentation depth considering the initial contact depth errors ($h_c + \Delta h_c$) is shown in Figure 32 for the 11 polished 2017A specimens.

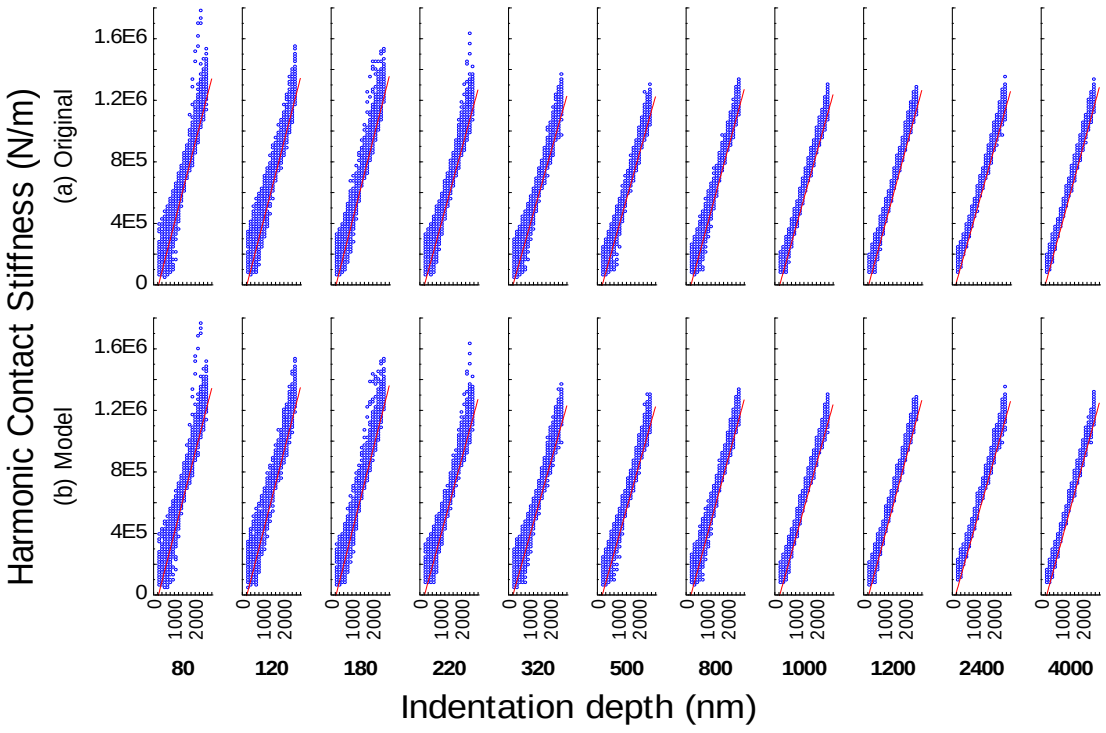

Figure 32: Evolution of the contact stiffness and the indentation depth (a) ignoring or (b) considering the initial contact depth error for each polished 2017A specimen.

For comparison, the relationship between contact stiffness S and the indentation depth ignoring the initial contact depth errors (h_c) is also indicated. Linear relationships are clearly observed for the different grit papers. Using a least square method, the corresponding slopes of contact stiffness on indentation depth considering the initial contact depth errors are estimated. As indicated in Figure 33, the mean values of the slopes for different specimens are nearly equal and in the range of 470-520 N/m. Hence, the contact stiffness seems to be not affected by the surface roughness or the surface hardening due to mechanical polishing.

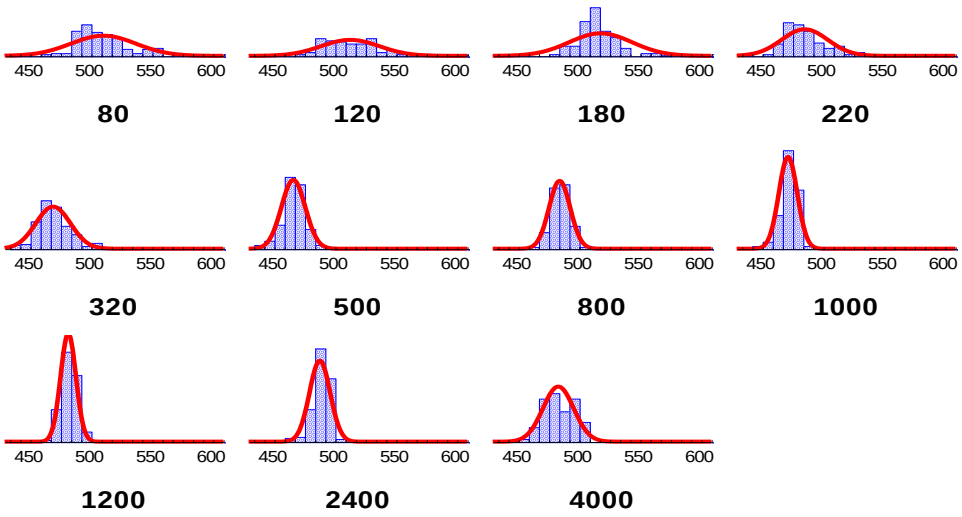

Figure 33: Slope of the contact stiffness on the indentation depth considering the initial contact depth error.

The Young's modulus of the different samples is computed using Equation (2.2) and Equation (2.3),

$$\frac{1}{E_r}=\frac{1-\nu^2}{E}+\frac{1-\nu_i^2}{E_i}, \tag{2.2}$$

$$E_r=\frac{\sqrt{\pi}}{2}\frac{S}{\sqrt{A}}, \tag{2.3}$$

The finally equation is as follow:

$$E=\frac{1-\nu^2}{\frac{1}{E_r}-\frac{1-\nu_i^2}{E_i}}=\frac{1-\nu^2}{\frac{2\sqrt{\alpha}h_c}{S\sqrt{\pi}}-\frac{1-\nu_i^2}{E_i}} \tag{3.9}$$

where ν =0.3 for material 2017A.

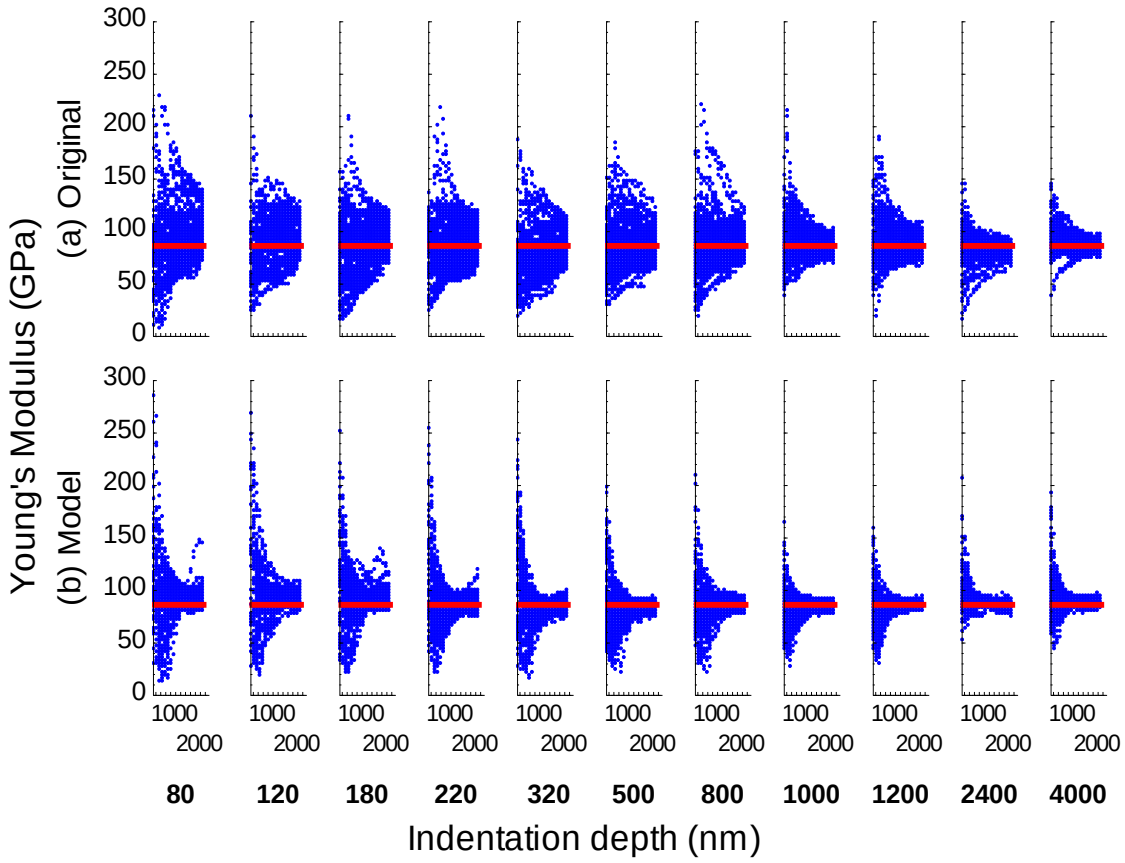

Figure 34: Young's Modulus calculated by the proposed method (a) ignoring or (b) considering the initial contact depth error for each polished 2017A specimen.

Figure 34 shows the evolution of the Young's modulus calculated with the proposed model (a) ignoring or (b) considering the initial contact depth error. When the model is applied with condition (b), the calculated Young's modulus is more gather than those in condition (a). The consideration of the initial contact depth error decreases the dispersion in the Young's modulus calculation. However, for small indentation depths (less than 100 nm), a poor evaluation of the Young's modulus is observed, which can be related to the first contact detection error. The latter is more critical for small depth values (see h_c in Equation (2.11)). Note that for higher indentation depth (>100nm), as expected, the calculated Young's modulus remains almost constant for the 11 tested samples. The estimated value in condition (b) is around 85 ± 16 GPa (see Figure 35), which is consistent with the theoretical value of the elastic modulus of the aluminum alloy 2017A (73 GPa) [48].

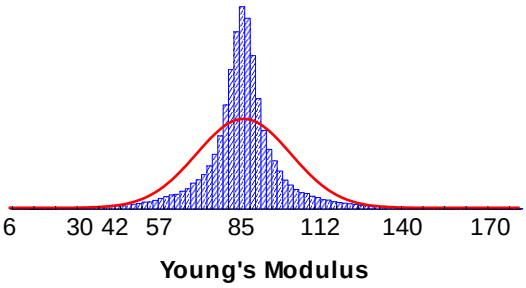

Figure 35: Distribution of the Young's Modulus of polished 2017A specimens.

III.4.3 Relationship between surface roughness and initial contact depth error

Figure 36 shows the distribution of the initial contact depth error calculated with the proposed numerical method for each specimen. A decrease in the scatter is observed with a finer polishing. This scatter is characterized by the standard deviations varying from 68 to 280 nm for the specimens polished with grit paper 4000 and 80, respectively. There is no doubt that these standard deviations of the initial contact depth error significantly relate to the effect of the surface roughness on the instrumented indentation curves.

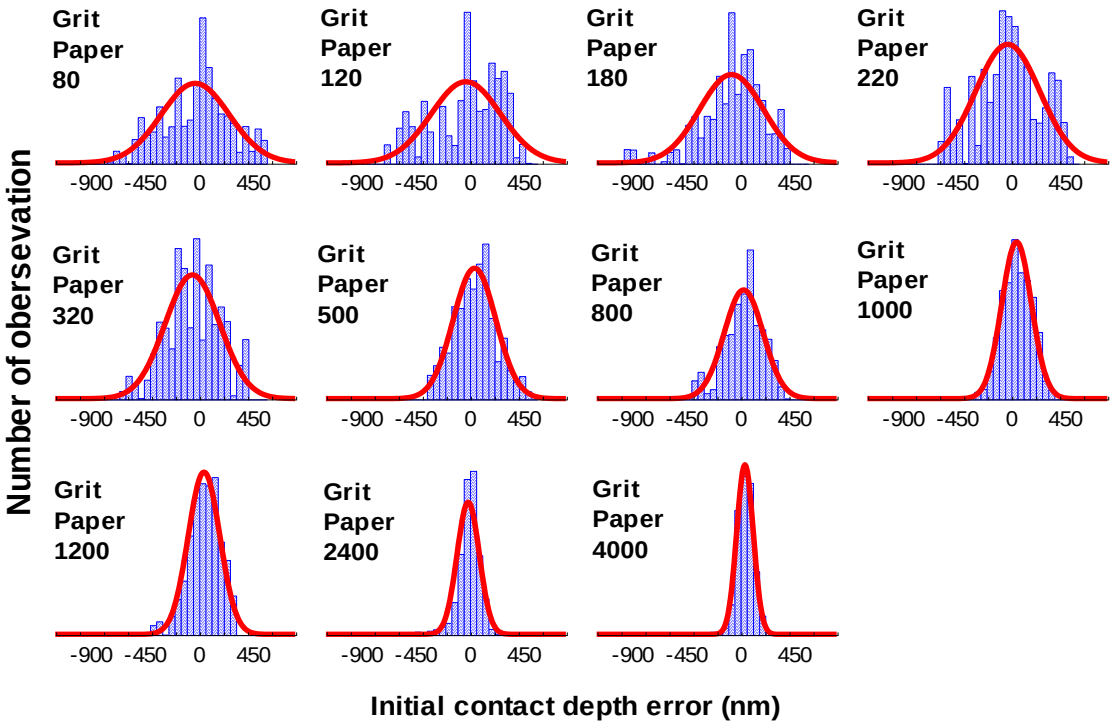

Figure 36: Distribution of the initial contact depth error for each polished specimen 2017A and the standard deviation of the initial contact depth error.

As the initial contact depth error is significantly different in each polished specimen, the influence of the roughness on the nanoindentation tests is performed. As described in Section II.2.4, such a study is difficult to handle with because it implies the use of roughness parameters whose values are intimately linked with the evaluation length chosen for their calculation. The arbitrary choice for the evaluation length introduces a bias in the estimation of the roughness parameters and thus may introduces errors in the analysis results. To deal with this issue, a multi-scale surface roughness analyses is developed as in paragraph III.3.1 for the sandblasted samples.

The surface profiles are recalculated with different evaluation lengths. Figure 37 plots the multi-scale profile reconstructions corresponding to two different evaluation lengths (15µm and 5µm) for 2017A specimens polished with grit paper 80, 180, 800 and 4000, respectively. As expected, the profile calculated with smaller evaluation length shows more slight details for each specimen.

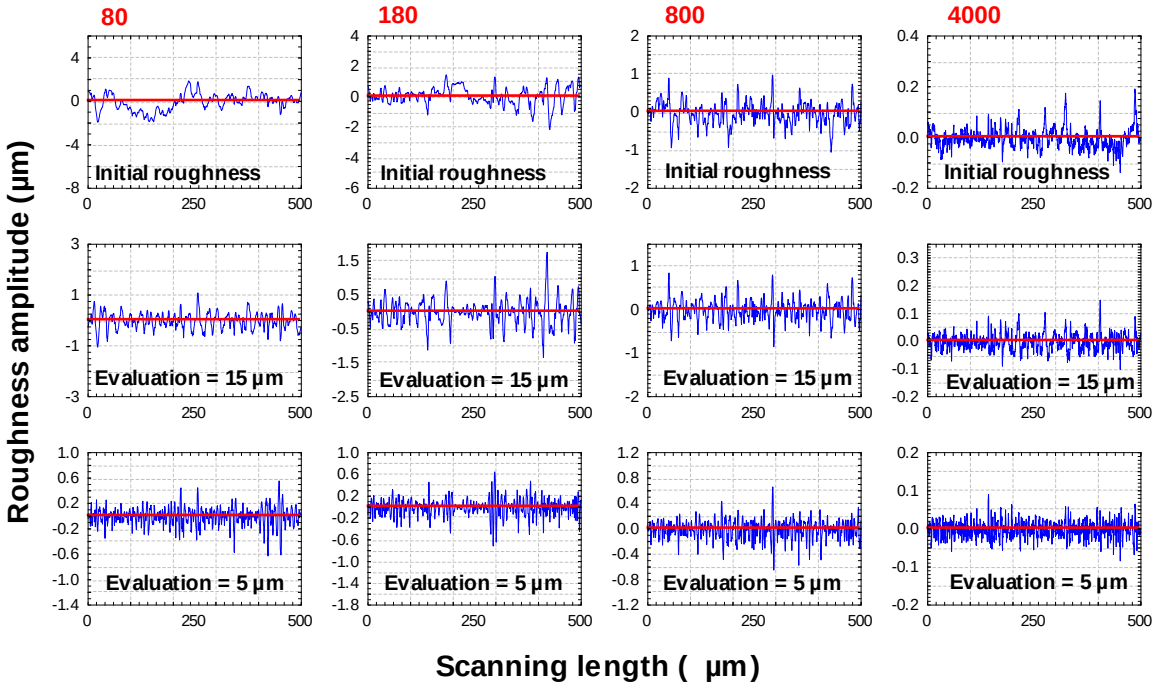

Figure 37: Multi-scale profile reconstructions corresponding to different evaluation lengths for 2017A specimens polished with grit papers 80, 180, 800 and 4000.

The root mean square roughness parameter R_q is calculated according to these different profiles analyzed with different evaluation lengths. Figure 38 shows the evolution of the roughness parameter R_q with different evaluation lengths for each polished 2017A specimen. The roughness parameter R_q increases with the evaluation length at small scale and reaches a saturation state after an evaluation length (around 15 µm) for grit papers 800

to 4000, and the stable value of Rq is within a range of 25 - 80 nm. For grit papers 80 to 500, the root mean square roughness parameter continues to increase and achieves a stable value when the evaluation length is around 170 µm. The corresponding stable value of Rq is within a range of 300 - 900 nm, which is much higher than the stable value of the fine surface. It is worth to note that for the sandblasted 2017A specimens, the stable value of Rq is also in the range of 300 - 900 nm and it is achieved when the evaluation length is around 170 µm (see Figure 24). It seems that, comparing with the smoother surface, a higher evaluation length threshold (around 170 µm) is required for the rougher surface in order to get a stable roughness parameter. The difference of this evaluation length threshold between the rougher surface (300 - 900 nm) and the smoother surface (25 - 80 nm) may be explained by the Gaussian distribution in the multi-scale surface roughness analysis method. As mentioned in Section III.3.1, the roughness parameter Rq is the standard deviation of the Gaussian distribution of the vertical surface heights. A stable roughness parameter Rq (*i.e.* stable standard deviation) will be achieved only when adequate variances of the vertical surface heights are included in the distribution. For the rougher surface, the variances of the vertical surface heights are more important than the smooth surface. It is therefore reasonable that a longer evaluation length is required to insure that adequate variances of the vertical surface heights are included in the distribution and to achieve a stable roughness parameter for rougher surface.

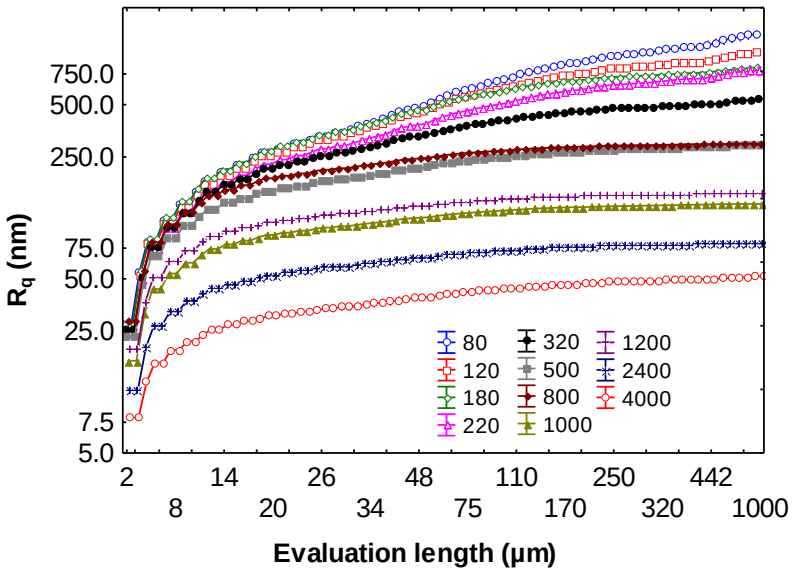

Figure 38: Evolution of the root mean square surface roughness parameter (Rq) *versus* the evaluation length for each polished 2017A specimen.

To assess the effect of the surface roughness on the instrumented indentation data, the standard deviation of the initial contact depth error is represented as a linear function of the roughness parameter Rq. This relationship has been calculated on eighty evaluation lengths between 5 and 1000 µm for determining the scale at which the best relationship is obtained. Finally, the best correlation between the root mean square roughness parameter Rq and the standard deviation of the initial contact depth error is obtained when the evaluation length is around 15 µm, as shown in Figure 39.

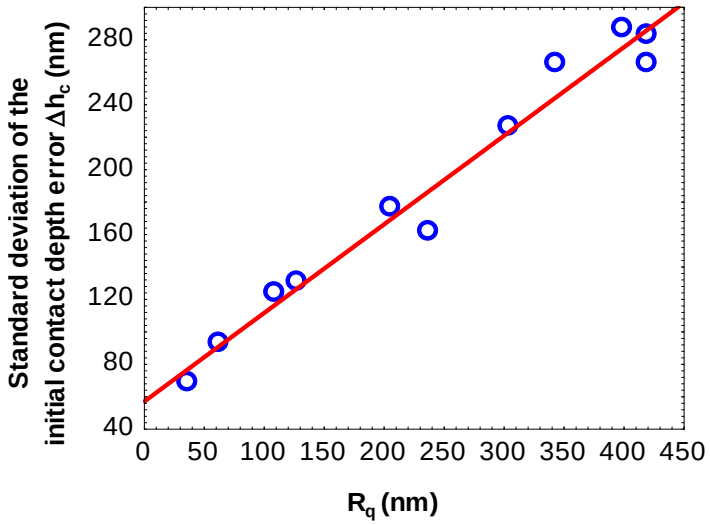

Figure 39: The linear correlation between the standard deviation of the initial contact depth error and the RMS roughness calculated with the evaluation length equals to 15 µm.

III.4.4 Conclusions

In this part, the proposed numerical method is applied to the polished 2017A specimens with different surface roughness. In addition to the macro-hardness of the material, the Young's Modulus is also estimated. Comparing the difference of mechanical properties calculated with considering or ignoring the initial contact depth error, the results prove that considering the initial contact depth error in the loading-depth curve treatment will effectively reduce the variation of the estimated material properties (*i.e.* Hardness and Young's modulus). Finally, as the previous studies on polished 316L and sandblasted 2017A specimens, a linear relationship between the standard deviation of the initial contact depth error and the surface roughness parameter is found when the evaluation length is around 15 µm.

III.5 Conclusions

In this chapter, the robustness of the proposed numerical model is examined by applying the proposed method on three different specimens. In the study of polished 316L specimen, the effect of the referential choice, simultaneous treatment and indentation size effect consideration on the calculation of hardness is assessed by comparing the material properties obtained from the proposed method and other classical methods. Subsequently, the effect surface roughness of sandblasted 2017A specimens on the instrumented indentation data is quantitatively estimated at different evaluation lengths by a multi-scale roughness analyzing and a linear regression method. The macro-hardness and ISE factor sandblasted 2017A specimens obtained from the proposed method with the condition of ignoring or considering the initial contact depth error are compared. Finally, in the study of polished 2017A specimens, the macro-hardness and Young's Modulus are calculated with the proposed numerical model. The results show that the identified material properties (*i.e.* Hardness and Young's modulus) will have a more large error if the initial contact depth error is neglected in indentation curves treatment, particularly when the specimens have a larger surface roughness.

As a conclusion, thanks to the application of the proposed method on the analyzing process of instrumented indentation data, significantly smaller standard deviations of material properties are obtained for all the materials. It shows that the proposed numerical method can perfectly improve the accuracy of the calculated hardness from the instrumented indentation testing even if the indentation is performed on rough surface. Moreover, the similar linear relationships between the standard deviation of the initial contact depth error and the surface roughness parameter are found for these three specimens. It clearly shows that the effect of surface roughness on the instrumented indentation data can be reduced by the consideration of the initial contact error with the proposed numerical model. Furthermore, these linear relationships of all the studied materials are obtained when the evaluation length for the estimation of surface roughness parameter is around 15 µm, which is just in the same scale with the indentation performed by Berkovich indenter.

Chapter IV Comparison of the indentation data obtained with different indenter tip

IV.1 Overview

In this chapter, the nanoindentation data performed on specimens TA6V4 with different surface roughness are analyzed using the proposed numerical method. The specimens are polished according the method described in Chapter II. For each specimen, 200 nanoindentation tests are performed. Half of them are performed with Berkovich indenter and the others are performed with Cube-Corner indenter. In order to verify the feasibility of the proposed method on different indenter tip and to check the effect of the indenter tip on the mechanical properties of material, the loading-depth curves obtained using these two indenters are analyzed by the proposed method and the corresponding mechanical properties are compared.

IV.2 Initial surface roughness

The initial surface roughness of the specimens is measured using 2D surface measurement equipment tactile profilometer TENCOR P10 and 3D surface measurement equipment optical interferometer. Figure 40 shows the different 3D topography of the surface of the samples polished by grit papers 80 and 800 as an example. Here, deep valleys (dark colors) and high peaks (light colors), due to the grinding process, are observed in the surface.

TA6V4 polished with grit paper 80	TA6V4 polished with grit paper 800
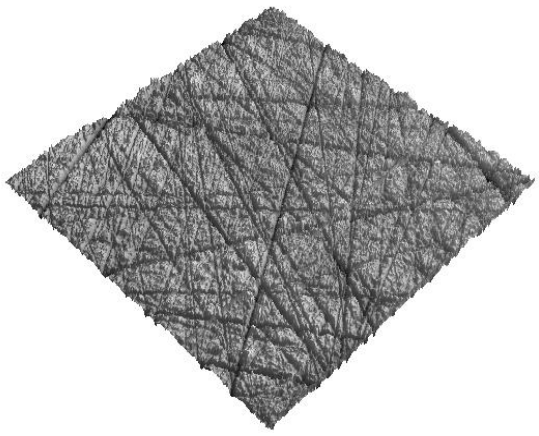	

Figure 40: 3D topography of initial surfaces of polished TA6V4 specimens with different roughness using optical interferometer.

The initial roughness profiles are experimentally measured for a given length. However, as described in the previous studies for specimens 316L and 2017A in Chapter III, this length is not suitable for studying the indentation imprint. A relevant evaluation length for the

roughness calculation should be selected. Figure 41 shows 2D roughness profiles which are calculated using 2 different evaluation lengths (20.2 µm and 5 µm) for samples 80, 180, 800 and 4000. The effect of the evaluation length on the estimation of the roughness parameters is clearly highlighted as already observed in the previous studies in Chapter III.

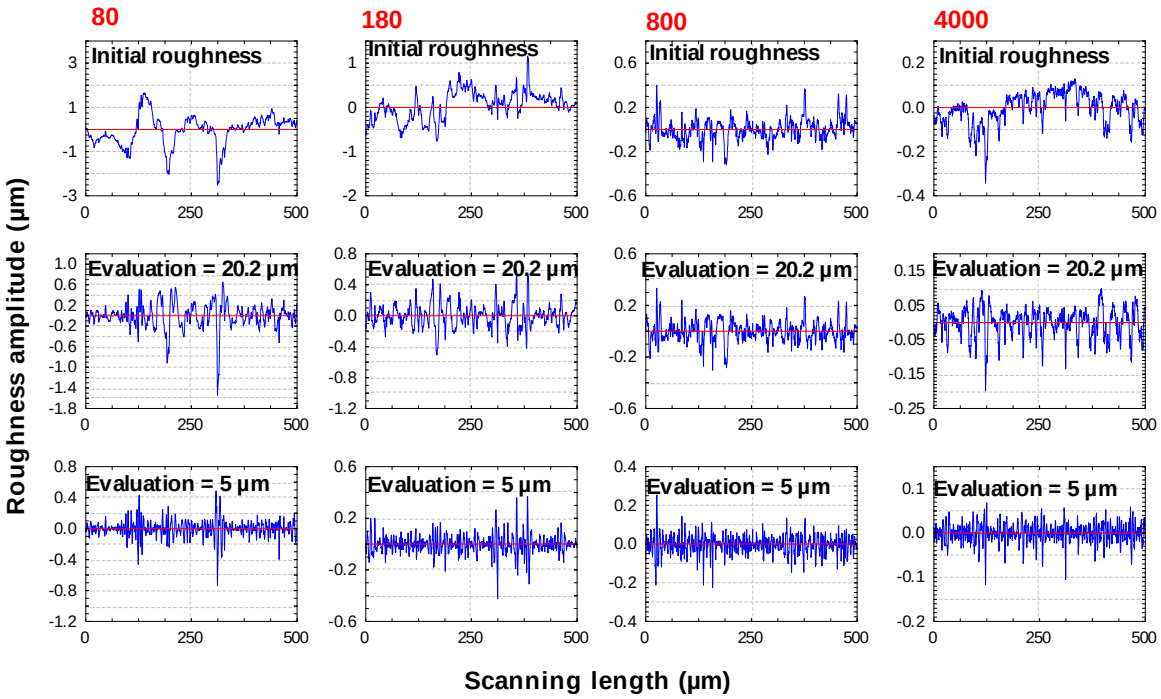

Figure 41: Multi-scale profile reconstructions corresponding to different evaluation lengths for TA6V4 specimens polished with grit papers 80, 180, 800 and 4000.

From these reconstructed profiles, the roughness parameter R_q is estimated. As shown in Figure 42, the root mean square parameter R_q increases logarithmically with the evaluation length for the different samples. However, for a given grit paper (*i.e.,* abrasive grain size) when a critical length is reached, the parameter R_q begins to increase slightly. Note that larger grit paper numbers (*i.e.*, lower abrasive grain size) correspond to lower R_q for all the evaluation length scales. The surface roughness of the specimens decreases from the grit paper 80 to grit paper 4000. Broadly, the critical evaluation length for the fine surface is around 20 µm (Rq is in the range of 20 - 200 nm, polished with grit paper from 180 to 4000), while the one for rougher surface is around 170 µm (Rq is in the range of 300 - 600 nm, polished with grit paper from 80 to 120).

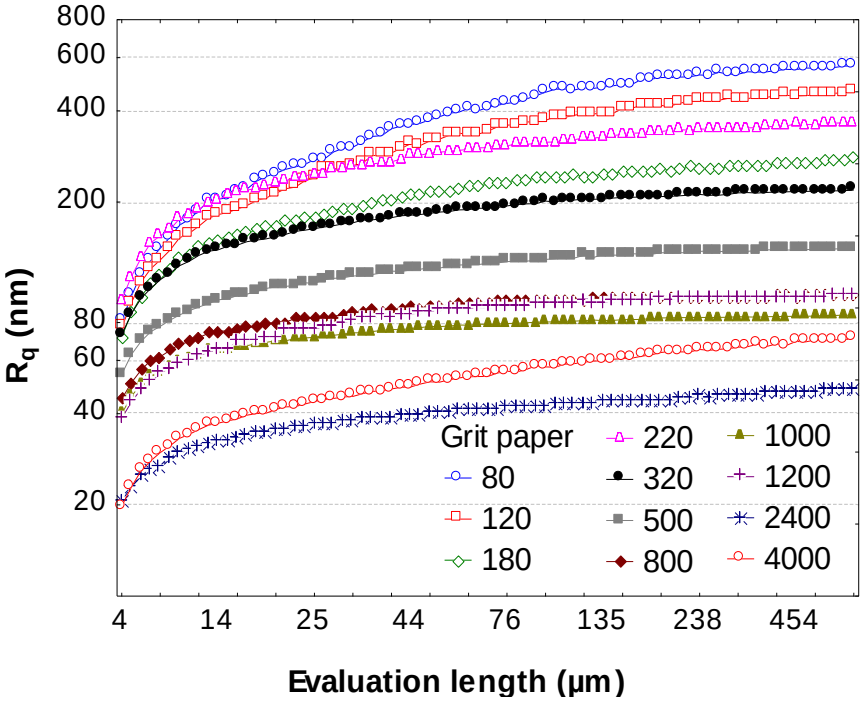

Figure 42: Evolution of the root mean square roughness parameter (Rq) *versus* the different evaluation lengths for each polished TA6V4 specimen.

IV.3 Loading-depth curve

The experimental loading-depth curves for the specimen polished with grit paper 80 or 2400, obtained with Berkovich or Cube-Corner indenter are shown in Figure 43. For both specimen 80 and 2400, the load is lower for the sharper indenters Cube-Corner than the one observed for the Berkovich at the same depth. For both indenter Berkovich and Cube-Corner, the loading-depth curves for specimen 80 present more scatter than the one for the specimen 2400. It is consistent with the previous study on other materials: rougher surfaces give higher scatter of the instrumented indentation curves. The different scatters obtained for the different specimens may be an evidence of the effect of the surface roughness on the instrumented indentation testing.

By application of the proposed method (Method A in Chapter III) to the instrumented indentation data performed with Berkovich or Cube-Corner indenters, the dispersion of the loading-depth curves are minimized with the consideration of the initial contact depth error. Figure 44 plots the loading-depth curves after the processing of the proposed method for the specimen polished with grit paper 80 or 2400, obtained with Berkovich or Cube-Corner indenter. As expected, very effective scatter reduction is obtained for the loading-depth curves, which is likely to yield more accurate macro-hardness estimation.

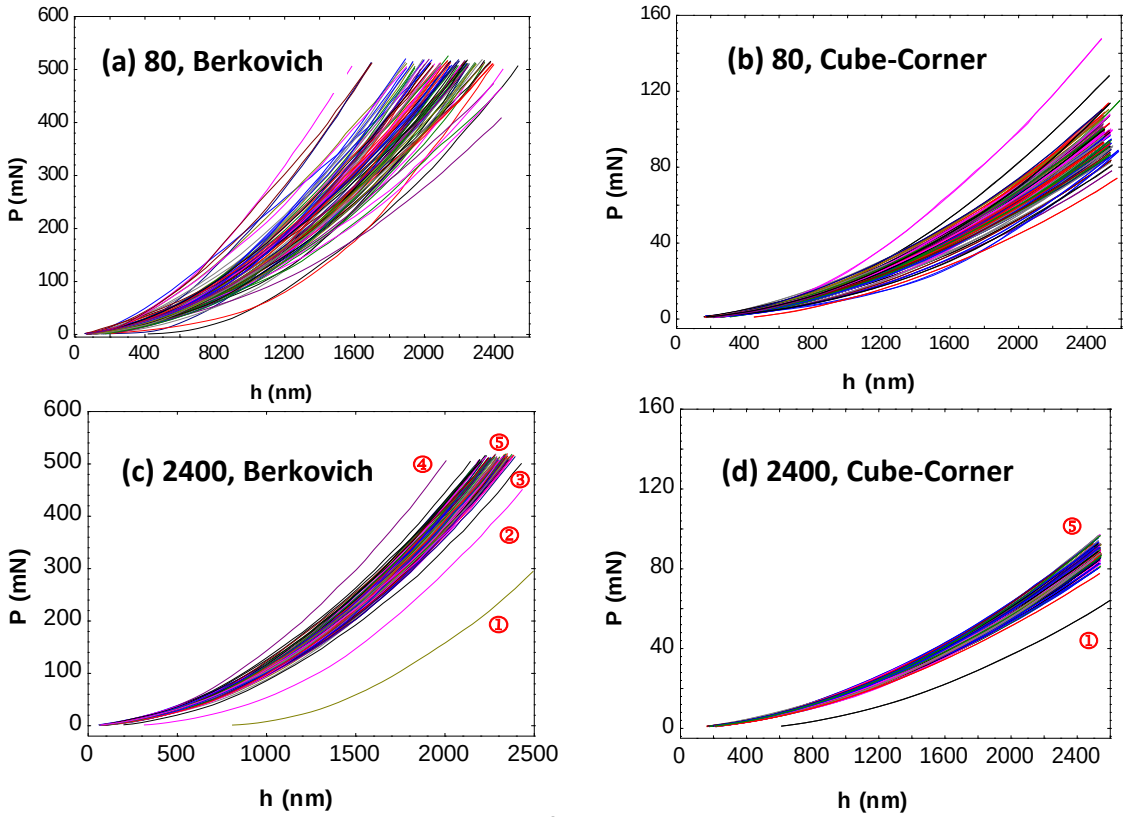

Figure 43: Experimental loading-depth curves for the TA6V4 specimen polished with grit paper 80 (up) or 2400 (down) obtained with (a), (c) Berkovich or (b), (d) Cube-Corner indenter.

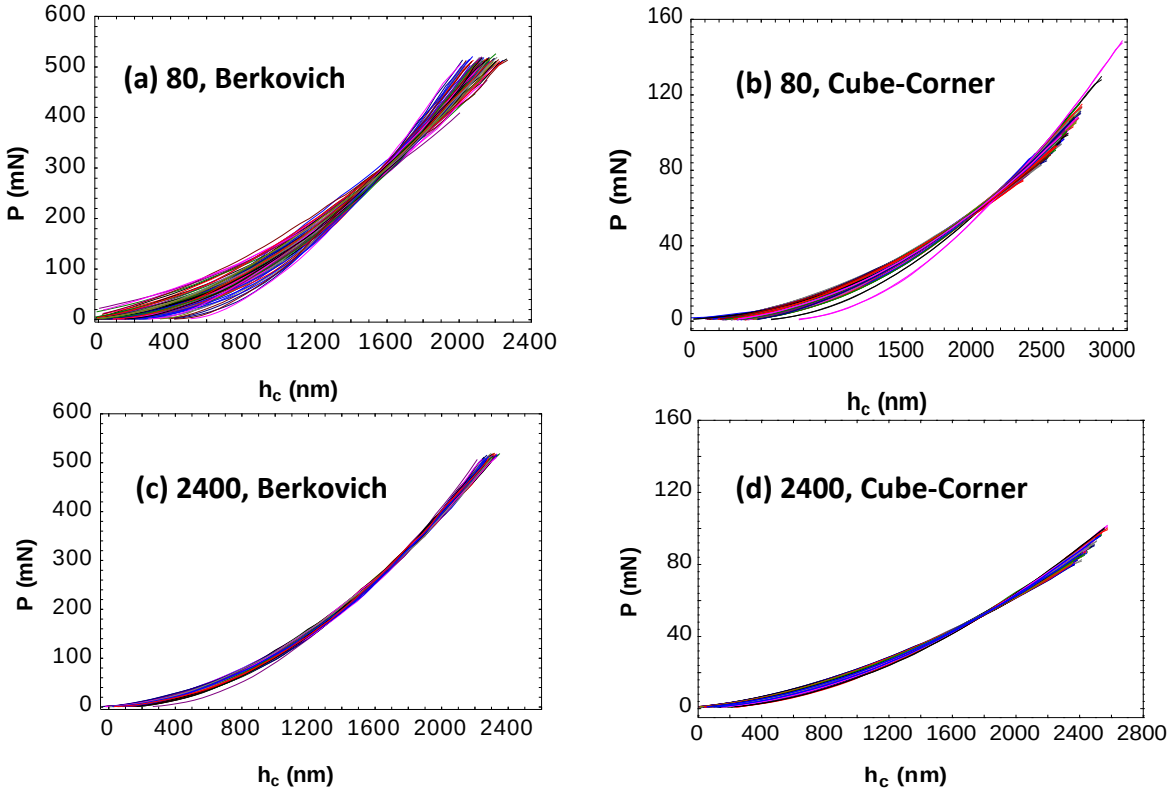

Figure 44 : Processing of the experimental loading-depth curves with proposed method considering the initial contact depth error for the TA6V4 specimen polished with grit paper 80 (up) or 2400 (down) obtained with (a), (c) Berkovich or (b), (d) Cube-Corner indenter.

IV.4 Macro-hardness and ISE factor

Figure 45 shows the distributions of the macro-hardness H_0 and the ISE factor β for the specimen polished with the grit paper 2400 obtained with Berkovich or Cube-Corner indenter. The mean value of the Berkovich macro-hardness and of the Berkovich ISE factor given by the proposed model is 3.64 GPa and 774 mN/nm, with the standard deviations of 0.008 GPa and 113 mN/nm, respectively. The mean value of the Cube-Corner macro-hardness and of the Cube-Corner ISE factor given by the proposed model is 4.39 GPa and 3420 mN/nm, with the standard deviations of 0.014 GPa and 86 mN/nm, respectively.

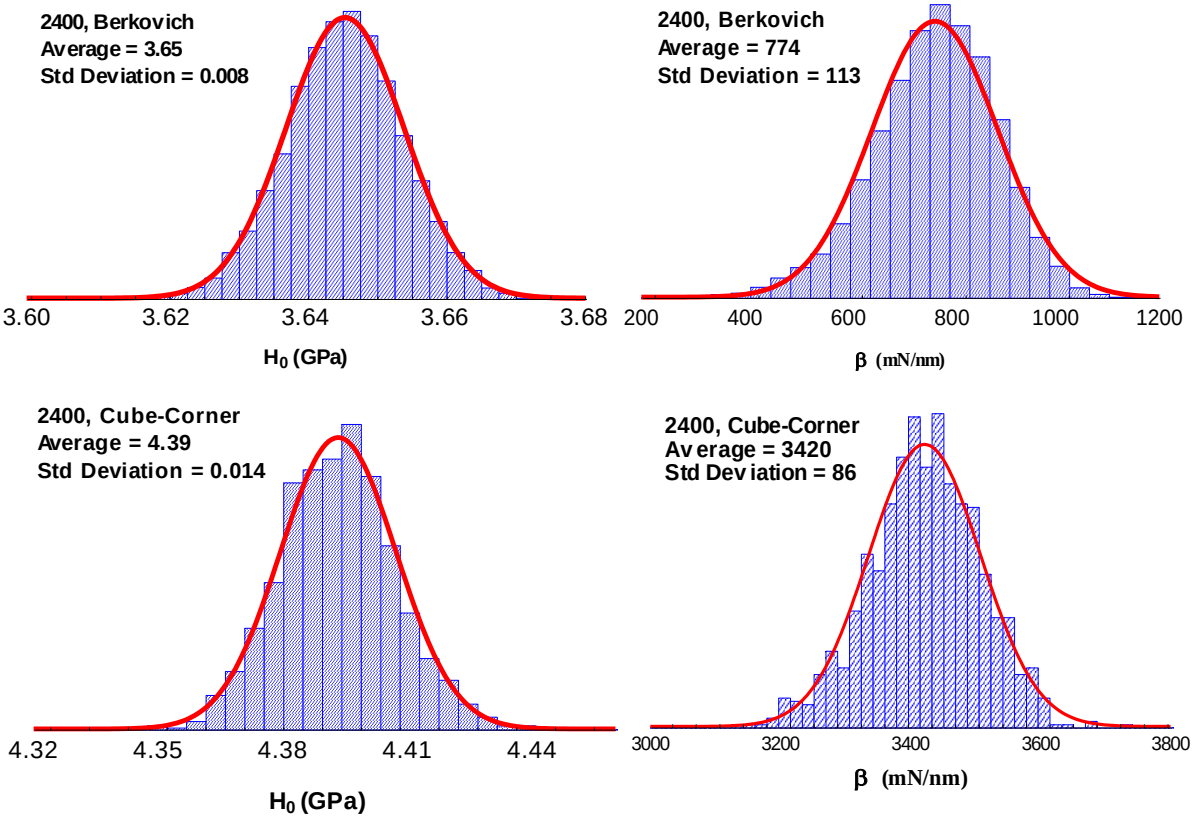

Figure 45: Distribution of the macro-hardness H_0 and the ISE factor β for the TA6V4 specimen polished with grit paper 2400 obtained with Berkovich or Cube-Corner indenter.

Moreover, the macro-hardness obtained with the Cube-Corner indenter is higher than the one obtained with the Berkovich by 20 percent. The situation is also similar for the specimens polished with other grit papers (See Figure 46). Hay and Pharr *et.al* [49, 50] affirms that during the indenter is pressed into the surface, the Cube-Corner indenter displaces more than three times the volume of the material compared to the Berkovich one,

thus producing higher stresses and strains in the contact area. It is a possible reason for explaining the difference of the macro-hardness obtained by different indenter.

Figure 46 shows the calculated macro-hardness H_0 and the ISE factor β obtained with Berkovich indenter and Cube-Corner for each TA6V4 specimen. The average macro-hardness varies with the different grit papers for both indenters. For the results obtained with Berkovich indenter, the macro-hardness varies in the range of 3.5-4.1 GPa. From sample 80 to 320, the average value of H_0 decreases with the increase of the grit paper (*i.e.*, the decrease of the size of the abrasive grain). This effect might be partly assigned to the influence of the surface contact area in the indentation test. For the rougher surface (*i.e.*, polished by the lowest grit paper), the surface contact area is small, hence the hardness is high. Within the second and the third group (*i.e.*, grit papers from 500 to 1200 and from 2400 to 4000, respectively), the average value of H_0 significantly increases the grit paper increases. This effect may be related to the work-hardening phenomenon arising from the polishing process. Similarly, the macro-hardness obtained with Cube-Corner indenter could also be separated into three groups (grit papers from 80 to 500, from 800 to 1200 and from 2400 to 4000), except for the specimen 220 whose value is abnormally high as it is equal to 5.12 GPa. This difference has not been explained yet. The standard deviations of all the specimens obtained with each indenter are relatively low, down to 0.01 GPa. Comparing with the macro-hardness given by the Nanoindentation MTS system, which calculates the macro-hardness using mean value of the hardness estimated from each curves (around 4.3 GPa with the standard deviation of 0.5 GPa), the macro-hardness calculated by our method shows a small deviation, no matter what kind of indenter is used. It indicates that a more reliable assessment of the material parameters can be provided by this quantitative method. The average values for the ISE factor β lie between 310 mN/nm and 1600 mN/nm for the results obtained with the Berkovich indenter, while the range of the results obtained with the Cube-Corner is from 1500 mN/nm to 3500 mN/nm, excepting for the specimen 220. Their deviation decreases when the grit paper increases. As the ISE is closely related to the materials and surface factors, it appears quite logical that the indentation size effect is not constant for each specimen. However, the ISE factor β is always greater than zero for each specimen. This clearly means that the ISE takes place in this titanium alloy.

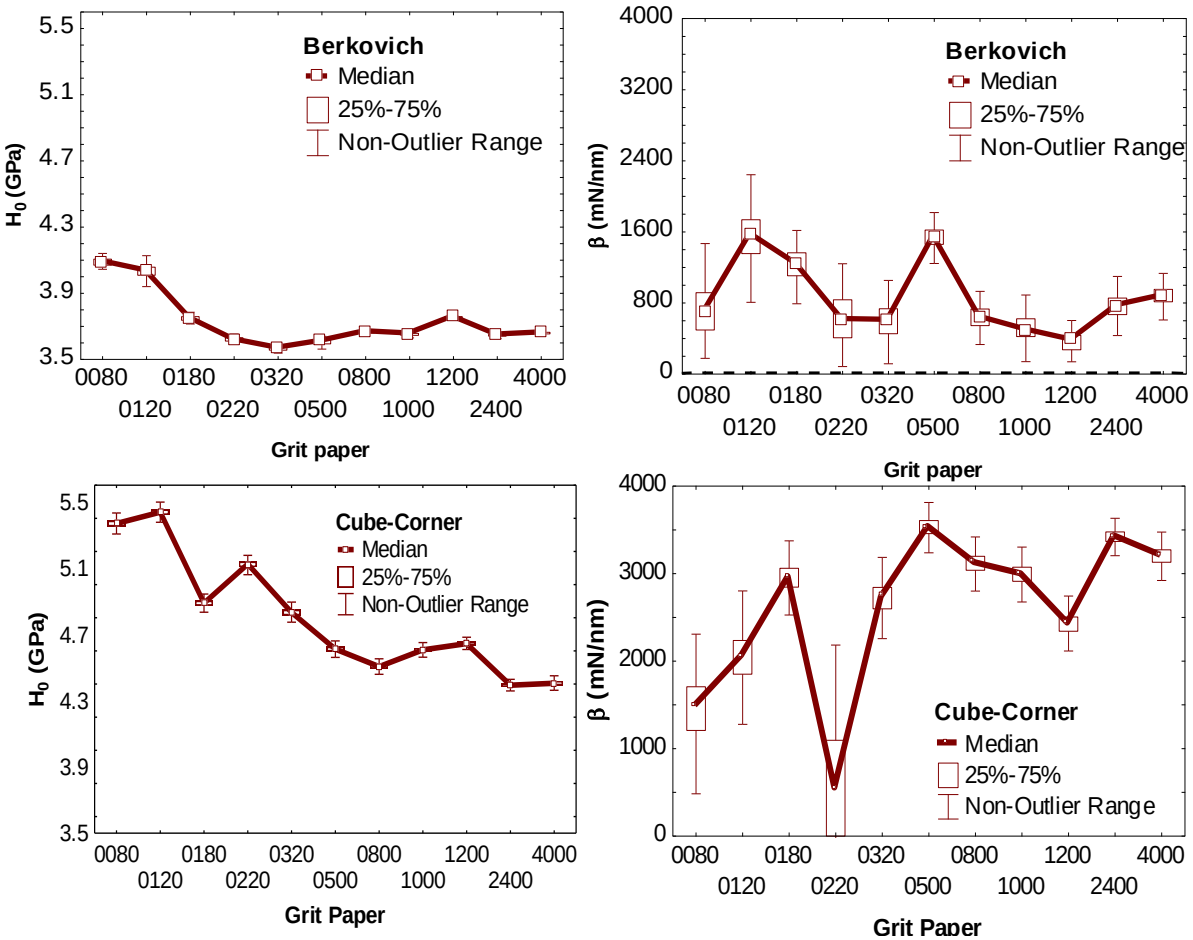

Figure 46: Macro-hardness H_0 and the ISE factor β for each TA6V4 specimen obtained with Berkovich and Cube-Corner indenters calculated using the proposed method (Method A).

The literature on the instrumented indentation test points out that the reasons behind the ISE are multiple, including the pile-up effect [51]. Due to the occurrence of the pile-up, the actual contact depth between the indenter and the specimen is higher than the recorded contact depth. It yields to an underestimation of the actual contact area, hence an overestimation of the hardness. As an example shown in Figure 47, the topography of the indentation imprint with pile-up for specimens polished with grit paper 2400 and 80 obtained with Berkovich indenter is observed with a Scanning Electron Microscope (SEM).

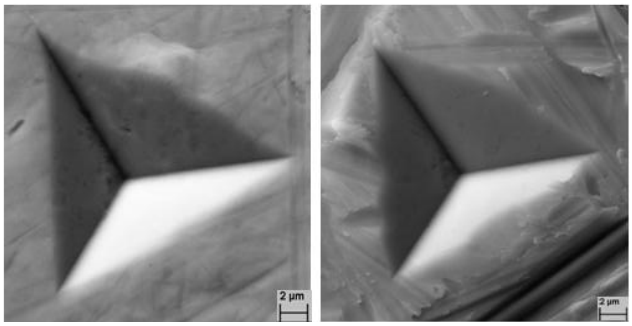

Figure 47: Observation of the indentation imprints obtained with Berkovich indenter for specimens TA6V4 polished by grit paper 2400 (left) and 80 (right) using Scanning Electron Microscopy.

IV.5 Contact stiffness and Young's Modulus

With the method described in Chapter III Section 4.2, the contact stiffness evolution with the indentation depth ignoring or considering the initial contact depth error obtained with Berkovich and Cube-Corner indenters are shown in Figure 48 for each TA6V4 specimen. Linear relationships are clearly observed for the different grit papers and different indenters.

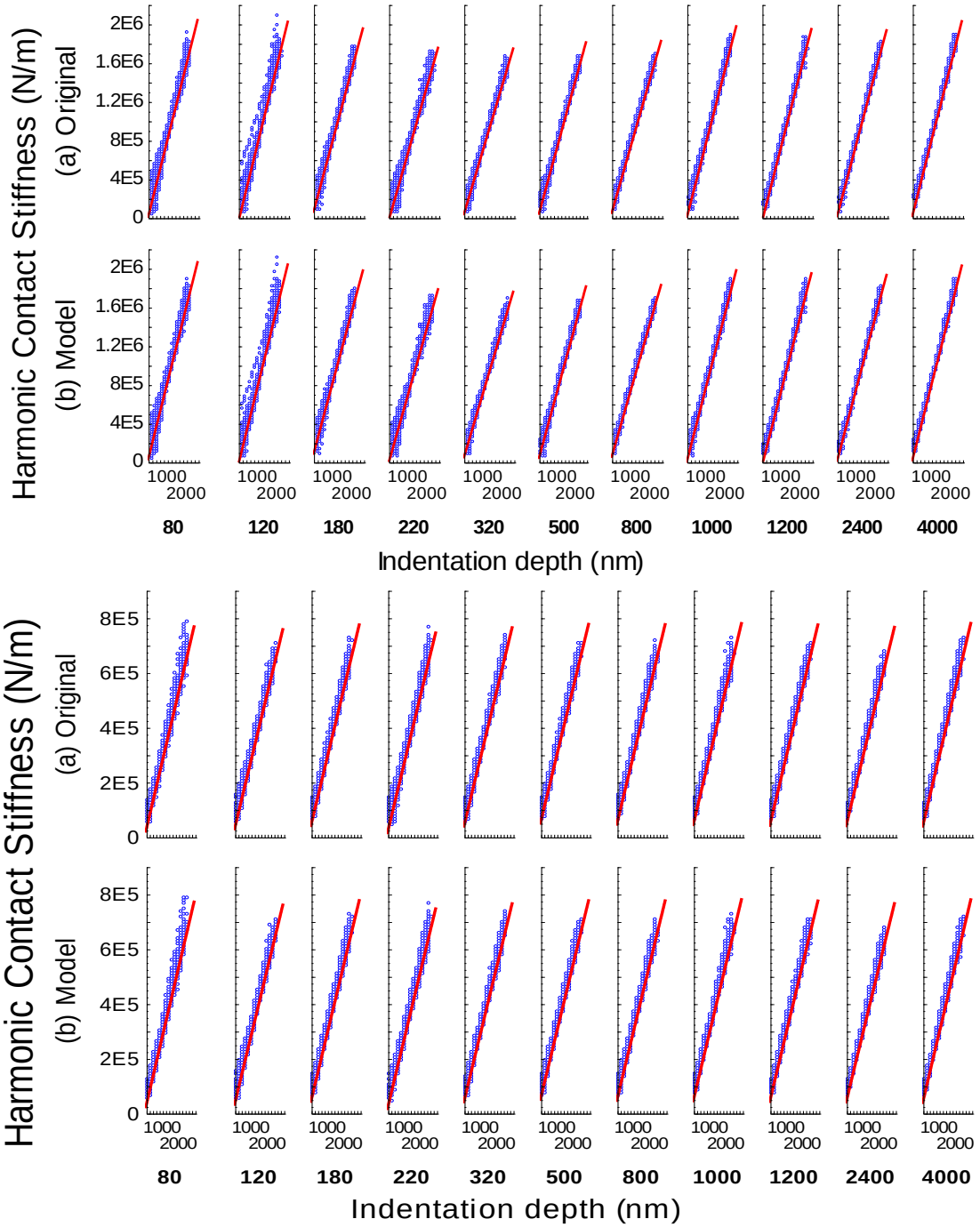

Figure 48: Evolution of the contact stiffness *versus* the indentation depth in the x axis (a) ignoring or (b) considering the initial contact depth error obtained with Berkovich (up) and Cube-Corner (down) indenters for each TA6V4 specimen.

The corresponding slopes of contact stiffness on indentation depth considering the initial contact depth error obtained with Berkovich and Cube-Corner indenter are estimated using a least square method.

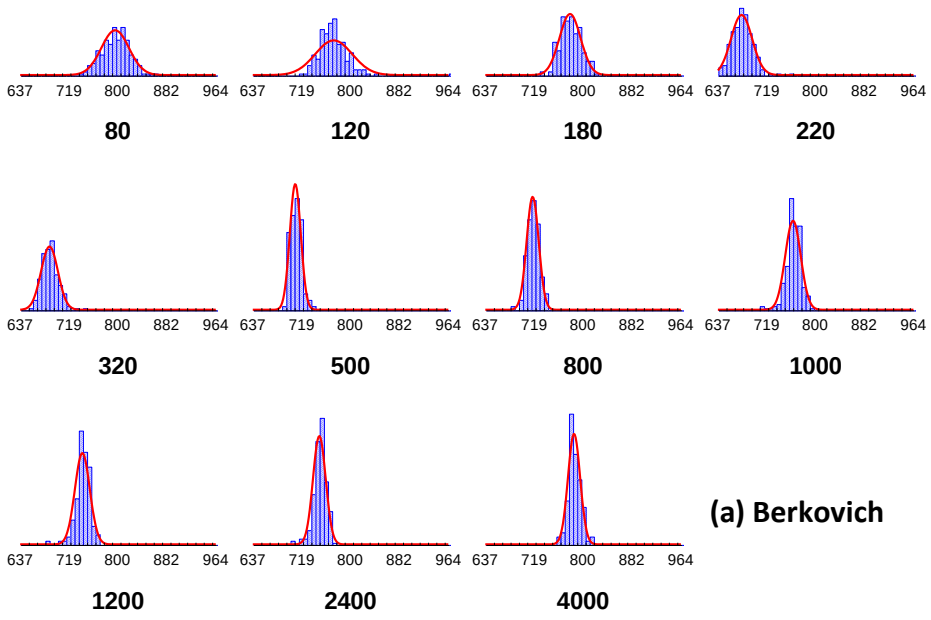

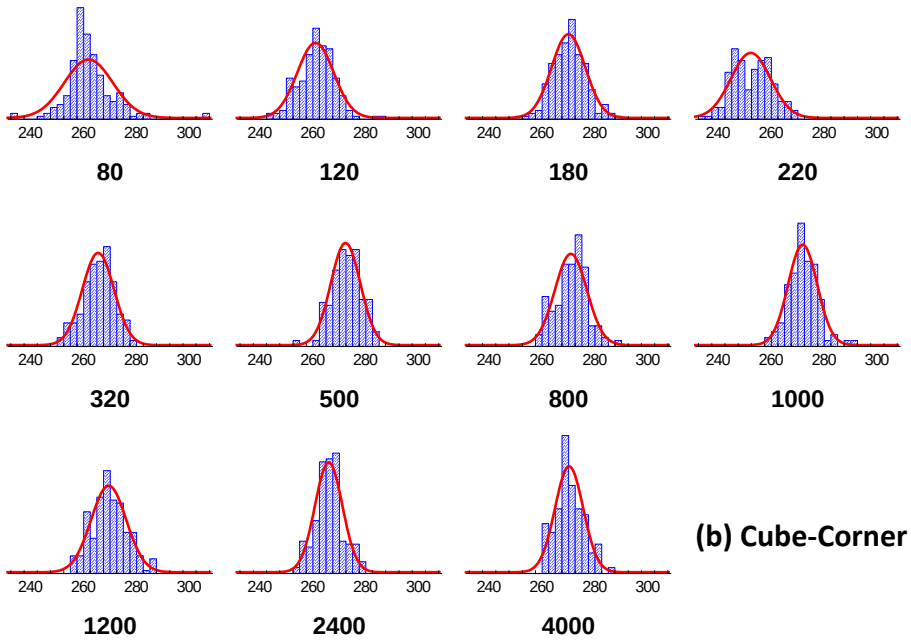

Figure 49: Slope of the contact stiffness on indentation depth considering the initial contact depth error obtained with (a) Berkovich and (b) Cube-Corner indenters for each TA6V4 specimen.

As indicated in Figure 49, the mean values of the slopes for different specimens but obtained with the same indenter are nearly equal. Hence, the contact stiffness seems to be independent from the surface roughness. For the Berkovich indenter, the slope values vary in the range of 676-795 kN/mm², which is three times higher than the range for the Cube-Corner (252-272 kN/mm²). Higher contact stiffness is obtained for Berkovich indenter for a given depth. It is consistent with the observations in Figure 48 that the contact stiffness for Berkovich indenter increases with the indentation depth more rapidly than the Cube-Corner.

The Young's modulus obtained with Berkovich or Cube-Corner indenters are calculated with the proposed method in Section III.4.2, as shown in Figure 50. The estimated value is around 136 ± 20 GPa for Berkovich indenter, which is a similar with the value calculated for Cube-Corner (150 ± 25 GPa). For both indenters, the values are consistent with data from the literature for this material (120 GPa) [52]. Figure 51 represents the evolution of the Young's modulus calculated with the proposed model (a) ignoring or (b) considering the initial contact depth error obtained with Berkovich and Cube-Corner indenters for each TA6V4 specimen. When the initial contact depth is considered in the model, the identified Young's modulus is more gather than those obtained in the case of ignoring the initial contact depth. The consideration of the initial contact depth error decreases the dispersion in the Young's modulus calculation. Note that for higher indentation depth (>100 nm), as expected, the calculated Young's modulus remains almost constant for each tested specimens.

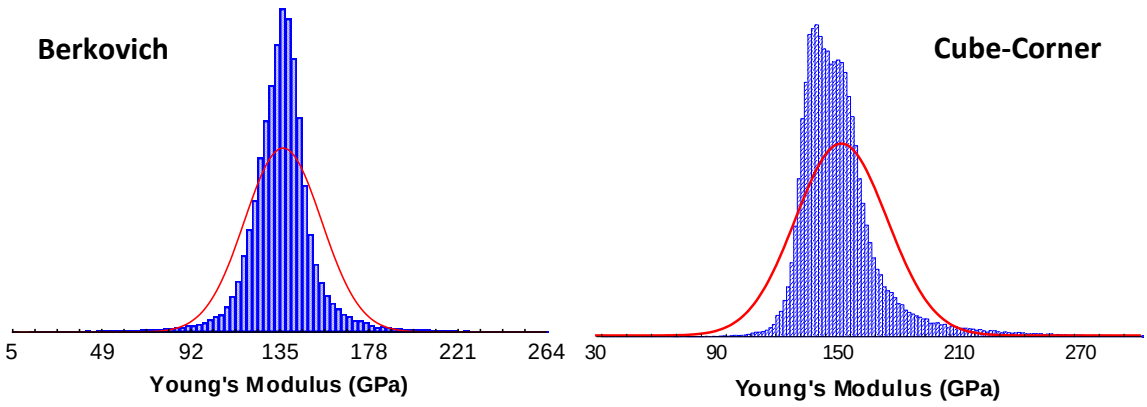

Figure 50: Distribution of the Young's Modulus obtained with Berkovich (left) or Cube-Corner indenter (right) for specimen TA6V4.

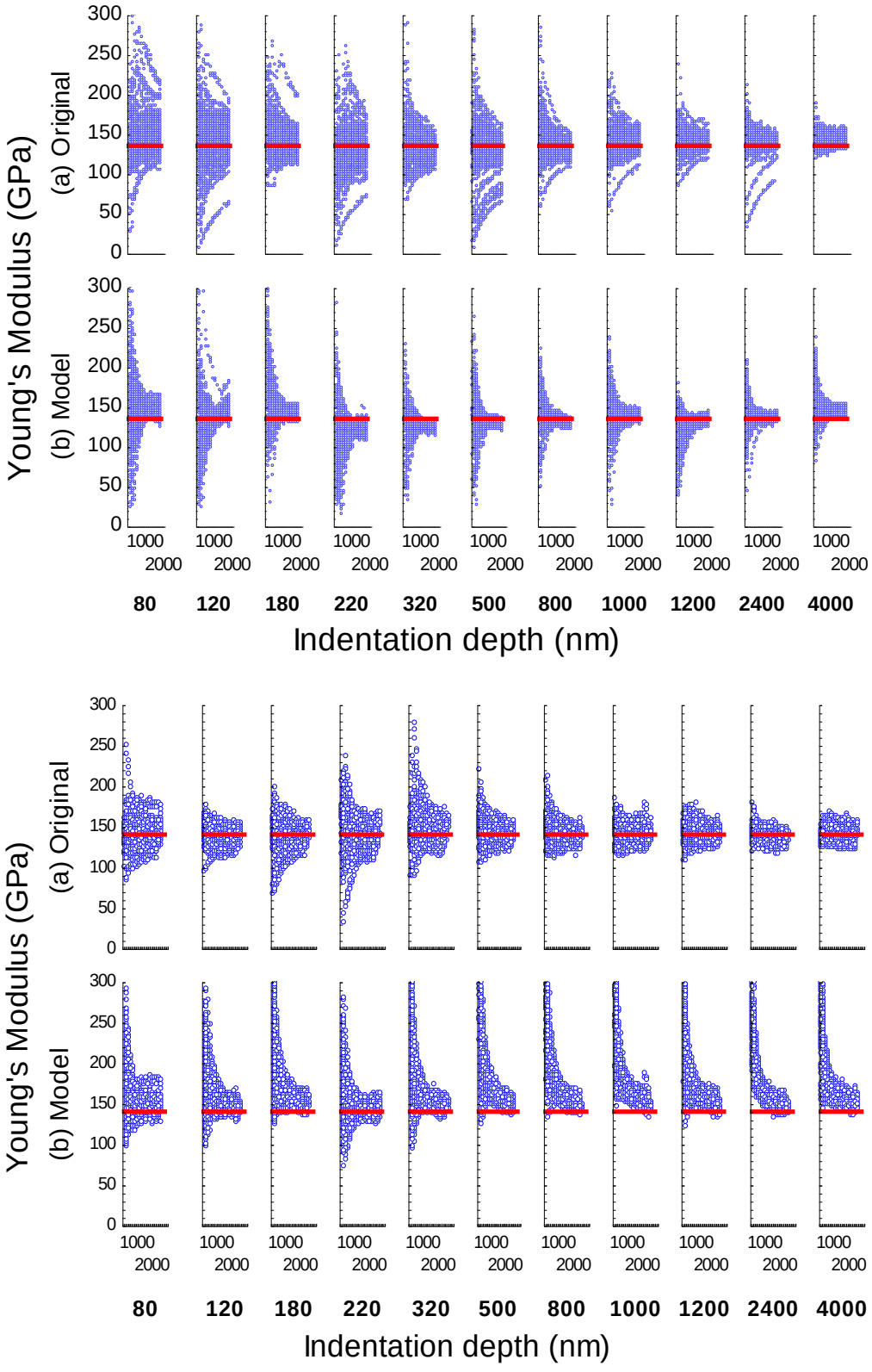

Figure 51: Evolution of the Young's modulus *versus* the indentation depth (a) ignoring or (b) considering the initial contact depth error obtained with Berkovich (up) and Cube-Corner (down) indenter for each TA6V4 specimen.

IV.6 Origin of the initial contact depth error

The observation of the experimental loading-depth curves enables the identification of two types of errors, whatever the indenter used to make the indentation, as illustrated in Figure 43. The first subpopulation gathers many curves showing a low scatter (group number 5 in Figure 52). Other individual curves are part of the other subpopulations. All the subpopulations are noticeable when studying the distribution of the initial contact depth error (see Figure 52 for specimen 2400). Take the specimen 2400 as an example, the correspondence between the scatter of loading-depth curve and the distribution of initial contact depth error performed with Berkovich indenter is established. As shown in Figure 52, the subpopulation gathering of a few curves, indicated by four red arrows, corresponds to the four experiment curves labeled by the same numbers in Figure 43. This is part of the systematic errors that result from a false detection of the first contact by the nanoindentation device. On the other hand, the last subpopulation number 5 (including many curves) shows lower scatter, which may arise from different phenomena such as measurement noise, indenter tip defect, temperature variation, or roughness. Obviously, the errors belonging to this part is the main origin of the initial contact depth error.

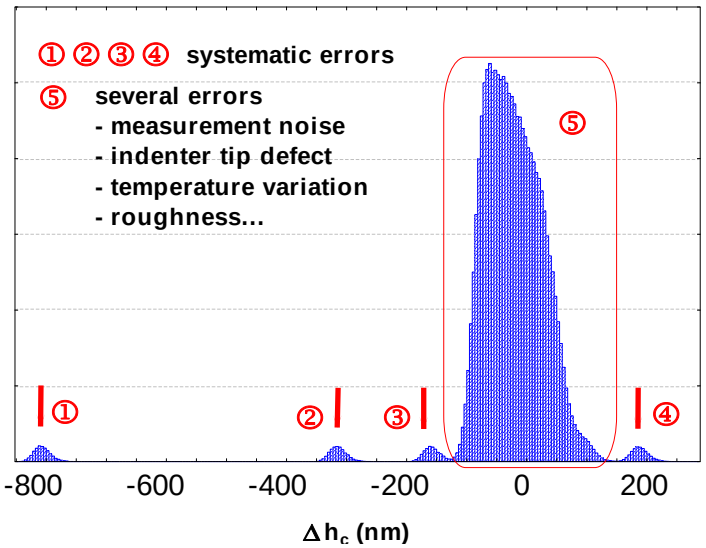

Figure 52: Distribution of the initial contact depth error performed on the TA6V4 specimen 2400 with Berkovich indenter.

Figure 53 shows the distribution of the initial contact depth error obtained with Berkovich and Cube-Corner indenters for each TA6V4 specimen. For both indenters, the scattering of the initial contact depth error decreases for a high grit paper (*i.e.,* a smooth

surface), which highlights the effect of surface topography on the scattering of the indentation curves.

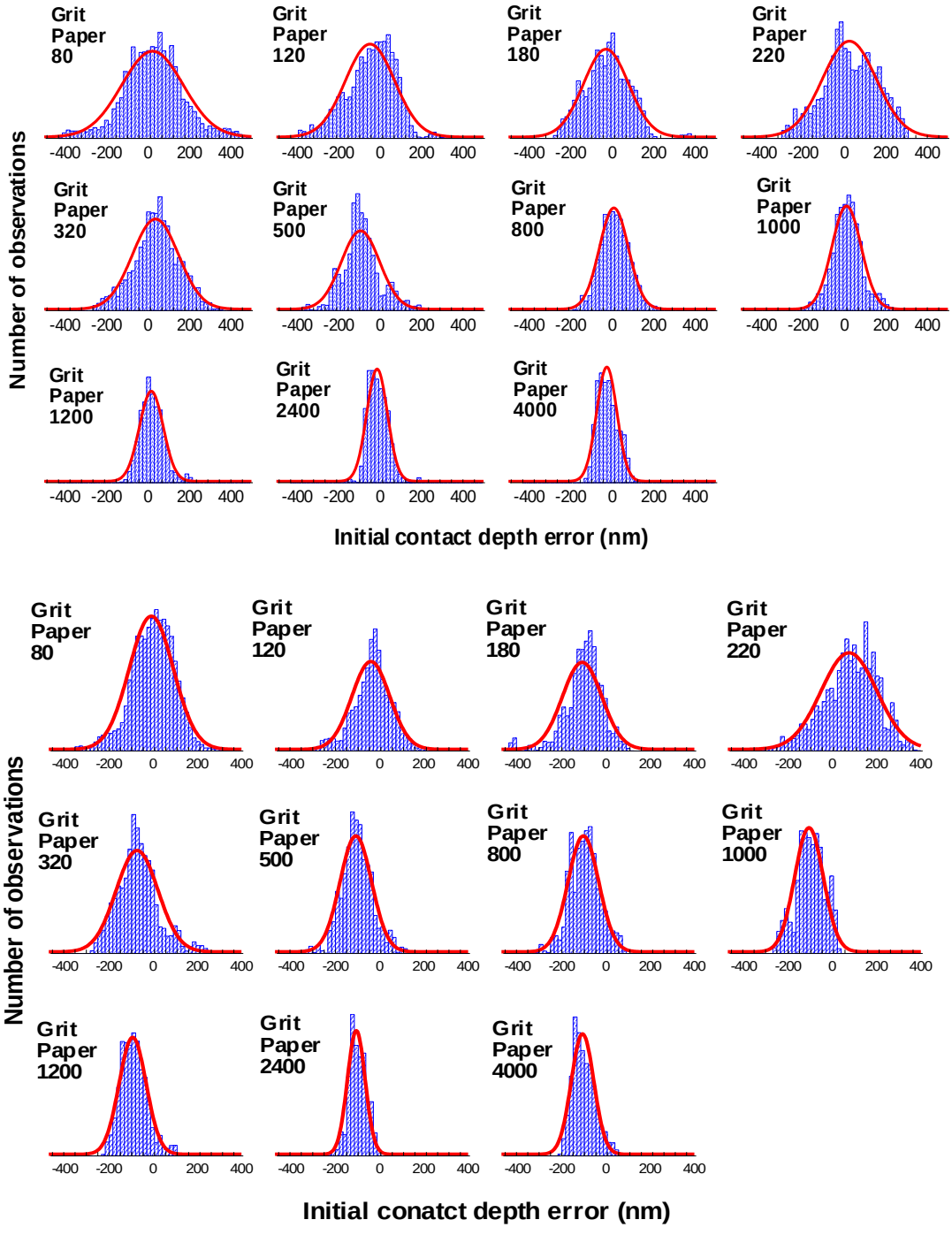

Figure 53: Distribution of the initial contact depth errors obtained with Berkovich (up) and Cube-Corner (down) indenters for each TA6V4 specimen.

This scatter is characterized by the standard deviation of initial contact depth error. When the grit paper changes from 80 to 4000, the standard deviation of initial contact depth error increases from 49.51 nm to 146.98 nm for the Berkovich and from 50 nm to 100 nm for

the Cube-Corner (excepting for specimen 220 whose standard deviation is around 124 nm), respectively. It is reasonable to conclude that the surface roughness is the main origin of the initial contact depth error and it seriously affects the accuracy of the determination of the mechanical properties using instrumented indentation test.

IV.7 Relationship between surface roughness and initial contact depth error

In order to quantitatively investigate the relationship between the surface roughness and the initial contact depth error, the a multi-scale analysis of the roughness, as mentioned in Chapter III Section 3.1, is applied to find the most accurate scale for the evaluation of each roughness parameter. The basic idea is that the best scale for roughness identification is given when the optimal linear relation is found between the standard deviation of the initial contact depth error and the root mean square roughness parameter, calculated using the selected evaluation length. Figure 54 plots the evolution of the linear correlation coefficient for this relation. The results suggest that the best evaluation length for roughness characterization is around 15 µm for Berkovich indenter and is around 5 µm for Cube-Corner indenter, which is in the same scale with corresponding indentation imprint. In this scale, the indenter can be considered as a surface "probe". In another word, the initial contact depth error correction is just like to shift the indentation curves according to the amplitude of surface topography. The surface topography variations are approximately equal to the deviations of the experimental data from conventional hardness description.

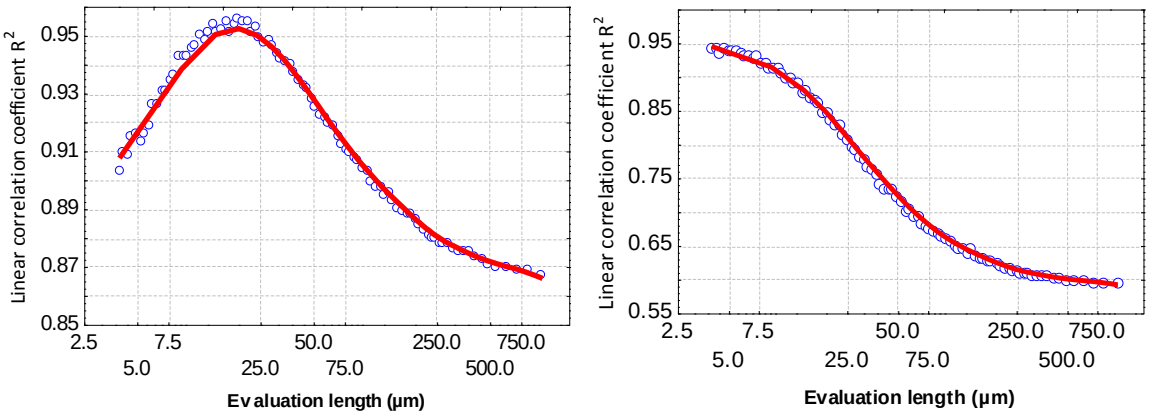

Figure 54: Evolution of the linear correlation coefficient for the relation between the standard deviation of the initial contact depth errors and RMS roughness parameter calculated using different evaluation length for Berkovich (left) or Cube-Corner (right) indenter.

Figure 55 shows that a linear relation between the standard deviation of the initial contact depth error and the roughness parameter Rq, which is obtained using an evaluation length of 15 µm and 5 µm for the corresponding indenters. It clearly means that the linear relation between roughness and the initial contact depth error is due to the analysis of the surface roughness at a length scale below the indentation size, since all wave forms higher than this size is removed by the high-pass filter process. It shows the effectiveness of the initial contact depth error correction. The proposed model allows estimation of the mechanical properties, based on the nanoindentation test on a rough surface, without bias linked to the roughness itself.

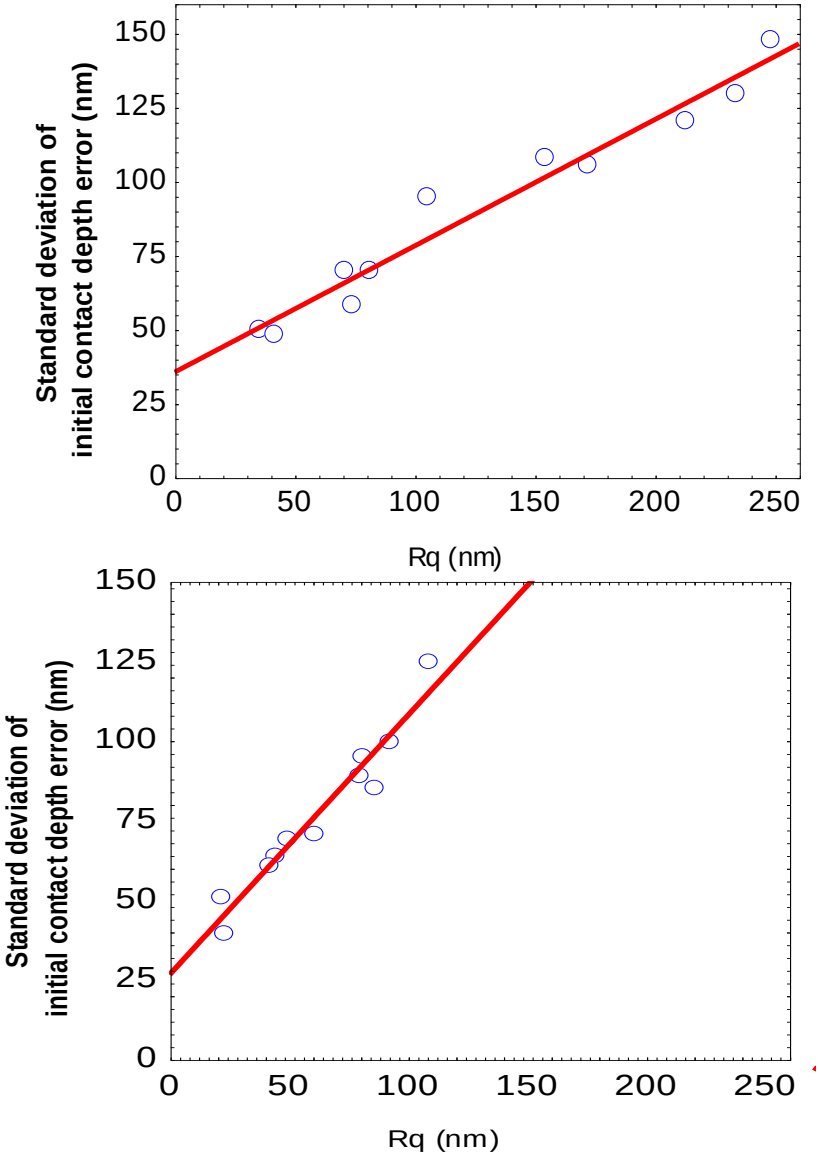

Figure 55: The linear correlation between the standard deviation of the initial contact depth errors and the RMS roughness calculated with the evaluation length equals to 15 µm for the Berkovich and 5 µm for the Cube-Corner indenters.

IV.8 Conclusion

In this chapter, the mechanical properties (Hardness and Young's modulus) of the titanium alloy specimens TA6V4 are evaluated using instrumented indentation test with Berkovich and Cube-Corner indenter. According to the experimental loading-depth curve data, the material parameters of the titanium alloy specimens are determined via the proposed method that simultaneous analyzing the indentation curves with the consideration of initial contact depth error (method A in chapter III). It is found that the scatter between the experimental loading-depth curves can be effectively diminished by our method, whatever the used indenter. The mechanical properties obtained by Berkovich indenter are compared with the one obtained by Cube-Corner indenters. The identified hardness determined by the Cube-Corner indenter are higher than the ones obtained with the Berkovich indenter. It is reasonable because the sharper cube-corner indenter displaces a much larger volume of material for a given load and thus produces higher stresses beneath the indenter shaper.

Subsequently, based on the proposed method, the relation of the identified standard deviation of the initial contact depth error and the root mean square roughness parameter is studied. The results show that the standard deviation of the initial contact depth error will increase significantly with an increase of the surface roughness, and a linear relationship will be found for these two variations when the best evaluation length is chosen to calculated the surface roughness. The best evaluation length is around 15 µm for Berkovich and 5 µm for Cube-Corner indenter, respectively, which is just in the same scale with the corresponding indentation imprint.

Chapter V Application of the numerical method on replicated surface

V.1 Overview

To investigate the effect of the surface roughness on the initial contact depth error of nanoindentation data, one of the effective means is to compare the initial contact depth error of nanoindentation test performed on two surfaces with the same roughness. For getting two surfaces with the same roughness, the surface replication technology is therefore used in our study. In this chapter, the principle of surface replication is presented. The similarity between the replicated surface and the model surface is analyzed. The nanoindentation data performed on the replication surface are analyzed using the numerical method developed in the previous chapter and the results are compared with the nanoindentation data performed on the model surface.

V.2 Surface replication

Replication is a non-destructive method to duplicate the surface topography by casting or impressing material onto the surface. It is widely used to study the surfaces of mechanical components that are inaccessible to be directly measured, e.g. a component too heavy or too large or too difficult to be dismantled from an entire system for measurement. With the replication technology, the replicas reproduce the geometrical details of the original surface with reasonable accuracy and presents an inverted image of the original surface, and then the topography of the original model surface can be assessed by measure the replica surfaces using a measurement instrument.

In the replication experiment, 7 specimens of TA6V4 polished with the grit paper 80, 120, 220, 500, 800, 1200, and 2400 are chosen as the model surfaces. The material used for the replicas is MD-3P from Plastiform (France). It is made of three components (resin, powder, hardening agent), which polymerize at room temperature after mixing. In the replication test, the replica resin and filling powder were mixed in a ratio of about 1:1 (1 dose of powder and 1 dose of resin). Then, ½ dose of the hardening agent was added to the pre-produced mixed liquid. A spatula is used in the mixing process in order to prevent any air bubbles and to ensure the product is homogeneous. The mixture is opaque and has a liquid initial consistency. Then the mixed MD-3P liquid was poured onto the model surfaces of 7 samples of TA6V4. After a curing time of 10 minutes, rigid impressions are obtained.

V.3 Comparison of replication surface and model surface

The replication surface and model surface are measured with 3D optical interferometer with Vertical Scanning Interferometry (VSI) mode as described in Section II.2.3. The surface topography features of the original surfaces and their replicas were then compared over several scales using a multiscale analysis. More specifically, the root mean square roughness parameter R_q was evaluated on 17 evaluation lengths (Tested evaluation lengths L = 6, 7, 9, 10, 13, 15, 19, 23, 29, 36, 45, 56, 74, 99, 127, 178, 297, 445 and 891 µm) with three robust Gaussian filters: a high-pass filter, a low-pass filter and a band-pass filter. For the band-pass filter, the bandwidth for each indicated value is equal to the difference between the corresponding lower cutoff evaluation length and the following greater value. For example, when the evaluation length is equal to 99 µm then the bandwidth is equal to 127-99 = 28 µm. The use of these Gaussian filters with several assessment lengths allows access to different levels of waviness and surface roughness. The aim is to identify whether the similarity of the roughness parameter of the replication and model surface is sensitive to the evaluation length. The effect of the coupling of a filter and an evaluation length on the reconstructions of the same topographies for replication and model surface are illustrated from Figure 56 to Figure 59. The topographies are rectified by a second-degree polynomial regression fitting corresponding to three different evaluation lengths from 6 to 891 µm with high-pass filter and low-pass filter. These figures show that very different features of surfaces are obtained depending on the filtering. When using a high-pass filter, more and more topography details are observed as the evaluation length increases. But for a low-pass filter, there are fewer topography details with the use of larger evaluation lengths. Similarly, depending on the evaluation length, substantially different results are obtained for the roughness parameters. For a given evaluation length, the rectification profile obtained from the high pass filters reveals the micro-roughness.

L(µm)	Model surface of specimen 80	Model surface of specimen 500
445	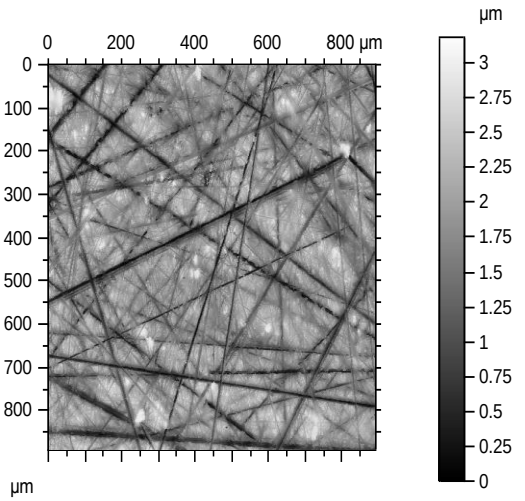	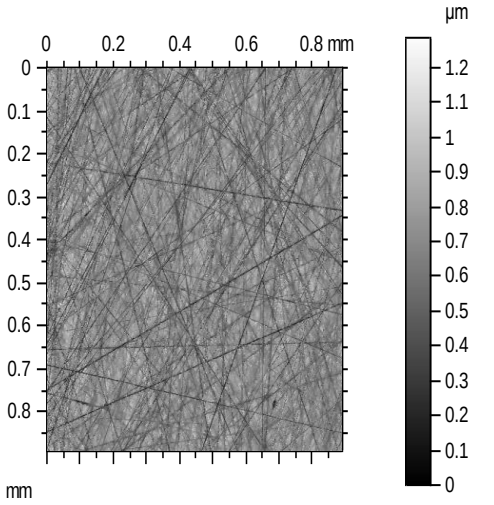
45	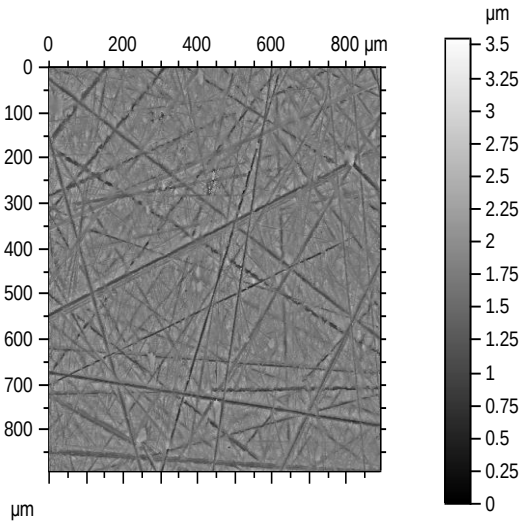	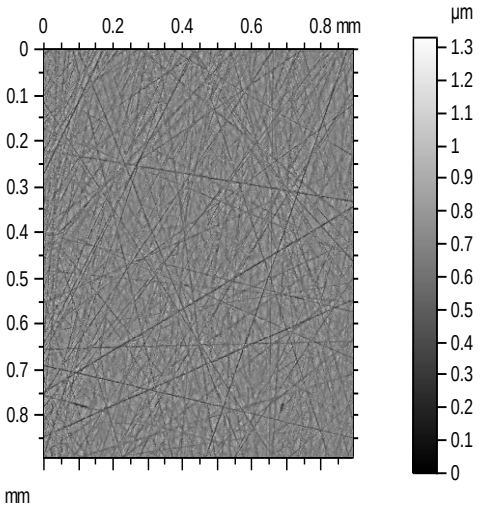
15	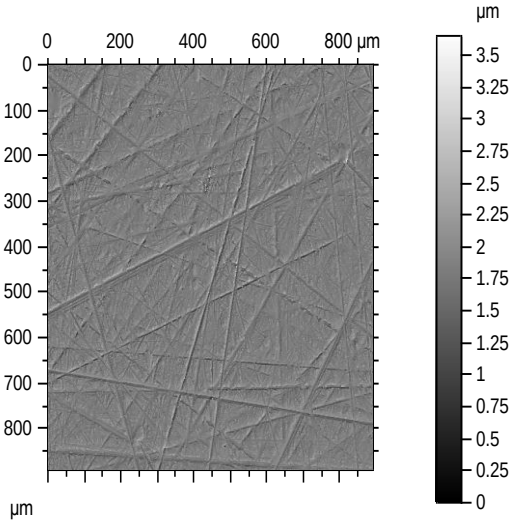	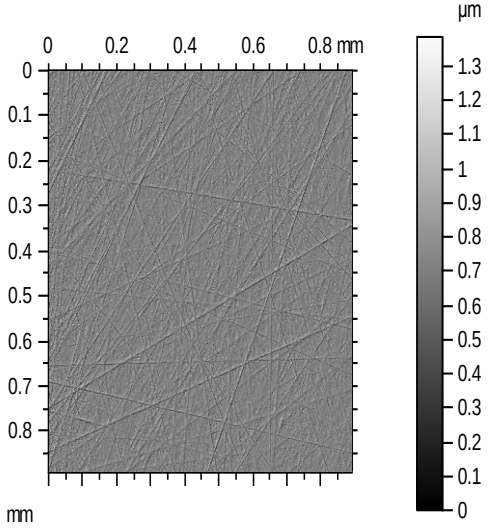

Figure 56: Model surfaces observed with high-pass filter.

L(µm)	Model surface of specimen 80	Model surface of specimen 500
445	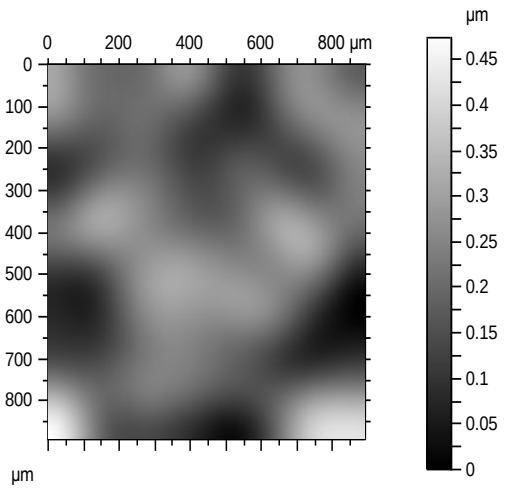	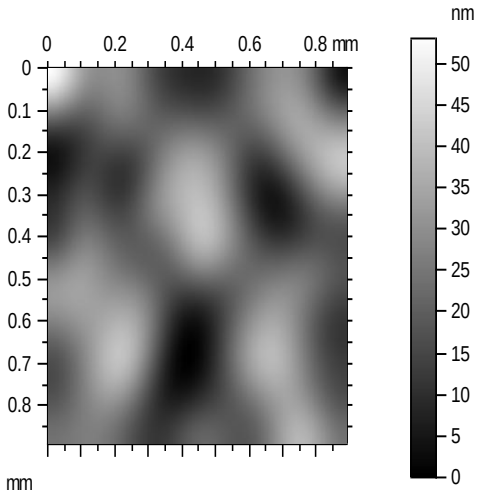
45	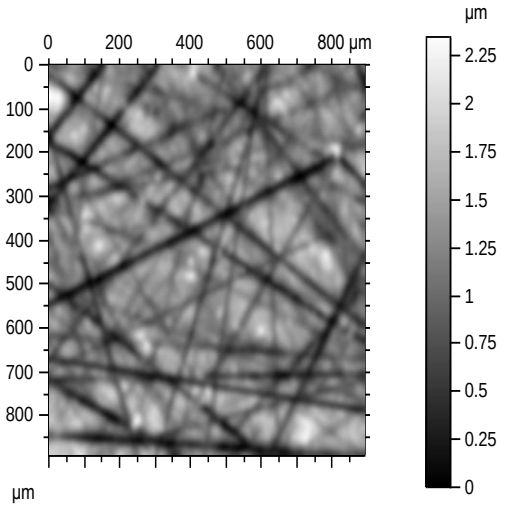	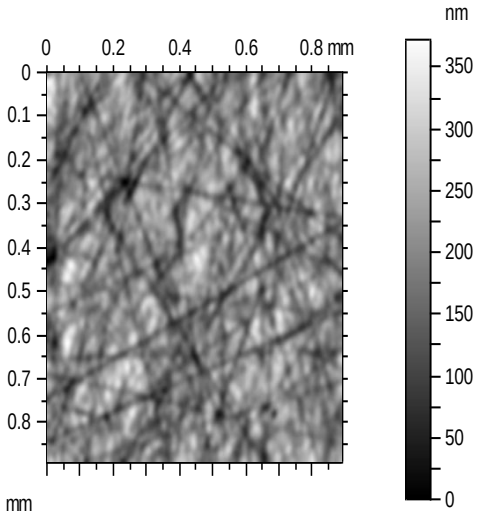
15	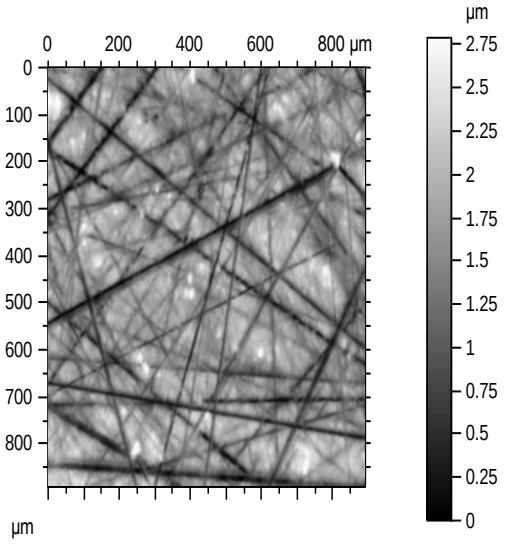	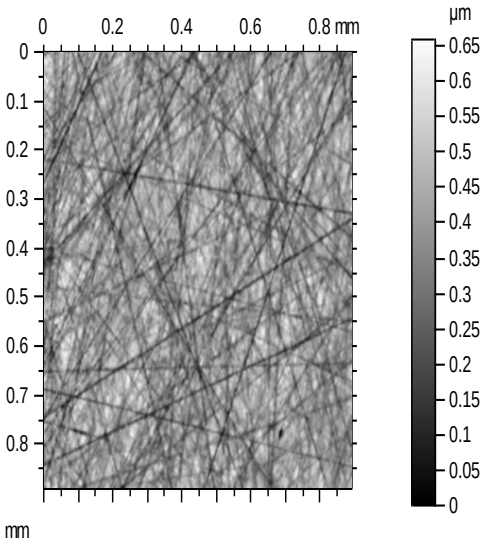

Figure 57: Model surfaces observed with low-pass filter.

L(µm)	Replication surface of specimen 80	Replication surface of specimen 500
445	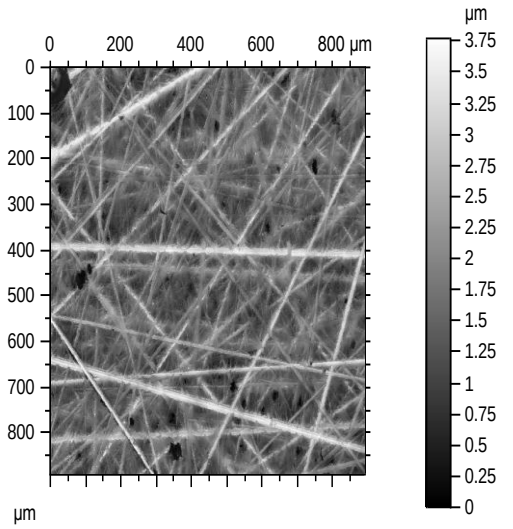	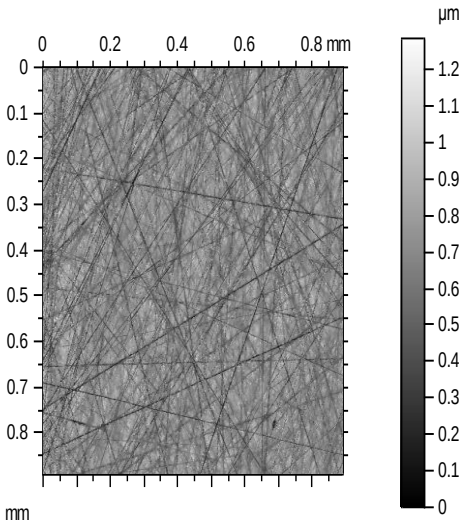
45	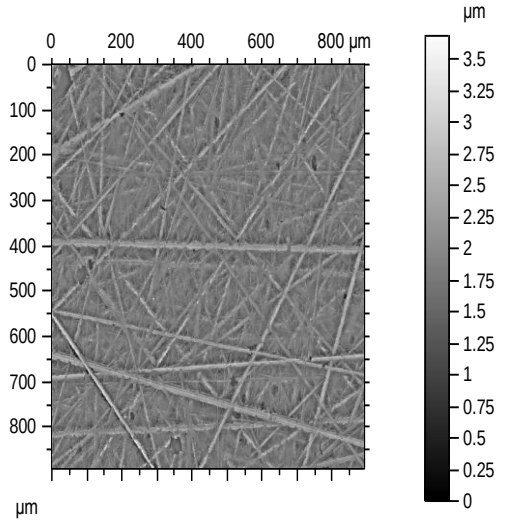	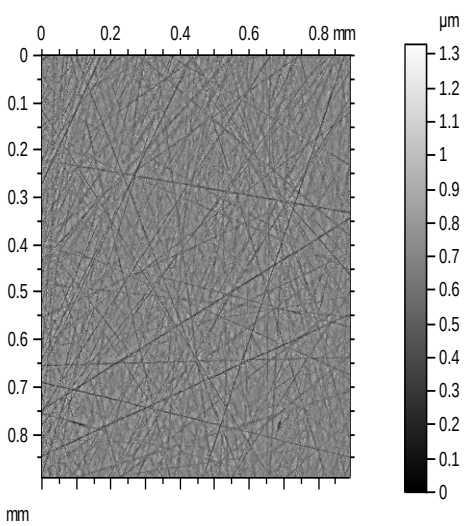
15	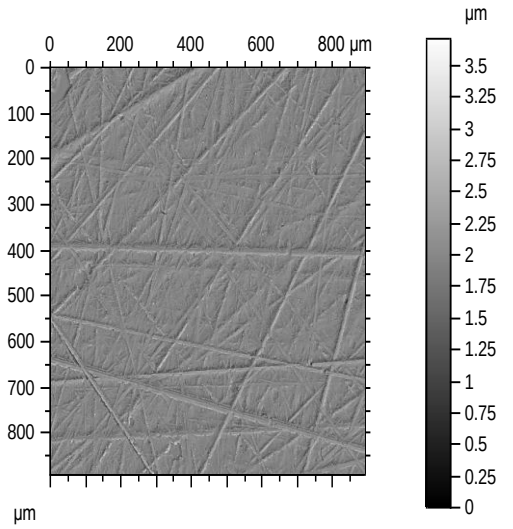	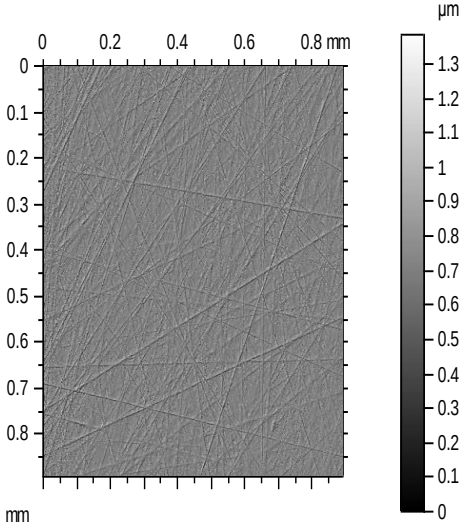

Figure 58: Replication surface observed with high-pass filter.

L(µm)	Replication surface of specimen 80	Replication surface of specimen 500
445	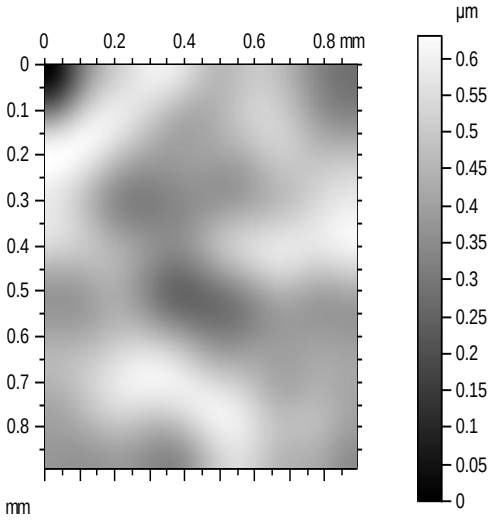	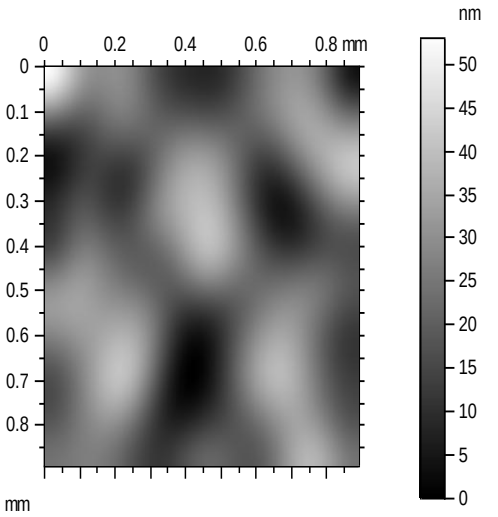
45	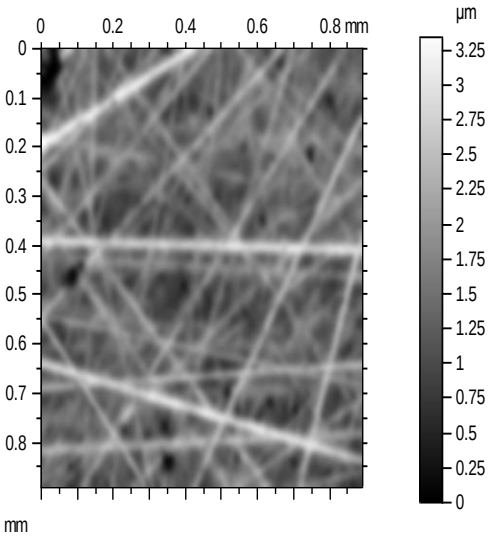	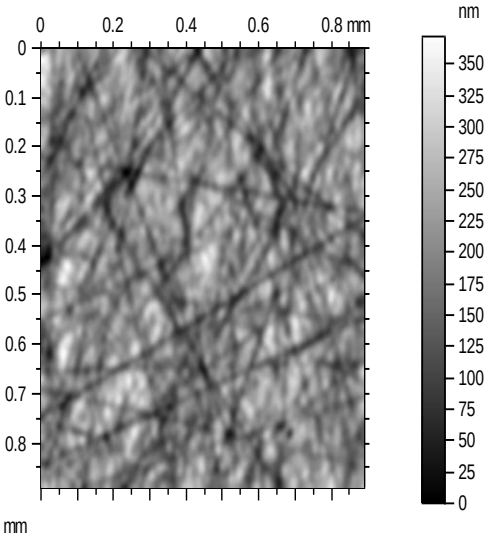
15	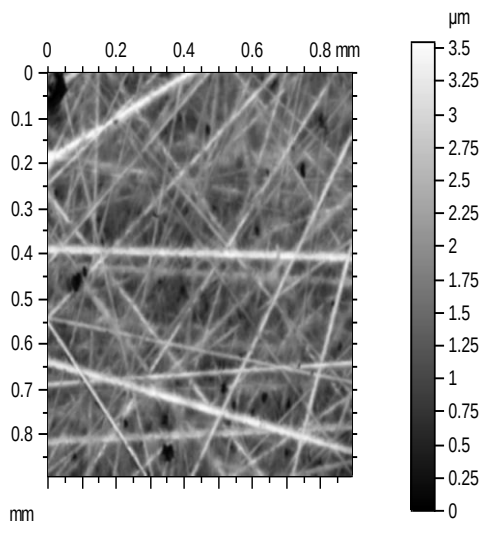	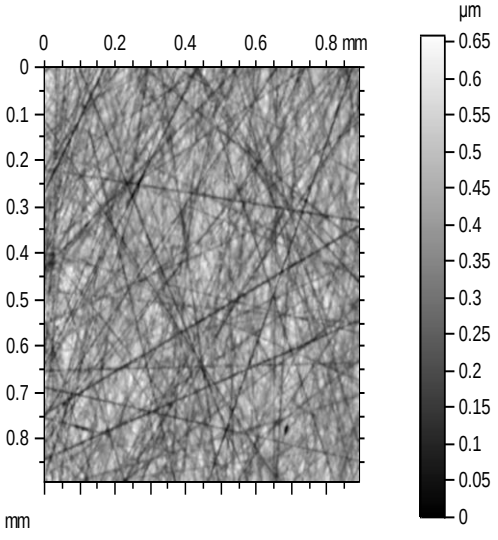

Figure 59: Replication surface observed with low-pass filter.

To compare the similarity of topographies between the replication and model surface, a better indicator may be a transfer function of the roughness parameter Sq, which corresponds to the parameter Rq when we investigate the surface profile in 2D measurement. Figure 60 shows the results found for the transfer function (Sq (replica)/Sq(model)) as a function of the evaluation length (x-axis) for the three types of filter (different colors), for the specimens polished with grit paper 120 and 2400.

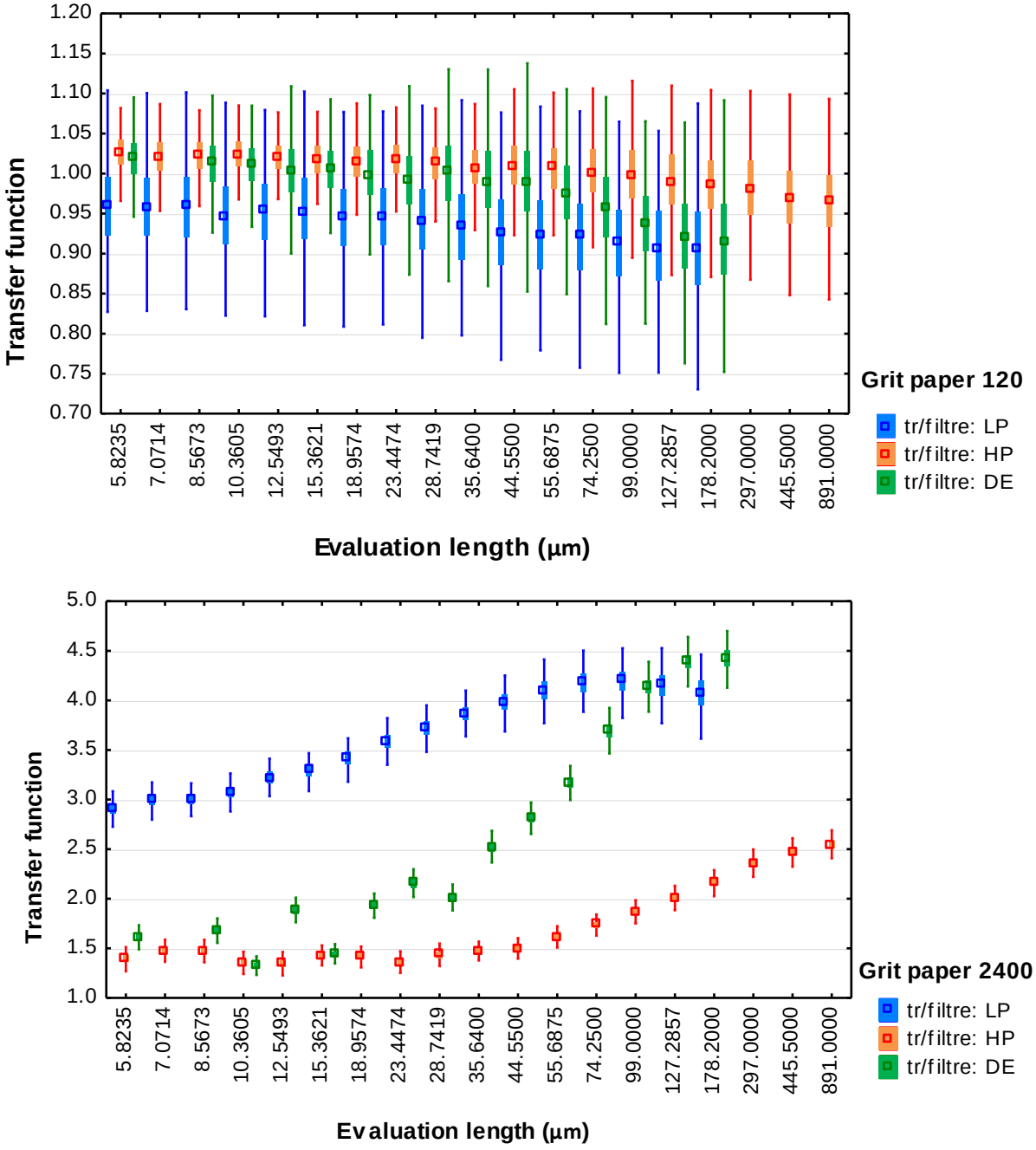

Figure 60: Transfer function (Sq (replica)/Sq(model)) as a function of the evaluation length for the three types of filter for the specimens polished with grit paper 120 (up) and 2400 (down).

The transfer function values for the surface 120 are globally equal to 1 whatever the filter type and the evaluation length. It means the replicated and the model surfaces are really similar. But for the surface 2400, the transfer function value is significantly affected by the filter type and the evaluation length. For the low-pass filter, the transfer function value is almost equal to 3 whatever the evaluation length is used on calculation. It means the difference between the replication and model surface will appear when we process the surface topographies with low-pass filter. For the high-pass filter and band-pass filter, the transfer function value is around 1 when the evaluation length is around 15 µm. Then, especially when the evaluation length is higher than 30 µm, the transfer function increases with the increasing of the evaluation length and arrives to 2.5 and 3 for high-pass filter and band-pass filter, respectively. Therefore, the replication and model surface are similar enough when the surface topographies are processed with the high-pass filter or band-pass filter as the evaluation length is around 15 µm. This evaluation length is just in the same order with the indentation imprint performed with Berkovich indenter. Thus the surface similarity is enough for investigating the effect of the surface roughness on the indentation tests with Berkovich indenter.

Figure 61 illustrates the transfer function as a function of the grit paper for the three types of filter with the evaluation length equals to 15 µm.

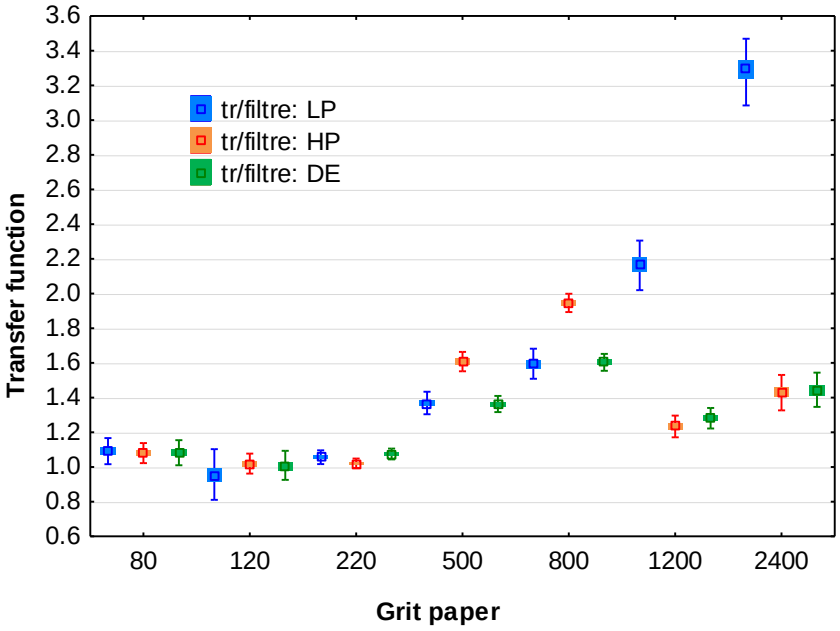

Figure 61: Transfer function as a function of the grit paper for the three types of filter with the evaluation length equals to 15 µm.

For all types of filters, the transfer function value is around 1 for the rough surface from grit paper 80 to 220, and then it increases with the increasing of the grit paper. Especially for the low-pass filter, the transfer function arrives to 3 for the grit paper 2400. Globally, it seems that, with the MD3P replica, rough surfaces are better replicated than smooth surfaces. A possible explanation of this trend is the replica viscosity. Large viscosity prevents an accurate replication of features having small amplitude and spacing. To test this hypothesis, the waviness and maximum height of the replicated and the model surfaces should be observed.

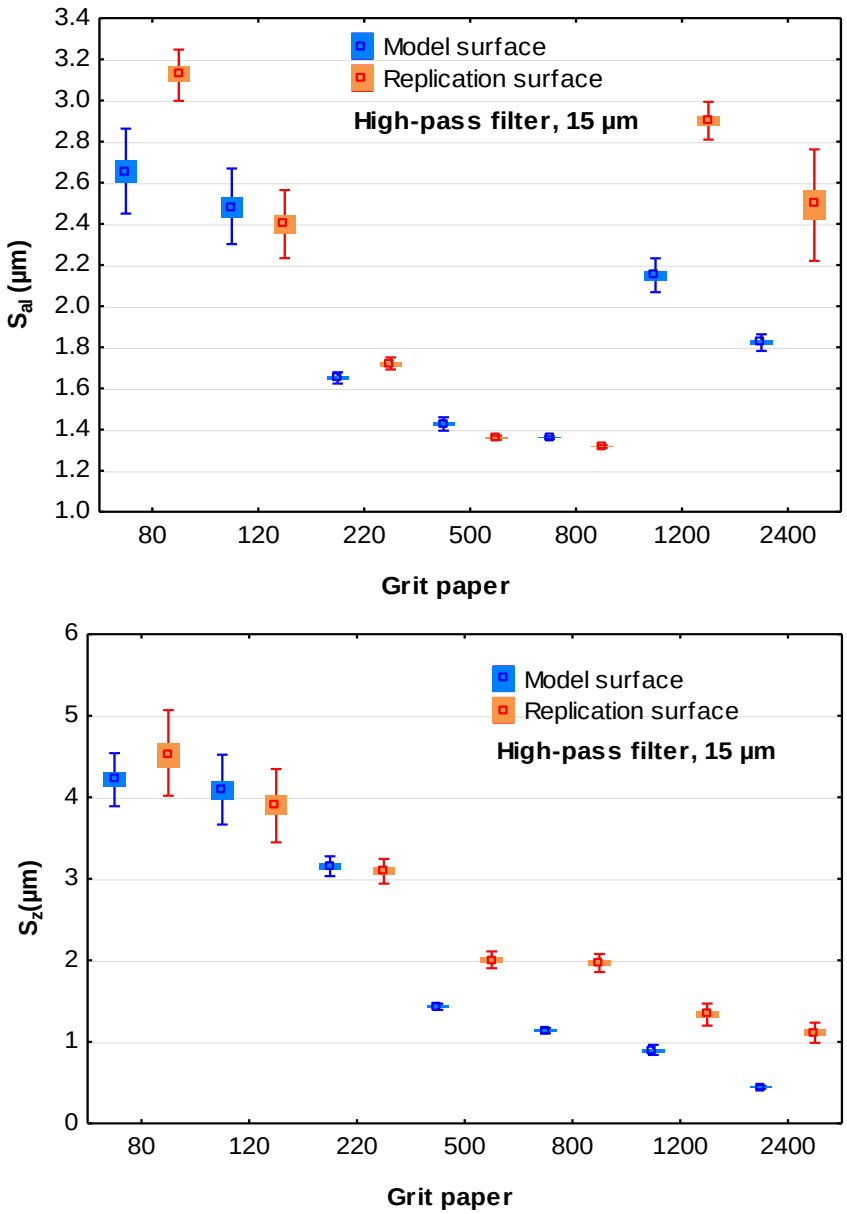

Figure 62: Autocorrelation length S_{al} (up) and maximum height S_z (down) of the replicated and the model surface as a function of the specimen numbers, calculated using a high-pass filter with the evaluation length equals to 15 µm.

The roughness parameter enabling to analyze the roughness maximum height is S_z while the one enabling to describe the surface global pattern is the autocorrelation length S_{al}. The latter represents the profile memory: it is the length from which the studied pattern repeats itself. Figure 62 present the data obtained for the autocorrelation length and the maximum height of the surface, respectively. It can be seen that the S_{al} values first decrease for grits ranging from 80 to 800 and then they increase for larger grit-numbers. Conversely, the S_z values steadily decrease with an increase of the grit-numbers. Thus, for specimens polished with coarse grit papers (e.g. Specimen 80), both the amplitude and the length over which it varies are large. Then, specimens polished with slightly finer grit papers show a decrease of both the amplitude and the variation length with certain proportionality (e.g. Specimen 220). Finally, for specimens polished with very fine grit papers (e.g. Specimen 2400), this proportionality between the amplitude and the variation length disappears: the amplitude keeps decreasing compared with surfaces obtained with coarser grit papers while the variation length increases. These variations, summarized in Figure 63, probably explain why rough surfaces are better replicated than smooth surfaces.

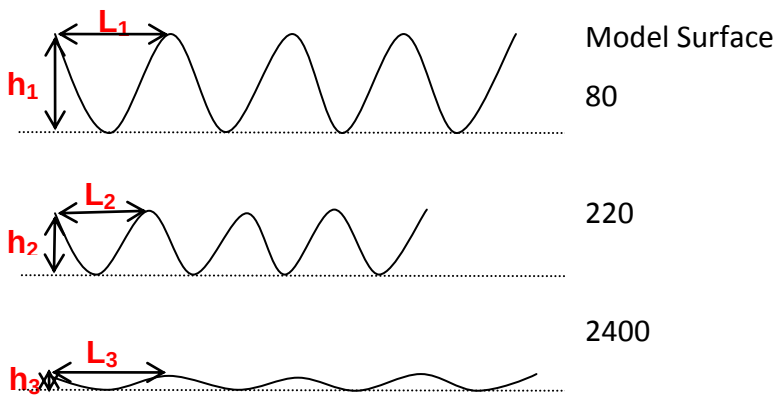

Figure 63: Diagram of the roughness of the specimens polished with 80, 220 and 2400 grit papers.

As discussed above, it can be concluded that the replication surface is similar with the model surface with the high-pass and band-pass filter treatments when the evaluation length is around 15 µm. In order to study the effect of the surface roughness of the replication material on the nanoindentation test, the small details of the replication surface is more important than the waviness. Thus the high-pass filter is used in the following study.

V.4 Macro-hardness and ISE factor of replication material

Nanoindentation test are performed with Berkovich indenter on the replication materials as described in Chapter II.2.5.5. Then the loading-depth curves are analyzed by the proposed numerical model. The macro-hardness and the ISE factor of replication materials as function of grit paper are shown in Figure 64. The macro-hardness is nearly in accordance with the value given by the Corporation PLASTIFORM, around 0.18 GPa. The ISE is zero for all the replication specimens. The probably reason is that the material is so soft that the pile-up doesn't occur here.

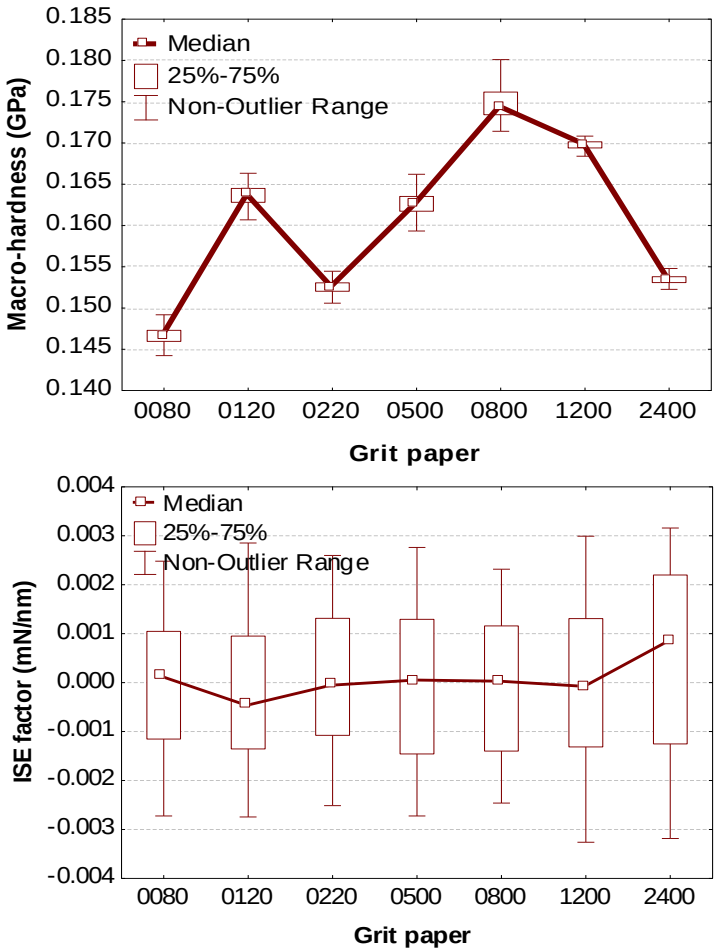

Figure 64: Macro-hardness and ISE factor of each replication specimen.

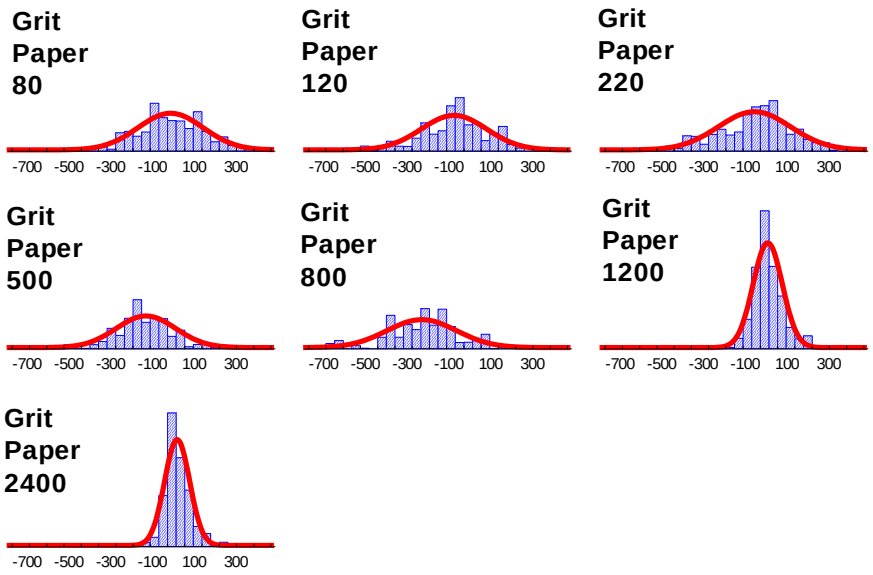

Figure 65: Distribution of the initial contact depth error.

The distribution of the initial contact depth errors is shown in Figure 65. Similar with the analysis for the specimens with model surfaces, the standard deviation of the initial contact depth errors still globally decreases with the surface roughness. The linear relationship between the standard deviation of the initial contact depth errors and the surface roughness parameter calculated when the evaluation length is equal to 15 µm with high-pass filter is plotted in Figure 66.

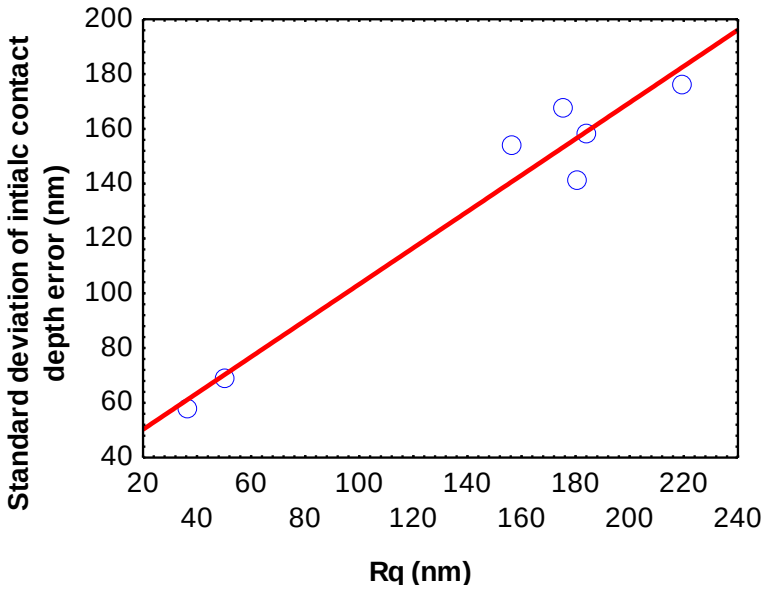

Figure 66: Relationship between the initial contact depth error and surface roughness parameters for each replication specimen.

To compare the nanoindentation data performed on model surface and replication surface obtained with Berkovich indenter, the standard deviation of the initial contact depth errors of these two groups of instrumented indentation data are compared with a variance analysis technology (ANOVA). The ANOVA technology compares these two unmatched groups of standard deviations based on a calculation of the P-value. The calculation of P-value is a type of statistical significance tests, which enables to address the probability that the relationship exists between two variables. In statistical significance tests, a null hypothesis should be assumed first, and then the P-value will be compared with a set certain significance level (often 0.05) in order to decide whether the value of the statistic test is consistent with the null hypothesis. If the P-value is less than the significance level 0.05, the null hypothesis will be rejected. Conversely, when the P-value is larger than the significance level 0.05, it means the null hypothesis is acceptable.

In our case, the two variables are the standard deviations of the initial contact depth errors for model surface (variable a) and replication surface (variable b), respectively. With the ANOVA technology, the null hypothesis is that the standard deviation of the initial contact depth errors for model surface and replication surface are identical. Therefore, if the P-value is higher than the significance level 0.05, it means there is not compelling evidence to prove that the standard deviations of initial contact depth errors for these two surfaces are different at this significance level. On the contrary, any time if the P-value is smaller than the significance level 0.05, it means the standard deviation of initial contact depth errors for these two surfaces is significantly different. The statistical significance analysis of the standard deviations of the initial contact depth errors for model surface and replication surface is shown in Figure 67. The ANOVA technology gives the P-value around 0.14, which is higher than the significance level (0.05). It suggests that the standard deviation of the initial contact depth errors for model surface and replication surface is statistically the same at this significance level.

According to these comparative experiments, for two groups of instrumented indentation data performed on two surfaces with similar roughness, the standard deviations of the initial contact depth errors will also be similar. The result proves that the surface roughness is the main effect of the initial contact depth errors.

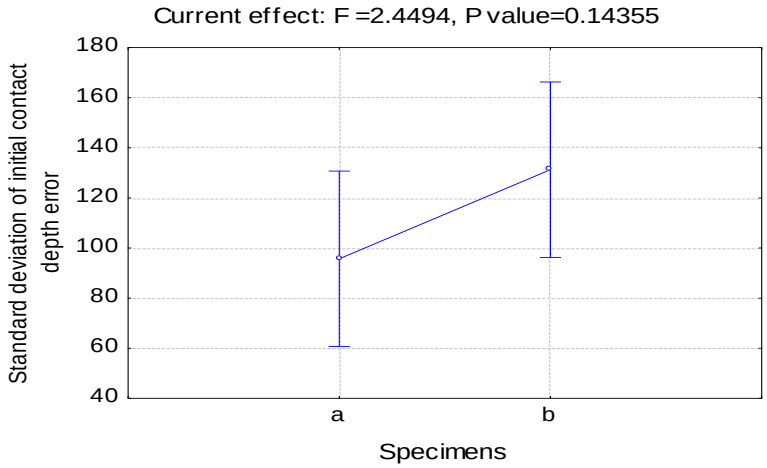

Figure 67: Statistical significance analysis of the standard deviations of the initial contact depth errors for (a) model surface and (b) replication surface.

V.5 Conclusions

In this Chapter, the surface roughness of several polished TA6V4 specimens are copied with a surface replication technology. The replication accuracy is verified by the comparison of the roughness of the model surface and its replica over several scales using a multi-scale analysis. The results show that the replication surface is similar with the model surface with the high-pass filter treatment when the evaluation length is around 15 µm. And then the instrumented indentation data performed on the model specimens and the replication specimens are investigated with the proposed method with the consideration of the initial contact depth error. It founds that the standard deviation of the initial contact depth error for model specimens and the replication specimens are also similar. The results of these comparisons between the model specimens and replication specimens suggest that the main reason for the initial contact depth error is linked to the surface roughness parameter that estimated with the high-pass filter treatment in a given evaluation length.

Chapter VI Conclusions and Prospects

This thesis is an innovative study on the accurate estimation of the mechanical properties of material from instrumented indentation testing data. Through the illustrations presented in this thesis and some researchers' investigations, we have noticed that the surface roughness of specimens is a serious and widespread problem in the identification of material parameters with instrumented indentation testing. If several indentation tests are performed on a specimen with rough surface, the roughness effect will produce an increased scatter in the load-depth curves and the identified material parameters from these curves will have high deviations. Moreover, the scatter of the indentation curves also occurs for the mirror-like surface (*e.g.* specimen polished with grit paper 4000). The main objective of this thesis is therefore to characterize the material behaviors by analyzing the instrumented indentation data excluding the surface roughness effect on the identification of material parameters. For this purpose, an original statistical numerical method for analyzing the instrumented loading-depth curves is proposed in the present thesis. Four representative materials (*e.g.* 316L, AU4G, and TA6V4), two different surface processing methods (*e.g.* polishing and sandblasting), and a surface replication technique are used to verify the robustness of the proposed method. The effect of surface roughness of these specimens on material properties (*e.g.* macro-hardness and Young's Modulus) identifications is assessed quantitatively. Moreover, the instrumented indentation data performed with two types of indenter (*e.g.* Berkovich and Cube-Corner) are investigated to further prove the universality of this method and to evaluate the sensitivity of the best evaluation length for surface roughness analyzing towards the different indenter geometry. According to the investigations mentioned in this thesis, a deep understanding of the effect of the surface roughness on the identification of material mechanical properties from instrumented indentation testing is achieved. The proposed method enables to improve the reliability of material parameter identified from the indentation testing. The key contributions of this thesis are the following:

1) An original statistical treatment model of the load-depth curves from the instrumented indentation test is proposed for the determination of the macro-hardness and Young's modulus with the quantification of indentation size effect.

Normally, in order to reduce the dispersion of instrumented indentation results, the mechanical properties are estimated separately from each experimental load-depth curve, and then take the average value of these mechanical properties as the final results. In the

present work, an improved method to accurately calculate the mechanical properties of material from instrumented indentation curves with the consideration of indentation size effect is proposed. The most significant feature of this model is the simultaneous statistical treatment for a set of the loading-depth curves, whose locations are set by a specific definition of the initial contact depth error ($\Delta h_{ci,i\in I}$), defined as a gap between the individual experimental loading curve i and the simulated one using Bernhardt law. In order to verify the robustness of the proposed method, it is applied to numerous loading-depth curves (one hundred per sample) for different specimens (different materials, different processes for surface generation, and different indenters). For each specimen, the results always show that the deviation of the mechanical properties obtained from the proposed method is smaller than the one obtained from the usual method calculated with mean value. It proves more accurate mechanical properties can be obtained from the proposed model.

2) The effect of surface roughness on the determination of the mechanical properties is investigated quantitatively.

Through the application of the proposed method to a large number of instrumented indentation tests performed on specimens with different surface morphologies, we found that the standard deviation of the induced initial contact depth error decreases with the decreasing of the surface roughness. Therefore, it is crucial to find a method to evaluate the influence of the surface roughness on the distribution of initial contact depth error (*i.e.* the dispersion of indentation curves). In this thesis, the relationship between the standard deviation of initial contact depth error ($\sigma(\Delta h_c)$) and the root mean square roughness parameter (Rq) is examined using the proposed model combined with a multi-scale roughness analyses method. The latter is used to calculate the surface parameters with different evaluation lengths. According to these analyses, a linear relationship between $\sigma(\Delta h_c)$ and Rq calculated from a best evaluation length is obtained. It suggests that the surface roughness of specimens is the main origin of the initial contact depth error. In other words, the effect of surface roughness on the mechanical properties determination can be reduced by the consideration of the initial contact depth error in the model. It quantitatively proves the fact that the proposed method is able to estimate the mechanical properties of material unrelated to the surface roughness of specimens. This fact is also proved by the comparison study between the replication surface and model surface in Chapter V. The

application of the replication technology enables to copy the surface roughness of the model surface. By the comparison of the instrumented indentation data performed on the replicated surface and the model surface, it found that the standard deviations of the initial contact depth error are similar for different materials having the similar surface roughness (replication surface and model surface). It suggests that the main origin of the initial contact depth error is the surface roughness. The considering of the initial contact depth error in the proposed model is help to exclude the surface roughness effect on the instrumented indentation data and enables to determine the mechanical properties of materials accurately.

3) The sensitivity of the best evaluation length for surface roughness analyzing towards the different indenter geometry is presented.

Thanks to the proposed model and the multi-scale surface roughness analyses method, a best evaluation length for the surface parameters estimation is chosen for each type of specimen. With this best evaluation length, the calculated surface parameter is the most relevant to the standard deviation of initial contact depth error. Generally speaking, two best evaluation lengths are chosen in this thesis: 15 µm and 5 µm. It is worth to note that these two values are obtained for the specimens that the instrumented indentation testing is performed by Berkovich indenter or Cube-Corner indenter, separately. In our cases, whatever the specimens are studied, as long as the indentation tests are performed with Berkovich indenter, the best evaluation length for specimen's surface parameters calculation is around 15 µm which is just equal to the contact dimension of Berkovich indenter in 3000 nm. Similarly, this value for Cube-Corner indenter is around 5 µm. It means that when we investigate the effect of the surface roughness on instrumented indentation data, the best evaluation length for surface parameter evaluation is sensitive to the geometry of the indenter. The greatest effects of surface roughness on indentation data are encountered when the wavelength of the roughness is comparable to the contact dimensions of indenter. Thus, it is reasonable that the best evaluation length is related with the used indenter.

Before closing this thesis, it is important to point out that this does not imply the end of the work on this subject. Much more efforts could be made to improve the estimation of mechanical properties by instrumented indentation testing. On the one hand, the statistical model that analyzed the instrumented indentation curves with consideration of surface effects has been tested on different materials, different types of surface treatment, and

different types of sharp indenter to examine the validity for numerous surface morphologies or material characteristics. In fact, its application could also be extended to spherical indenters. However, this requires replacing the Bernhardt law for the spherical indenters to better describe the load-depth curves for a wide range of materials. Similarly, the consideration of indentation size effect needs to be adapted to the case of the spherical indenter: the diameter of the spheres is the most important length scale for spherical indenters (*i.e.* spheres with a diameter less than or equal to 100 µm produce higher hardness). On the other hand, the developed model was used to significantly reduce the dispersion of the experimental load-depth curves and generate a more efficient curve to represent the material response. However, because the shapes of those sharp indenters are self-similar (ignoring the small imperfection at the indenter tips), the loading curve can provide only one independent quantity, which is a combination of the elastic and the plastic properties of the materials. Thus, a multi-scale indentation data (macro-, micro- and nano-indentation) should be considered to get different strain ratio and finally to obtain the constitutive law of material.

Reference

[1] M. Bigerelle, J.M. Nianga, D. Najjar, A. Iost, C. Hubert and K.J. Kubiak (2013) Roughness signature of tribological contact calculated by a new method of peaks curvature radius estimation on fractal surfaces. Tribol. Int. 65: 235-247.

[2] G.W. Stachowiak and P. Podsiadlo (2001) Characterization and classification of wear particles and surfaces. Wear 249: 194-200.

[3] M. Bigerelle, T. Mathia and S. Bouvier (2012) The multi-scale roughness analyses and modeling of abrasion with the grit size effect on ground surfaces. Wear 286: 124-135.

[4] A. Van Gorp, M. Bigerelle, A. Grellier, A. Iost and D. Najjar (2007) A multi-scale approach of roughness measurements: Evaluation of the relevant scale. Mater. Sci. Eng. C 27: 1434-1438

[5] A.C. Fischer-Cripps (2002) Nanoindentation. Springer, Berlin.

[6] S. Hengsberger, A. Kulik, and P. Zysset (2001) A combined atomic force microscopy and nanoindentation technique to investigate the elastic properties of bone structural units. Eur. Cells Mater. 1: 12-17.

[7] J. Hay (2009) Introduction instrumented indentation testing. Exp. Techniques 33: 66-72.

[8] W.C. Oliver and G.M. Pharr (2004) Measurement of hardness and elastic modulus by instrumented indentation: Advances in understanding and refinements to methodology. J. Mater. Res. 19: 3-20.

[9] H. Hertz (1882) On the contact of rigid elastic solids and on hardness. J. reine und angewandte Mathematik 92: 156-171.

[10] I.N. Sneddon (1965) The relation between load and penetration in the axisymmetric boussinesq problem for a punch of arbitrary profile. Int. J. Eng. Sci. 3: 47-57.

[11] S.I. Bulychev, V.P. Alekhin, M.K. Shorshorov, A.P. Ternovskii and G.D. Shnyrev (1975) Determining Young's modulus from the indenter penetration diagram. Zavod. Lab. 41: 1137-1140.

[12] G.M. Pharr, W.C. Oliver and F.R. Brotzen (1992) On the generality of the relationship among contact stiffness, contact area, and elastic modulus during indentation. J. Mater. Res. 7:613-617.

[13] G. Simmons and H. Wang (1971) Single crystal elastic constants and calculated aggregate properties: a handbook. M.I.T. press

[14] G. Guillonneau (2013) Nouvelles techniques de nano-indentation pour des conditions expérimentales difficiles : très faibles enfoncements, surfaces rugueuses, température. Thesis of University of Lyon, 20-23.

[15] M.F. Doerner and W.D. Nix (1986) A method for interpreting the data from depth-sensing indentation instruments, J. Mater. Res. 1: 601-609.

[16] W.C. Oliver and G.M. Pharr (1992) An improved technique for determining hardness and elastic modulus using load and displacement sensing indentation experiments, J. Mater. Res. 7: 1564-1583.

[17] J. Hay, P. Agee, and E. Herbert (2010) Continuous Stiffness Measurement during Instrumented Indentation Testing. Exp. Techniques 34: 86-94.

[18] J.B. Pethicai, R. Hutchings, and W.C. Oliver (1983) Hardness measurement at penetration depths as small as 20nm. Philos. Mag A 48: 593-606.

[19] A.C. Fischer-Cripps (2002) Introduction to contact mechanics, Springer-Verlag, NewYork.

[20] How to Select the Correct Indenter Tip. Agilent Technologies.

[21] S.V. Hainswortha, H.W. Chandlera, and T.F. Page (1996) Analysis of nanoindentation load-displacement loading curves. J. Mater. Res. 11: 1987-1995.

[22] F. Kick (1885) Das Gesetz der proportionalen Widerstände und seine Anwendungen : Nebst Versuchen über das Verhalten verschiedener Materialien bei gleichen Formänderungen sowohl unter der Presse als dem Schlagwerk Verlag von Arthur Felix.

[23] K. Zeng and C.H. Chiu (2001) An analysis of load-penetration curves from instrumented indentation. Acta. Mater. 49: 3539-3551.

[24] F.G. Yost (1983) On the definition of microhardness. Metall. Trans. 14A: 947-952.

[25] J. Gong, J. Wu and Z.Guan (1999) Analysis of the indentation eize effect on the apparent hardness of ceramics. Mater. Lett. 38:197-201.

[26] E. Meyer (1908), Investigations on hardness testing and hardness. VDI Zeitschriff. 52: 2077-2078.

[27] J.W. Harris, H. Stocker (1998) Spherical segment, Handbook of Mathematics and Computer Science, Springer-Verlag, New York.

[28] B. Rother, A. Steiner, D.A. Dietrich, H.A. Jehn, J. Haupt and W. Giessler (1998) Depth-sensing indentation measurements with Vickers and Berkovich indenters. J. Mater. Res. 13: 2071-2078.Z

[29] M.T. Attaf (2004) Tip bluntness determination using the energy principle and consequent correction to the indentation function. Mater. Lett. 58: 1100–1106

[30] M.T. Attaf (2004) Connection between the loading curve models in elastoplastic indentation. Mater. Lett. 58: 3491-3498.

[31] F. Fröhlich, P. Grau and W. Grellmann (1977) Performance and analysis of recording microhardness tests. Phys. Status Solidi A 42: 79–89.

[32] E.O. Bernhardt (1941) On microhardness of solids at the limit of Kick's similarity law. Z Metallkd 33: 135-144.

[33] C. Hays and E.G. Kendall (1973) An analysis of knoop microhardness. Metallurgica 6: 275-282.

[34] H. Li and R.C. Bradt (1993) The microhardness indentation load/size effect in rutile and cassiterite single crystals. J. Mater. Sci. 28: 917-926.

[35] K. Sangwal (2000) On the reverse indentation size effect and microhardness measurement of solids. Mater. Chem. Phys. 63: 145-152.

[36] B. Efron, R.J. Tibshirani (1993) An introduction to the Bootstrap. Chapman and Hall, NewYork.

[37] P. Hall (1992) The Bootstrap and the edge worth expansion. Springer, NewYork.

[38] A. Iost and R. Bigot (1996) Indentation size effect: reality or artefact? J. Mat. Sci. 31: 3573- 3577.

[39] D. Marquardt (1963) An algorithm for least-squares estimation of nonlinear parameters. SIAM Journal on Applied Mathematics 11: 431-441.

[40] K. Levenberg (1944) A Method for the Solution of Certain Non-Linear Problems in Least Squares. Appl. Math. 2: 164-168.

[41] W.C. Oliver and G.M. Pharr (2004) Review: Measurement of hardness and elastic modulus by instrumented indentation: Advances in understanding and refinements to methodology. J. Mater. Res. 19: 3-20.

[42] J. Alcalá, A.C. Barone and M. Anglada (2000) The influence of plastic hardening on surface deformation modes around Vickers and spherical indents. Acta. Mater. 48: 3451-3464.

[43] B. Dubuc, J.F. Quiniou, C. Roques-Carnes, C. Tricot and S.W. Zucker (1989) Evaluating the fractal dimension of profiles. Phys. Rev. A 39:1500–1512.

[44] M. Bigerelle, A. Gautier and A. Iost (2007) Roughness characteristic length scales of micro-machined surfaces: A multi-scale modeling. Sensor. Actuat. B-Chem 126:126-137.

[45] G. Carter, I.J. Bevan, I.V. Katardjiev and M.J. Nobes (1991) The erosion of copper by reflected sandblasting grains. Mater. Sci. Eng. A. 132:231-236.

[46] Y. Lee, J. Hahn, S. Nahm, J. Jang and D. Kwon (2008) Investigations on indentation size effects using a pile-up corrected hardness. J. Phys. D. Appl. Phys. 41:074027.

[47] J. Kim, S. Kang, J. Lee, J. Jang, Y. Lee and D. Kwon (2007) Influence of surface-roughness on indentation size effect. Acta. Mater. 55:3555–3562.

[48] L. Hemmouche, D. Chicot, A. Amrouche, A. Iost, M.A. Belouchrani, X. Decoopman, G. Louis and E.S. Puchi-Cabrera (2013) An analysis of the elastic properties of a porous aluminium oxide film by means of indentation techniques. Mater. Sci. Eng. A 585: 155-164.

[49] J.L. Hay, G.M. Pharr (2000) Instrumented indentation testing. ASM Handbook - Mechanical Testing and Evaluation 8: 232 - 243.

[50] G.M. Pharr (1998) Measurement of mechanical properties by ultra-low load indentation. Mater. Sci. Eng. A 253: 151 - 159.

[51] A. Bolshakov, G.M. Pharr (1998) Influence of pile-up on the measurement of mechanical properties by load and depth sensing indentation techniques. J. Mater. Res. 13: 1049-1058.

[52] R. Ferré, S. Fouvry, B. Berthel, J.A. Ruiz-Sabariego (2013) Stress gradient effect on the crack nucleation process of a Ti–6Al–4V titanium alloy under fretting loading: Comparison between non-local fatigue approaches. Int. J. Fatigue 54: 56–67.